RICE UNIVERSITY

Examination of magmatic differentiation processes in the formation of intermediate and silicic composition magmas: constraints from regional and global geochemical systematics

by

Michael Joseph Farner

A THESIS SUBMITTED
IN PARTIAL FULFILLMENT OF THE
REQUIREMENTS FOR THE DEGREE

Doctor of Philosophy

APPROVED, THESIS COMMITTEE

Cin-Ty A. Lee, Chair
Professor of Earth Science, Department of Earth Science

Rajdeep Dasgupta
Professor of Earth Science, Department of Earth Science

Helge M. Gonnermann
Associate Professor, Department of Earth Science

Julia K. Morgan
Professor of Earth Science, Department of Earth Science

Scott P. Egan
Assistant Professor, Department of BioSciences

HOUSTON, TEXAS
APRIL, 2017

Abstract

Examination of magmatic differentiation processes in the formation of intermediate and silicic composition magmas: constraints from regional and global geochemical systematics

by

Michael Joseph Farner

Granitic rocks and mafic enclaves from the Bernasconi Hills pluton in the Peninsular Ranges Batholith, California, USA provide constraint on the extent and spatial lengthscale of mafic-felsic interaction in upper crustal granitic plutons. Further detailed mapping of mineralogical variations in the pluton and among enclaves highlights late-stage magmatic processes such as segregation of evolved residual melt and reactions between solidified enclaves and granitic melts. Collectively, the field, mineralogical and geochemical systematics of the Bernasconi Hills pluton show that mafic-felsic mixing between host granitic magma and partially solidified mafic enclaves was limited spatially, on the order of meters, and only proceeded to an early, incipient stage. Phosphorus-zirconium systematics indicate that the pluton developed through a combination of crystal fractionation and incipient mixing, in contrast to volcanic rocks, where magmatic evolution is primarily driven by crystal fractionation. Further examination of global geochemical systematics of subaerial arc lavas show a correlation between SiO_2 and crustal thickness as expressed by elevation. Arc lavas become more compositionally evolved with increasing elevation/crustal thickness, tend towards increasingly iron-depleted, or calc-alkaline, compositions and show evidence for garnet fractionation at depth in thick arcs. Coupled thermal and thermodynamic compositional modeling indicates that crustal thickness controls arc lava compositions by modifying the thermal lifespan and segregation times of melt in crustal magma chambers.

Acknowledgements

A thesis only lists one author, however, there are many people who helped this author complete it and to whom I am truly grateful. Firstly, I would like to thank my advisor, Cin-Ty Lee, for his patience, enthusiasm, and support of my research. Cin-Ty taught me many things during my time at Rice, but perhaps most importantly how to think about science, how to distill a problem down to its essence, and how to see the interconnectedness of seemingly disparate topics. I feel grateful to have been able to work with such a fantastic person and supportive mentor.

I would also like to thank my committee members Rajdeep Dasgupta, Helge Gonnermann, Julia Morgan, and Scott Egan for their interest and enthusiasm in my work as well as scientific input and advice. A great deal of thanks is due to several current and former students and post docs in the lab, including Wenrong Cao, Emily Chin, Xu Chu, Monica Erdman, Hehe Jiang, Peter Luffi, Lexi Malouta, Ming Tang and Julin Zhang for discussions and feedback. I would also like to thank Gelu Costin, Detao He and Xun Yu for their insight and discussions at various points. Special thanks are due to Mark Mikus for his assistance and comradery in the field during the early stages of this work and Graham Eldridge for his contributions in the lab.

I have had the good fortune to have made many friends during my time at Rice and would like to thank Clint Miller, Pranabendu Moitra, and Harsh Vora for their friendship and many enjoyable scientific discussions.

Finally, I would like to thank my fiancé Samantha Renee Barrow for her love, support, and tolerance for listening to my ramblings on, among other things, granite, mafic enclaves, the PRB, and K-feldspar megacrysts

Funding for the work in this dissertation was provided by the National Science Foundation, teaching assistantships from the Rice University Department of Earth Science, a research fellowship from the Chevron Corporation and a student research grant from the Geological Society of America.

Contents

List of Figures

Chapter 1

Introduction

Since the pioneering work of N.L. Bowen nearly a century ago, magmatic differentiation has been one of the primary focuses of igneous petrology. Volcanoes and batholiths give valuable constraints on the role of crustal processes in transforming a mantle melt into the compositions observed at the surface. Continuous crustal arc sections (e.g. Kohistan Arc section, Pakistan; Bonanza Arc section, Vancouver, Canada) provide in-situ examples of how melts evolve at different depths in the crust, but these are sparse. Samples from individual volcanoes and plutons are far easier to come by, but taken alone, only represent snapshots of the overall differentiation process. Thus, it is necessary to examine igneous rocks at a variety of scales, from local case studies to global compilations, to assess the first order controls on magmatic differentiation.

This dissertation is focused on examining magmatic differentiation processes using geochemical systematics from a detailed case study of the Bernasconi Hills pluton in the Peninsular Ranges Batholith, California and data from a global compilation of samples from all active volcanic arcs. The Bernasconi Hills pluton is a small granitic intrusion in the western Peninsular Ranges and provides an excellent example of intimate mingling between mafic enclaves and host granitic magmas. Here, I present data from a detailed field-based examination of mafic enclaves and associated granitic host rocks as a means of better constraining the lengthscales of mafic-felsic interaction in upper crustal intrusions. This work is complemented

by a global study of magmatic differentiation as recorded by volcanic rocks to provide further context for the role of intracrustal processes in magmatic differentiation.

The second chapter of this dissertation presents a study of reactions between mafic enclaves and their host granitoid melt. I show that solidified enclaves react with incompatible element-rich late-stage melts to form biotite-rich rinds along their outer margins. Additionally, I show that these rinds preferentially deform, compared to the parent enclave, to form highly attenuated schlieren that eventually become indistinguishable from, and effectively homogenized with, the host magma. This study helped to set the focus of my work at Bernasconi Hills on the enclaves themselves and motivated some of the work presented in Chapters 3 and 6. This chapter has been published in Earth and Planetary Science Letters (Farner, M.J., et al. "Mafic-felsic magma mixing limited by reactive processes: a case study of biotite-rich rinds on mafic enclaves". Earth and Planetary Science Letters 393 (2014): 49-59).

In Chapter 3, I expand from looking at enclave rinds to examining interaction between enclaves and host granitoid in a ~15 m wide enclave swarm. Here, I present geochemical systematics of the mafic enclaves and host pluton. The data show most of the enclaves and host rocks fall into two distinct compositional groups, but there is limited compositional overlap between a few enclave and host samples. These samples are from the enclave swarm and despite retaining distinct textural characteristics, they appear to represent incipient mafic-felsic mixing. Compositional transects across plagioclase phenocrysts from host rocks are unzoned and thus do not show any evidence of widespread mixing in the pluton. Comparison of conductive cooling timescales and diffusive re-equilibration timescales for the pluton and plagioclase crystals, respectively show that the unzoned profiles observed in the plagioclase cannot be due to re-equilibration and must represent a record of the cooling magma chamber, further supporting the

interpretation that mixing is limited. Comparison of thermodynamic calculations of melt evolution and phosphorous-zirconium saturation systematics suggests a combination crystal fractionation and limited mixing is responsible for producing granitoid compositions. Furthermore, while the enclaves and host granitoids have limited interaction at the present level of exposure, the enclaves may have interacted with other magmas on their way up. This chapter is under review as a manuscript for the Geological Society of America Bulletin.

Chapter 4 makes a detour to the volcanic realm, examining global geochemical systematics of subaerial lavas with respect to crustal thickness. In this chapter, I examine how mean arc lava composition changes as a function of crustal thickness using a 10 km x 10 km elevation model and an empirical relationship between elevation and crustal thickness in orogenic belts. The data show a clear increase in SiO_2 and incompatible element contents with increasing elevation/crustal thickness, with lavas averaging basaltic at low elevations and andesitic lavas dominating at high elevations. Paradoxically, the most primitive basalts and most SiO_2-rich rhyolites are both observed at low elevations, but are generally absent at high elevations. A two-stage model is developed for magma ascent and cooling where melt rises from the mantle along a dike cooling conductively until it ponds in a convecting crustal magma chamber. This is coupled with parameterizations of melt SiO_2 content and melt fraction as functions of temperature based upon calculations from the Rhyolite-MELTS thermodynamic program. Two things are evident from these calculations, first, melt rising through thick crust undergoes more cooling and is therefore more evolved by the time it reaches the surface. Second, once melt ponds in the crust, the erupted composition depends upon the difference between the cooling timescale of the melt and melt segregation timescale. To illustrate, melt in a deep magma chamber takes longer to cool because the geothermal gradient increases with depth. This extends

the thermal lifespan of the melt compared to a shallow magma chamber such that the cooling timescale is much longer than the melt segregation timescale. As a result, formation of silicic compositions is prevented in thick crust because the melt segregates before most of the magma has crystallized. In thin crust settings, cooling timescales are short and the melt cools faster. If the segregation time is longer than the thermal lifespan, the bulk composition of the magma chamber will remain basaltic since no segregation can take place. However, if segregation times and cooling times are similar, highly evolved residual melt can be extracted, giving rise to the rhyolites observed in thin island arcs. Finally, a distinct iron depletion trend is observed with increasing crustal thickness and is accompanied by increasing La/Yb and Gd/Yb ratios. This suggests that crustal thickening gives rise to the calc-alkaline (iron depletion) differentiation trend observed primarily in continental arcs. This chapter is currently in revision for Earth and Planetary Science Letters.

Returning to intrusive settings, the fifth chapter examines the role of late stage melt segregation in the formation of K-feldspar megacrysts. Here, I present textural systematics of K-feldspar-bearing and K-feldspar-absent rocks in the Bernasconi Hills pluton. Rocks with K-spar primarily occur in a ~15 m wide region near the center of the pluton and contain 1-2 mm subhedral to euhedral K-spar phenocrysts. These phenocrysts generally lack inclusions and have symplectic intergrowths of K-spar and quartz along crystal faces. Additionally, all samples with K-feldspar are silicic (> 70 wt. % SiO_2) and enriched in K_2O and Ba compared to K-spar-absent rocks. Finally, as observed in K_2O-SiO_2 space, K-spar-bearing and K-spar-absent samples define a linear trend with a distinctly different slope from intermediate samples, suggesting that granitoids with K-feldspar represent late segregated liquids while some K-poor, K-spar-absent rocks represent the cumulates to these liquids. Using potassium, I estimate that K-feldspar

crystallizes when only ~10-20 % of melt remains, relative to a parental composition, in agreement with experimental studies of K-feldspar crystallization. Comparison with megacrystic granites shows that rocks with K-spar megacrysts have the same K_2O content and proportion of K-feldspar, despite having giant (> 5 cm) crystals. Additionally, K-feldspar megacrysts also appear to have begun crystallizing late, with ~10-20 % melt remaining. Collectively, this motivates the notion that K-feldspar megacrysts, despite their large sizes, formed in a similar fashion to the K-spar in Bernasconi Hills. Thus, I suggest megacrysts form from evolved segregated liquids late in the cooling history of their host intrusion and grew quickly.

Finally, in Chapter 6, I present 5 m scale enclave distribution maps of geochemical sampling transects through the Bernasconi Hills pluton with corresponding geochemical cross sections. These transects provide an additional spatial dimension to the geochemical systematics described in Chapter 3 and places the textural systematic described in Chapter 5 into greater context. Comparison of geologic maps and geochemical sections shows that the composition of host granitoids is reflects variations mineralogy. For example, in the portion of the pluton where K-feldspar-bearing granitoids are present, a clear rise in K_2O and Ba occurs and remains elevated. In some instances, granitoid composition also appears to reflect the relative abundance of enclaves. Where the transect crosses a ~15 m wide enclave swarm, granitoid compositions overlap with the enclaves, highlighting the spatial extent of the incipient mixing described in Chapter 3. Enclave compositions are more variable. Enclaves generally contain higher heavy rare earth element concentrations, which appears to be due to their higher hornblende contents.

Chapter 2

Mafic-felsic magma mixing limited by reactive processes: A case study of biotite-rich rinds on mafic enclaves[1]

[1]This chapter has been reprinted and reformatted from Earth and Planetary Science Letters (full citation below).

[1]Farner, M.J., Lee, C.-T.A., Putirka, K.D. Mafic-felsic magma mixing limited by reactive processes: a case study of biotite-rich rinds on mafic enclaves. Earth and Planetary Science Letters 393 (2014): 49-59.

Mafic enclaves in felsic plutons are often used to argue that intermediate magmas form by mafic-felsic magma mixing, but the extent and nature of mixing remains unclear. Here, we examine biotite-rich rinds on mafic enclaves from the Cretaceous Bernasconi Hills Pluton in the Peninsular Ranges Batholith of southern California to gain insight into magma mixing processes. Rinds differ from the enclave interior and the host monzogranite in being more fine-grained and more mafic and potassic. Rinds are also 2-5 times more enriched in rare earth elements than the host monzogranite and up to 3 times more enriched than enclave interiors. These observations indicate that the rinds were not generated by isochemical quenching, binary mixing between enclave and host monzogranite, or in-situ magmatic differentiation. Instead, rinds appear to have formed by chemical reaction between the solidified enclave and a hydrous K-rich residual melt or fluid formed after progressive crystallization and cooling of the host magma body, transforming amphibole in the enclave into biotite-rich rinds. Field observations show snapshots of biotite-rich rinds being eroded off and new rinds simultaneously forming on freshly eroded surfaces of enclaves, consistent with rinds being formed by chemical reaction instead of as quenching products. Deformation of enclaves is accommodated primarily by ductile attenuation of the thin rind while the enclave as a whole tends to rotate as a rigid body with minimal internal deformation other than localized brittle failure. A comparison of the aspect ratios and cross-

sectional areas of mafic bodies in the pluton shows that those with high aspect ratios (indicating greater accumulated strain) are systematically more biotite-rich and have smaller cross-sectional areas than those with lower aspect ratios, which are amphibole-rich. These relationships not only confirm that biotite-rich lithologies are more deformable but also indicate that the high aspect ratio biotite-rich bodies (also known as schlieren) derive from small parent bodies, consistent with a derivation from eroding enclave rinds rather than from the enclave itself. Finally, geochemical and thermodynamic modeling indicates that the biotite-rich rinds formed when the host felsic magma had cooled to a low melt fraction state (F=0.15-0.3; 700-760°C), suggesting that such reactions occur late in the lifespan of a magma body. Thus, mafic-felsic mixing may not be an efficient process for making intermediate magmas unless the magma body can reside at this low temperature range long enough to permit rind formation and subsequent deformation.

2.1 Introduction

Mafic enclaves are ubiquitous in felsic plutons, and their presence has been interpreted as evidence of mixing between mafic and felsic magmas (Barbarin, 2005; Frost and Mahood, 1987; Furman and Spera, 1985); Pabst (1928); (Ratajeski et al., 2001; Reid et al., 1983; Vernon, 1984, 1990; Walker and Skelhorn, 1966; Wiebe et al., 1997). The abundance of enclave-bearing plutons has motivated the hypothesis that mixing may be an important mechanism by which intermediate magmas, like andesites, form (Eichelberger, 1975; Frost and Mahood, 1987; Ratajeski et al., 2001; Reid et al., 1983). Although many studies have demonstrated geochemical mixing trends exist between enclave and granitoid end-members, the exact processes by which mixing occurs remain unclear (Eichelberger et al., 2006; Frost and Mahood, 1987; Ratajeski et al., 2001; Reubi and Blundy, 2009; Sisson et al., 1996; Zorpi et al., 1989). A common feature of

enclaves is that they are finer-grained than their host pluton and often have dark, fine-grained margins. This has led to the interpretation that enclaves are chilled upon contact with felsic magma and that these fine-grained margins represent quench rinds (Barbarin, 2005; Blake et al., 1965; Chapman, 1962; Furman and Spera, 1985; Vernon, 1990; Wager and Bailey, 1953; Walker and Skelhorn, 1966; Wiebe et al., 1997). Such a scenario is expected given that mafic magmas have higher liquidus and solidus temperatures than silicic magmas and therefore should freeze if intruded into a silicic magma host. However, freezing of mafic magmas would result in a high viscosity contrast between the solidified enclaves and the partially molten host magma, thereby inhibiting deformation of enclaves and mechanical mixing (Frost and Mahood, 1987; Paterson, 2004). Mixing might only be efficient in basalt-dominated systems as the basaltic host would provide sufficient heat to completely melt felsic material, but the reverse, that is, mixing of mafic enclaves incorporated into felsic-dominated systems, is more difficult. How do we reconcile the rheological difficulties of mafic-felsic mixing with the apparent evidence for mixing based on the presence of mafic enclaves and associated schlieren?

Here we examine enclaves from the Cretaceous Bernasconi Hills Pluton in the northern Penninsular Ranges of southern California. At this locality, rinds on mafic enclaves are chemically distinct from both the host rock and enclave core and therefore cannot represent isochemical quench rinds. We demonstrate that these rinds are K and biotite-rich and exhibit highly enriched REE patterns compared to enclave interiors and host rock. This implies that the rinds may instead represent reaction products between the enclave and interstitial liquids within the host magma body. We propose that these biotite-rich rinds form by reaction between hydrous residual liquids or fluids and the solidifying mafic enclave during the late stages of pluton crystallization. We further show that these rinds are rheologically weak and hence become

preferentially deformed relative to their parent enclave, resulting in their delamination or erosion from the enclave and the formation of biotite-rich schlieren. We propose that enclave deformation and the formation of schlieren is thus limited by the generation of biotite-rich reaction rinds. Therefore, magma mixing, in at least some felsic systems, may be limited by chemical reaction between enclaves and interstitial melt.

2.2 Geologic Background

The Peninsular Ranges Batholith (PRB) intruded during the mid to late Cretaceous and is the southernmost intrusion in the chain of North American Mesozoic batholiths spanning from Alaska to Baja California. The PRB has been divided into western and eastern zones based upon regional variations in lithology, geochemistry and age of individual plutons as well as metamorphic grade of surrounding wallrock (Gastil, 1975; Gromet and Silver, 1987; Kistler et al., 2003; Lee et al., 2007; Todd, 1985; Todd et al., 1988; Wetmore et al., 2003). This boundary between western and eastern zones is inferred to represent a tectonic suture between accreted island arc terranes and the Paleozoic North American continental margin, respectively (Gastil, 1975; Kistler et al., 2003; Lee et al., 2007; Todd et al., 1988; Wetmore et al., 2003). In the northern PRB the boundary runs roughly north-south until the Agua Blanca Fault in Baja California, where it trends southeast until the terminus of the range (Gastil et al., 1988; Lee et al., 2007; Wetmore et al., 2003).

This study focuses on the Bernasconi Hills Pluton, which lies west of the suture in the northern PRB, Riverside County, California. The southern margin of the pluton is truncated by the adjacent ~90 Ma Lakeview Mountains Pluton (Mason and Cohen, 1990; Morton, 1969, 2003) indicating that it is older than 90 Ma, but the exact age is unknown. It is composed mainly of

monzogranite, granodiorite and tonalite, however small bodies of diorite are also observed within the pluton. Our study area lies along a ~200 m segment (33.839° N, 117.168° W) exposed by recent quarrying in the southern portion of the pluton. Quarrying has provided fresh outcrop exposure and a clear view of mafic enclave-host rock relations within the interior of the pluton.

2.3 Analytical Methods

Mafic enclaves and the adjacent host granitoid were collected from the quarried section of the Bernasconi Hills Pluton. Enclaves were selected on the basis of being relatively unweathered and having a sufficiently thick rind for geochemical analysis. Each enclave was separated into host rock, rind and enclave interior subsamples with a saw. Whole rock geochemistry samples were crushed to a fine powder in a tungsten carbide mill and fused with a lithium tetraborate-lithium metaborate mix. Major oxide compositions were determined by X-ray fluorescence spectrometry (XRF) at California State University, Fresno (see (Busby et al., 2008). Trace element concentrations were determined at Rice University by laser ablation-ICP-MS (LA-ICP-MS) with a ThermoFinnigan Element 2 equipped with a New Wave 213 nm laser ablation system for the same fused glass disks used in XRF analyses. External standards used for LA-ICP-MS analysis were United States Geological Survey basaltic (BHVO2g and BCR2g) and National Institute of Standards synthetic silica-rich glasses (NIST612). Laser ablation was conducted with a fluence of 20 J/cm^2, 10 Hz frequency, and 55 μm spot size. Prior to measurement, the instrument was tuned by controlling the sample gas (Ar) to achieve a sensitivity of 250,000 cps on 15 ppm La in BHVO2g in low mass resolution (m/Δm ~300). Raw data were converted to concentrations using an in-house data reduction program (http//www.ruf.rice.edu/~ctlee/Laser-RAWDATA-TEMPLATE.xls) that removed background

signal intensities and elemental fractionation with external standards. Signal intensities were normalized to an internal standard (^{25}Mg), and time-resolved intervals were integrated.

2.4 Field Observations

2.4.1 Granitoid Rocks

The Bernasconi Hills Pluton is mainly composed of biotite-hornblende-monzogranite and granodiorite with lesser amounts of tonalite. At outcrop scale (~5 m) the pluton has a uniform appearance except where enclaves, schlieren and biotite-amphibole selvages are present. Diorite is also present as a large body near the middle of the quarried section of the pluton. The diorite weathers dark gray and superficially resembles mafic enclaves, but is distinguished by its coarse-grained texture and more heavily weathered appearance.

2.4.2 Enclaves

Mafic enclaves occur as gray to blackish blobs throughout the Bernasconi Hills Pluton and range in size from a few centimeters to a meter in longest dimension. Enclaves show varying degrees of attenuation as shown in Figure 2.1. Enclave size and shape vary on the scale of a few centimeters in some parts of the pluton and these variations are most pronounced where there is a large enclave density such as in enclave swarms. The range of enclave shapes indicate that multiple stages in the strain history of a typical enclave are preserved within the pluton, giving a continuous view of how physical interaction between enclaves and the host magma progresses with respect to the enclave.

Almost all enclaves are mantled by thin (0.2-2 cm thick) rinds, which differ from the amphibole-rich enclave interiors by being darker in coloration, finer-grained, and biotite-rich. In many cases, the biotite-rich rinds appear to delaminate, erode or shear off from the parent enclave (Figure 2.1B), suggesting that strain accumulates preferentially in the rind or at the rind-enclave interior interface while the enclave interior remains largely undeformed except for occasional evidence of brittle fracture. Rinds appear to form on enclave surfaces at all stages of enclave development, with new biotite-rich rinds re-forming after earlier ones are mechanically eroded away (Figure 2.1B).

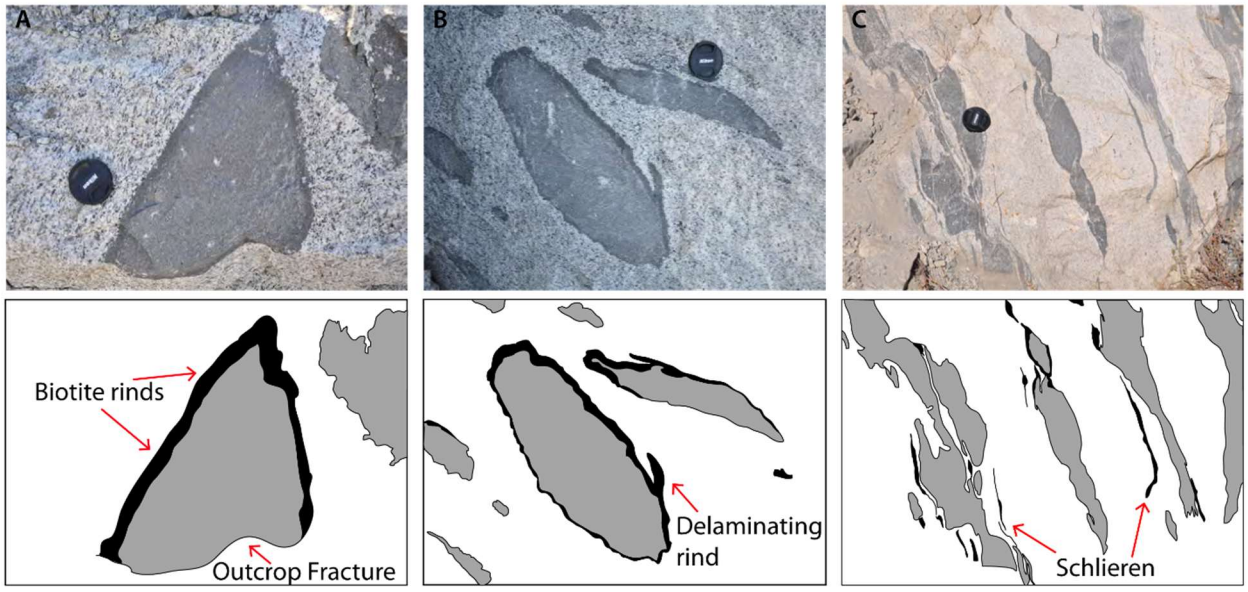

Figure 2.1. Relationship of biotite-rich rinds to mafic enclaves and host monzogranite. (A) An undeformed enclave with a well-developed rind. (B) Slightly elongated enclaves with delaminating rinds. As rinds delaminate, rinds continue to form on the newly exposed enclave surface. (C) Elongated enclaves with eroded rinds and associated schlieren. The rinds and schlieren are biotite-rich and appear to be rheologically weak, resulting in higher rates of strain accumulation than the enclave as a whole.

2.4.3 Schlieren

Schlieren are dark, fine-grained, biotite-rich segregations within the host granitoid. They vary in length (several cm to >3 meters) and thickness (<1 cm to 10 cm) and are characterized by

a foliation fabric defined by preferentially aligned biotite crystals. Schlieren are most common near the margins of enclave swarms and appear texturally identical to the biotite-rich rinds associated with enclaves. In many cases they are observed in close proximity to rinds and in some cases appear to derive directly from them (Figure 2.1B-C).

2.4.4 Aspect ratio of mafic enclaves and selvages

The quarried face of the pluton is primarily perpendicular to the large scale foliation defined by the attenuated mafic enclaves. We measured the long (*a*) and short (*b*) axes of enclaves and associated biotite and amphibole-rich selvages in order to compare their aspect ratios (*a/b*) and cross-sectional areas ($A=\pi ab$) perpendicular to the foliation plane. Selvages look superficially similar to rinds and are distinguished from enclaves by being darker and finer-grained. They generally have higher aspect ratios (*a/b*) and lower cross-sectional areas compared to enclaves (Figure 2.2), indicating that the selvages accumulate more strain than the enclaves and are therefore more deformable. Low aspect ratios determined for enclaves indicate that enclaves do not attenuate appreciably and instead rotate.

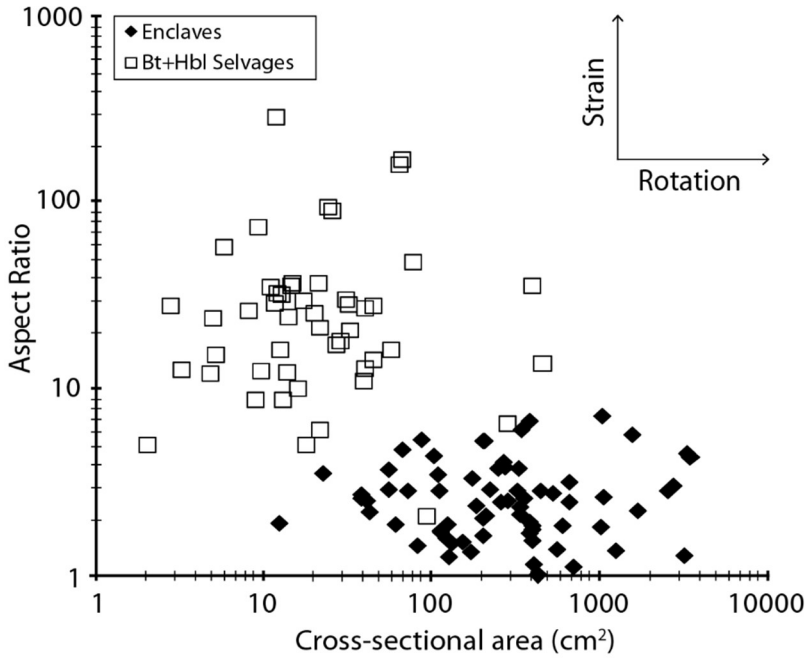

Figure 2.2. Plot of aspect ratio versus cross-sectional area for biotite-rich selvages and enclaves. Selvages have higher aspect ratios and smaller cross-sectional areas compared to enclaves, indicating that they have accumulated more strain. While enclaves do deform, their generally low aspect ratios suggest that they primarily rotate, consistent with the view that enclaves have a high viscosity contrast with the host magma (Paterson et al., 2004). The systematically higher aspect ratios of the selvages, combined with their small cross-sectional areas, suggests that they preferentially derive from small and more deformable parent bodies, such as the biotite-rich rinds on the enclaves.

2.5 Petrography

2.5.1 Granitoid Rocks

Plagioclase (~30%) and quartz (~50%) occur as subhedral and anhedral crystals and comprise the bulk of the host pluton. Alkalic feldspar (~15%) is also present as subhedral grains, some of which are zoned. Biotite (~1%) is scarce, but when present, it occurs in clots as coarse subhedral and anhedral crystals (Fig. 3). Hornblende (~5%) is generally more abundant in the host rock than biotite and occurs mostly in clots of stubby dark green crystals. Apatite, ilmenite, magnetite, sphene and zircon are observed as accessory phases.

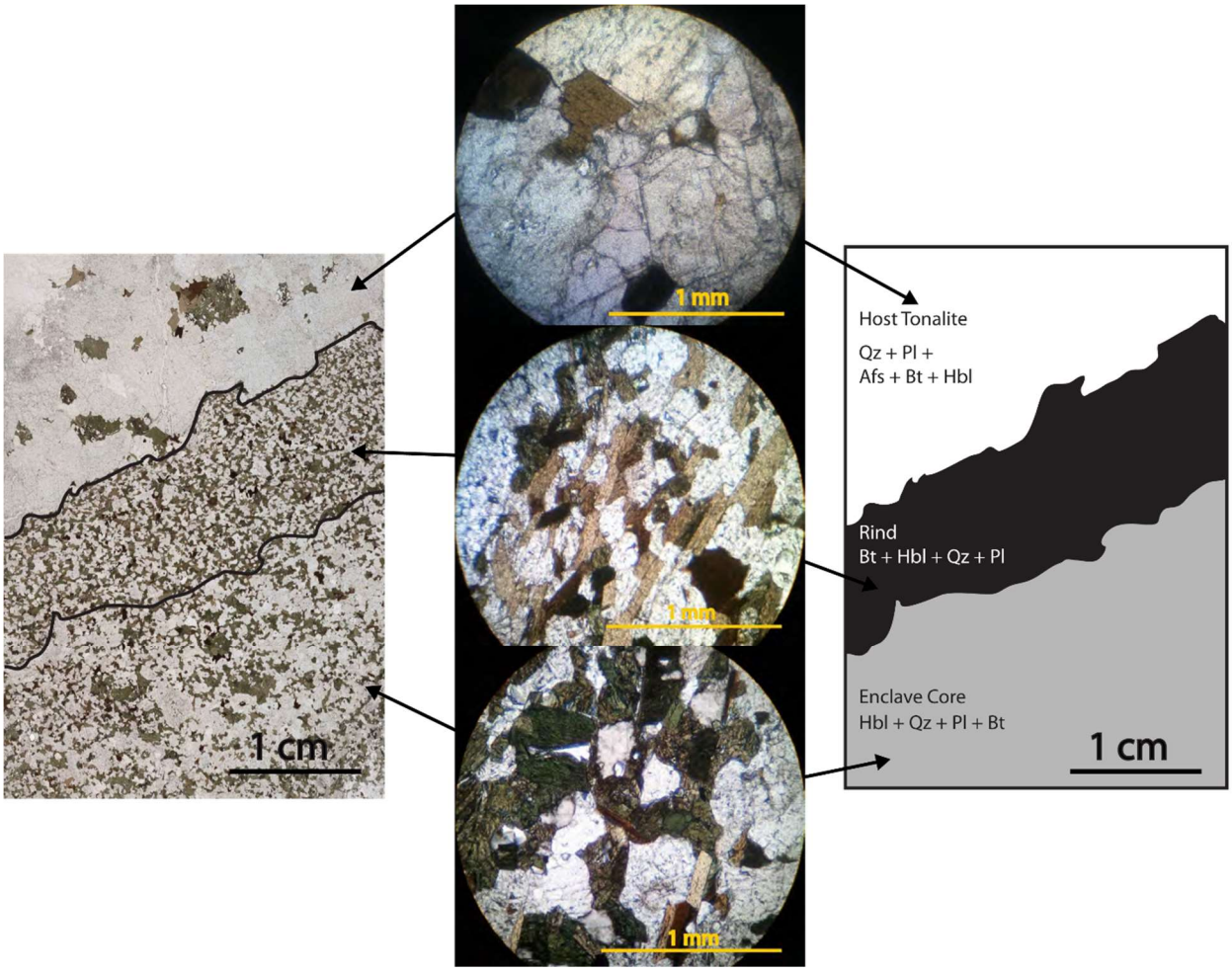

Figure 2.3. Petrographic transect of an enclave with granitic host, biotite-rich rind and enclave interior. Mineral abbreviations used here and elsewhere in the text are from Whitney and Evans (2010).

2.5.2 Enclaves

Mafic enclaves are mineralogically zoned between an outer fine-grained, biotite-rich rind and an inner biotite-poor region (Figure 2.3). Enclave interiors are composed of quartz (~35%), plagioclase (~20%) and hornblende (~32%). Quartz is generally equigranular, suggesting recrystallization, and is most abundant near the center of the enclave. Plagioclase occurs as lathes

and subhedral grains and is present in roughly equal proportions throughout the enclave interior. Biotite (~13%) forms subhedral to anhedral brown to yellow-brown crystals. It is not abundant in enclave interiors, but when present it is typically associated with hornblende. Hornblende commonly forms clots of subhedral to anhedral dark green crystals, although it also occurs as an interstitial phase between quartz and plagioclase in the central parts of the enclave interior. Hornblende is most abundant in the outer region of the enclave interior, adjacent to the biotite-rich rind. Apatite and magnetite are present as accessory minerals within enclaves.

Rinds are finer-grained than the enclave interior and have a higher density of mafic minerals. They are biotite-rich (30%), and contain hornblende (~25%), plagioclase (~10%) and quartz (~35%). Biotite occurs as euhedral to subhedral yellow-brown crystals and is most abundant along the outer portions of rinds and steadily decreases in abundance towards the rind-enclave boundary (Figure 2.3). Additionally, biotite crystals within rinds are aligned parallel to the enclave-host magma interface, which contrasts with the lack of orientation within the enclave interior. Hornblende generally forms stubby, anhedral crystals and is roughly aligned with biotite. Quartz and plagioclase are both equigranular. Plagioclase is aligned parallel to biotite. Rinds do not contain any accessory minerals other than apatite, which is typically observed as fine-grained needles within plagioclase and quartz.

2.6 Geochemistry

2.6.1 Major Elements

The host monzogranite is characterized by ~72 wt% SiO_2, ~0.8 wt% MgO, ~3 wt% CaO, ~3 wt% Fe_2O_3, ~13-14 wt% Al_2O_3, and ~5 wt% alkalis (Appendix A).

Enclave interiors are intermediate (basaltic trachy-andesite to trachy-andesite; 56-59 wt% SiO_2) in composition. Interestingly, enclave interiors are more alkalic (Na_2O+K_2O ~6 wt%) than the surrounding host rock despite having lower SiO_2 and higher MgO (~3 wt%) content (Figure 2.4A). Na_2O is slightly greater in enclave interiors than in either the enclave rind or host rock due to the abundance of hornblende within the enclaves. Enclave rinds are less felsic (SiO_2 ~52-55 wt%), more potassic (~1.6-2.6 wt%), and have higher MgO and Fe_2O_3 content (~3.4 wt% and ~12-13 wt%, respectively) than enclave interiors and host tonalite (Figure 2.4A-B). Rinds are significantly more potassic than the host monzogranite despite being more mafic. One rind is more felsic (SiO_2 ~57.6 wt%) and has less MgO (3 wt%), and Fe_2O_3 (10 wt%) than other measured rinds, but is still more potassic (K_2O ~1.9 wt%) than measured enclave interiors and host monzogranite.

2.6.2 Trace Elements

Trace element concentrations (Appendix A) for host monzogranite, enclave interior, and enclave rinds have been normalized to the bulk continental crust (BCC; (Rudnick and Fountain, 1995) (Figure 2.4C) and show systematic differences between each lithology. Normalized heavy rare earth element (HREE) concentrations for all samples are subparallel to BCC and are enriched by 2 to 12 times with respect to BCC.

The host monzogranite is less enriched in the REEs (Figure 2.4C) compared to enclave interior and rind samples. The LREE contents of enclave interiors are similar to that of the rinds but the HREEs are lower in the enclaves than in the rinds Rinds show varying degrees of REE enrichment compared to enclave cores and host rocks (Figure 2.4C). This enrichment is most pronounced for the HREEs with normalized rind concentrations roughly 2-5 times greater than

average host rock and up to 3 times that of enclave cores. REE enrichment is greatest in rinds with high modal proportions of biotite. Rinds show strong relative depletions in Eu, Sr and Zr.

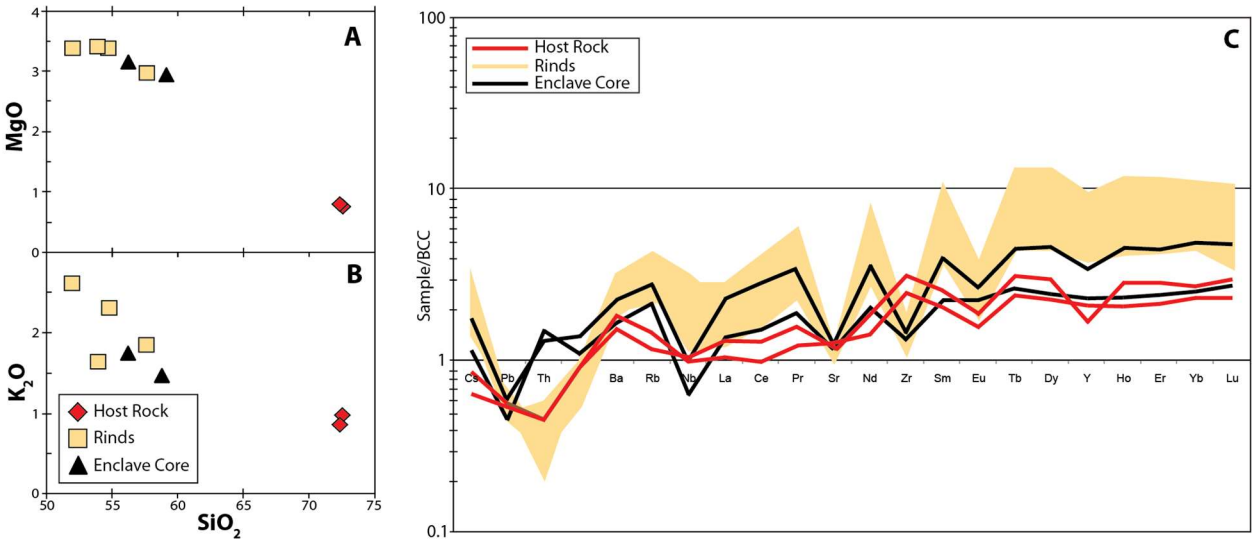

Figure 2.4. Whole-rock major (A and B) and trace element geochemistry (C) of host monzogranite, mafic enclave interiors, and rinds. Rinds are both more mafic and potassic than their parent enclave and the host rock. They are also substantially enriched in heavy rare earth elements, but show extreme depletions in Eu, Zr and Sr. Oxides are in weight %. Trace elements have been normalized to model bulk continental crust (Rudnick and Fountain, 1995).

2.7. Discussion

2.7.1 Assessing the origin of biotite-rich rinds

Several processes have been proposed to explain the nature of interaction between enclaves and felsic magmas. These include 1) isochemical quenching of enclave magmas, 2) mechanical mixing between host magma and enclaves, 3) in-situ magmatic differentiation of the enclave, 4) gas-filter pressing and 5) reaction with the host magma and are addressed here in the context of our field, petrographic, and geochemical observations.

The isochemical quenching scenario (Barbarin, 2005; Blake et al., 1965; Didier, 1973; Furman and Spera, 1985; Ratajeski et al., 2001; Wager and Bailey, 1953; Wiebe et al., 1997) is motivated by the fact that liquidus and solidus temperatures of basaltic magmas are much higher than those of granitic magmas and such a sharp temperature gradient would result in rapid cooling of mafic enclaves. However, our geochemical data demonstrate that the rinds are compositionally distinct from the enclave and the host lava. The quenching hypothesis also predicts that rinds would form only during the initial injection of hot mafic magmas into the cold felsic host, but our field observations indicate that biotite-rich rinds form continuously, with new rinds forming even after earlier rinds are eroded off (Figure 2.1B).

The mixing scenario predicts that rind compositions should fall along linear mixing arrays between the felsic host and mafic enclave end-members. Rinds, however, are more mafic and potassic than both the enclaves and the host monzogranite and have elevated REE concentrations (Figure 2.4). Because rind compositions are not collinear with the felsic and mafic end-members, mechanical mixing between mafic enclave and felsic host alone cannot explain the rind compositions.

Generation of biotite-rich rinds via in situ crystallization of the mafic enclave also may not be supported by our study. Eberz and Nicholls (1990) proposed that geochemical zonation observed in enclaves in the Swifts Creek Pluton of southeastern Australia is the product of early crystallization that occurs when liquid mafic enclaves come in contact with felsic host magma thereby cooling and crystallizing inwards from the inner margin of the enclave. They suggest that enrichment in K and incompatible trace elements in rinds is caused by diffusion from the host magma into the enclave interior. However, if biotite-rich rinds form exclusively when enclave magmas first come in contact with felsic host magmas, rinds should not form afterwards

because the enclave would have already solidified due to rapid thermal equilibration on the small lengthscales under consideration. Instead, we observe that rinds form continuously as can be seen by the presence of rinds during different stages in the strain history of an enclave (Figure 2.1), precluding an origin by in-situ differentiation of the enclave itself.

The fourth scenario, gas-filter pressing, was proposed as a means of generating compositional zonation within mafic inclusions in volcanic rocks (Anderson et al., 1984; Bacon, 1986; Sisson and Bacon, 1999). In this process, residual melt is driven out of a crystallizing inclusion by excess pressure imposed by exsolved vapor, resulting in rhyolitic glass within a rind near the margins of the inclusion. Bacon (1986) suggested gas-filter pressing may occur in plutonic settings as a possible way of generating felsic haloes and veins adjacent to enclaves. Because residual liquids would be more evolved than the initial enclave magma, it is plausible that they would provide the enrichments in K and REEs observed in rinds. This is consistent with our geochemical observations and may provide an explanation for the origin of biotite-rich rinds on enclaves. However, like quenching, gas-filter pressing predicts that rinds should form at only one instant, that is, during expulsion of residual liquids from the enclave as it is crystallizing. This is inconsistent with the continual generation of rinds observed in this study (Figure 2.1B).

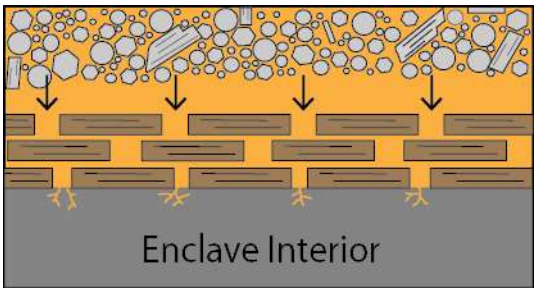

Figure 2.5. Cartoon illustrating a possible scenario of rind formation by reaction between interstitial residual liquids in the host monzogranite and the mafic enclave.

All of the above scenarios may operate at some level in magmatic systems, but none these scenarios alone adequately explains the origin of biotite-rich rinds. Instead, our field and geochemical observations are most easily explained if the rinds are products of continuous reaction between solid mafic enclaves and hydrous residual liquids or fluids in the host magma (Figure 2.5). We suggest that rinds are preferentially deformed and eroded from the parent enclave into the host magma, ultimately developing into schlieren, which become mixed into the magma (Figure 2.6). This is supported by our measurements of enclave and biotite-rich selvage aspect ratios (Figure 2.2), which indicate that thin, biotite-rich selvages are more deformable than enclaves and can accommodate large amounts of attenuation. We expand on the reactive mixing scenario in the next section.

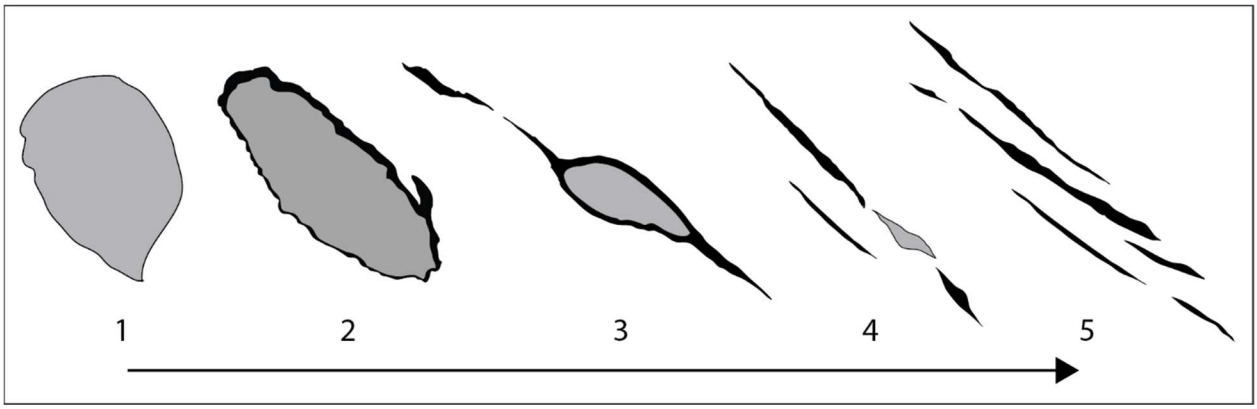

Figure 2.6. Cartoon illustrating hypothesized progression of reaction and deformation, beginning with reaction-driven rind formation followed by the formation of schleiren with progressive strain. (1) A mafic enclave is entrained in a felsic host melt. (2) Biotite-rich rinds begin to form on the enclave as enclave-interstitial residual liquid reactions progress. (3) Rinds erode from the enclave. Both enclave and eroded rind begin to elongate, but elongation is more efficient in the rheologically weak biotite-rich rind. (4) Freshly exposed surfaces on the enclave continue to react with interstitial melt to form new biotite-rich rinds. (5) Enclave has completely reacted and eroded rinds develop into schlieren.

2.7.2 Constraints on the mechanisms and timing of reactive rind formation

We now explore the mechanisms by which biotite-rich rinds form by chemical reaction between the solidified enclave and felsic magma. Petrographic relationships indicate that rinds

form by reaction between amphibole-bearing enclaves and hydrous K-rich felsic melts or fluids, suggesting the following simplified reaction:

$Ca_2Mg_5Si_8O_{22}(OH)_2 + 0.5K_2O(m) + 0.5Al_2O_3(m) = KMg_3AlSi_3O_{10}(OH)_2 + 2CaO(m) + 2MgO(m) + 5SiO_2(m)$ (2.1)

where oxides represent components within the melt or fluid. For simplicity, we assume end-member chemical formulas for amphibole and biotite, so Eq. 2.1 is meant solely for conceptual purposes. This equation indicates that increases in K_2O and Al_2O_3 activity or decreases in CaO, MgO, or SiO_2 activity in the magma drive the conversion of amphibole to biotite. At equilibrium, Eq. 2.1 requires the following relationship at a given temperature and pressure to yield the schematic activity diagram in Figure 7A:

$$\frac{-\Delta G_r^\circ}{RT} = 2\ln a_{CaO(m)} + 2\ln a_{MgO(m)} + 5\ln a_{SiO_2(m)} - 0.5\ln a_{K_2O(m)} - 0.5\ln a_{Al_2O_3(m)} \quad (2.2a)$$

The quantity on the left hand side is a constant, representing the P-T specific Gibbs free energy of pure substances at a standard state for reaction 2.1 divided by the gas constant and temperature.

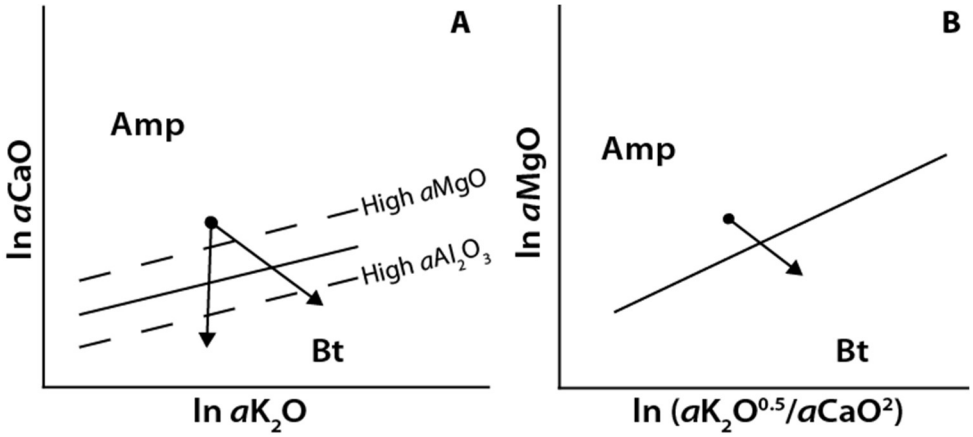

Figure 2.7. Schematic activity diagrams of amphibole + residual liquid = biotite + residual liquid. (A) CaO activity versus K_2O activity. (B) MgO activity versus K_2O/CaO activity. In A the bold black line defines the coexistence of biotite and amphibole and is given by equation 1. Dashed contour lines indicate changes in the respective mineral stability field with increases in either Al_2O_3 or MgO activities. The bold black line in B is given by rearranging equation 2b to yield ln aMgO = 0.5ln ($aK_2O^{0.5}/aCaO^2$) + C.

The right hand side expresses the natural logarithm of the activities of each component in the melt or fluid. Equation 2.2a can be simplified if we assume that the system contains quartz and plagioclase so that the SiO_2 activity is buffered and the Al_2O_3 activity is roughly buffered, yielding:

$$C = 2\ln a_{CaO(m)} + 2\ln a_{MgO(m)} - 0.5\ln a_{K_2O_{(m)}} \quad (2.2b)$$

where C is a constant that includes the Gibbs free energy of reaction and the activities of SiO_2 and Al_2O_3. Equation 2.2b is expressed in the schematic activity diagram in Figure 2.7B. It can be seen that increases in the K_2O activity in the melt or fluid must be the primary driver of converting amphibole to biotite. This is at odds with the fact that the K_2O concentration in the host magma is actually lower than that in the enclave interior as shown previously (Figure 2.4B). This suggests that the bulk host magma may not have been the reactant. Instead, it is the K_2O activity in the residual liquid/fluid that is of interest. As we will show below, the K_2O content or

K_2O/CaO ratio of interstitial liquids/fluids increases substantially during crystallization, thus we hypothesize that it is these interstitial liquids that are involved in the reaction rather than the bulk magma (crystals + liquid) itself.

We can evaluate this hypothesis by modeling the major element evolution of the residual liquid during crystallization of the host magma using the thermodynamic MELTS application (Asimow and Ghiorso, 1998; Ghiorso and Sack, 1995). This was done for variable bulk H_2O contents (0-4 wt%) over a range of pressures (2-3 kbar) applicable to emplacement of the Bernasconi Hills Pluton as inferred from the crystallization pressure map by Ague and Brimhall (1988) for plutons in southern California. We assumed closed system equilibrium conditions because crystal-liquid segregation of felsic magmas is relatively inefficient. All of our MELTS calculations reproduce the main constituent mineral phases observed in natural samples (Qtz, Plag, Amp, Kfs) except biotite, which was not stabilized. This may be due to the lack of comprehensive thermodynamic models for biotite in MELTS. In any case, biotite mode is low in the felsic host and, based on texture, appears late in the crystallization sequence. Because our model is focused on the composition of residual liquids in the felsic host, the effect of biotite on liquid compositions is small for most of the crystallization history.

Our modeling results indicate that K_2O/CaO begins to rise significantly in the residual liquid at melt fractions (F) of 0.55 to 0.6 (Figure 2.8A). This melt range suggests that biotite-rich rinds form when residual liquid fractions decrease to values below 0.5. The increase in K_2O/CaO in our modeled residual liquid is due to sequestration of Ca into feldspar rather than to a dramatic rise in the K_2O content of the magma. As shown in Figure 2.8A the increase in K_2O/CaO becomes more pronounced with increasing H_2O content in the melt.

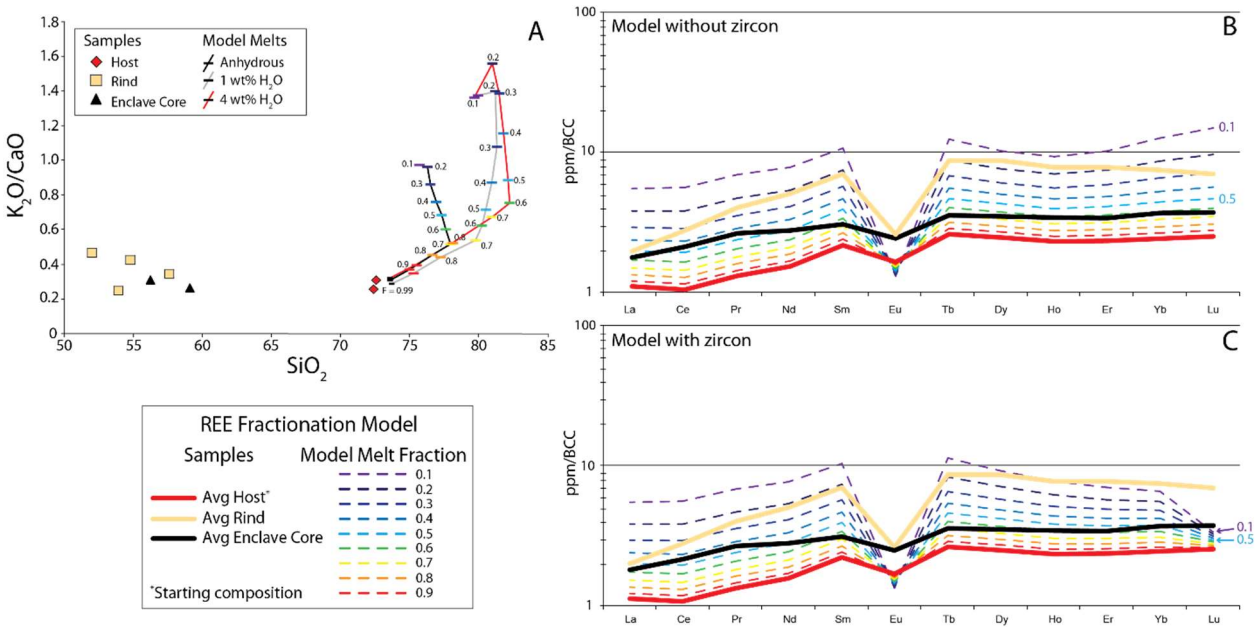

Figure 2.8. Modeling residual liquids with REEs and major oxides. Melt fraction is indicated by color as shown in A. (A) Evolution of residual liquids as constrained by K_2O/CaO ratios using the MELTS thermodynamic program (Ghiorso and Sack, 1995; Asimow and Ghiroso, 1998) for magmas with 0, 1, and 4 wt% initial H_2O. Calculated magma temperatures vary based upon initial H_2O content; 1113°C to 960°C (anhydrous), 1045-706°C (1 wt% H_2O), 865-706°C (4 wt% H_2O). Residual liquids and rinds have higher K_2O/CaO than the bulk melt and indicate that residual liquids, rather than the bulk host monzogranite, react with enclaves. (B-C) Modeling conditions of rind formation with REE patterns. The starting composition (F = 1) is average host monzogranite and the relative proportion of crystallizing phases is taken from petrographic mode estimates of the host monzogranite. Crystallizing phases are assumed to be in equilibrium with the residual melt. The average REE composition of rinds is used in conjunction with modeled REE patterns to estimate the melt fraction range of rind formation.

We can use trace element systematics as additional constraints. Qualitatively, the REE signatures of the rinds require reaction with a highly evolved residual liquid: REE abundances overall are enriched by at least a factor of 2 compared to the host magma and Eu is highly depleted. The only process that could generate this signature is segregation of a plagioclase-bearing assemblage, such that the Eu behaves compatibly and is sequestered into plagioclase while the remaining REEs behave incompatibly and remain with the residual liquid, resulting in a large Eu depletion relative to other REEs. The extent to which REEs can be fractionated and

enriched by crystallization can be quantified by modeling the REE evolution of residual liquids formed by equilibrium crystallization of the host magma (given the small lengthscales considered here we assume equilibrium crystallization). Our starting composition was assumed to be the average measured REE content of the host magma. Partition coefficients for plagioclase, biotite, hornblende, potassic feldspar and zircon are from Arth (1976), Nash and Crecraft (1985), and Bea et al. (1994). REEs are assumed to be perfectly incompatible (D_i=0) in quartz. We constrain the fraction of each crystallizing phase based upon petrographic mode within the host monzogranite (quartz ~51%, plagioclase ~30.5%, alkalic feldspar ~13%, hornblende ~4.5%, biotite ~1%). We assume, for simplicity, that the proportion of crystallizing phases does not change (in any case, the effect of biotite is negligible). Accessory phases, such as zircon, may also influence partitioning of REEs in granitic melts due to high partition coefficients (Bea et al., 1994), so crystallization models were run with 0.07% zircon (mode calculated from the bulk Zr content in the host magma) and without zircon for completeness.

Models with and without zircon both reproduce the overall relative REE abundance patterns in rinds for light rare earth elements and show a large negative Eu anomaly, thus supporting the involvement of a residual liquid rather than the bulk host magma in rind-forming reactions (Figure 2.8B-C). In detail, however, when zircon is included, HREEs are strongly depleted in the melt, particularly Er, Yb and Lu, which fall below that seen in the rinds (Figure 2.8C). This seems to suggest that zircon may not be an important accessory mineral during crystallization even though the negative Zr anomalies observed in the rinds (Figure 2.4C) suggest the involvement of zircon. One way to reconcile this apparent inconsistency is if the negative Zr anomaly is due to the fluid-immobile nature of Zr and its retention in other minerals like amphibole. In any case, because we are primarily interested in the overall REE patterns and the

associated negative Eu anomaly, it does not matter whether we use the zircon-free or present models. We thus apply the zircon-free model to further evaluate conditions of rind formation. The relative REE abundance patterns in the rinds can be reproduced with melt fractions between 0.15-0.3 (Figure 2.8B). The range of melt fractions predicted by this model corresponds to a temperature range of ~700-760 °C at 2 kbar and up to 770°C at 3 kbar as estimated by our MELTS calculations for a melt with ≥1 wt% H_2O. Given the uncertainties in partition coefficients and phase proportions, the modeled absolute abundances and REE enrichment/depletion may not match exactly what we see in the rinds, but this is not a major concern because it is the overall shape of the REE abundances (i.e., anti-correlated behavior of Eu relative to HREEs) that are of interest. These low melt fractions imply that the formation of the rinds must have taken place during the later stages of the Bernasconi magma chamber. Such extreme fractionation also explains the relative depletions in Sr seen in the rinds (Figure 2.4C) as Sr would be sequestered into plagioclase during earlier stages of the magma chamber.

Zircon saturation temperature estimates (Miller, 2003; Watson and Harrison, 1983) for the host rock provide a means of determining whether biotite-rich selvages and schlieren could have formed by direct crystallization of the host magma as opposed to enclave-magma reactions. We calculate zircon saturation temperatures of ~850 °C, which represent minimum bounds on temperature. These temperatures are above the thermal stability of biotite for the pressures considered here (Miller, 2003; Patino Douce and Harris, 1998; Spear, 1995). This suggests that the host magma had not stabilized biotite at the time of zircon saturation. The fact that large concentrations of biotite within the host rock, such as enclave rinds and schlieren, are only observed in association with enclaves and that, elsewhere, biotite is only a scarce intergranular

phase suggests that most of the biotite is produced by enclave-residual melt reactions late in the crystallization history of the magma.

2.7.3 Reaction-limited mixing and the origin of schlieren

Enclave-rind relations observed in the field demonstrate that new rinds form by continuous influx of residual liquids/fluids into the enclave as older rinds are eroded from the parent enclave (Figure 2.1B). Thus, mechanical mixing and rind formation appear to be coupled. Our measurements of enclaves and biotite-rich selvages indicate that biotite-rich rinds can preferentially deform because they are rheologically weak compared to the solid enclave interior (Figure 2.2). The high viscosity contrast between the solidified enclaves and host magma instead causes enclaves to act as brittle, semi-rigid bodies that do not efficiently mix into the felsic host magma, but rather rotate within the magma. Rinds on the other hand can be mechanically mixed and more easily homogenized into the host magma, potentially enabling mafic-felsic mixing of otherwise solid mafic enclaves. Similarities in the mineralogy and texture of rinds, selvages and schlieren strongly support the hypothesis that rinds erode from enclaves, become selvages and develop into schlieren with increasing strain as illustrated in Figure 2.6. In some cases attenuation is so extreme that schlieren are almost texturally indistinguishable from the host monzogranite

Deformable, biotite-rich rinds can only form when the following conditions are met: 1) K_2O and H_2O activities in the residual liquids are high enough to stabilize biotite, 2) transport rates of K or residual liquids into the rind are fast enough to facilitate continuous reaction, and 3) enclaves and host magma must be within the thermal limit of biotite stability. The first condition

implies that the formation of biotite-rich rinds does not occur in dry felsic systems, so mixing basalts into dry rhyolites would be predicted to be inefficient. Water may therefore play a fundamental role in the formation of rinds. Our thermodynamic calculations indicate that once a free fluid phase is formed, that is, once the residual melt is water-saturated, the system exhibits eutectoid behavior and temperature is buffered over a large range of melt fractions (Patiño Douce and Johnston, 1991; Vielzeuf and Holloway, 1988) as seen by the increasing nonlinearity of F versus T with increasing water contents (Figure 2.9). This is because the release of latent heat of crystallization is delayed to low temperatures rather than uniformly released throughout the entire crystallization interval (Figure 2.9). Additionally, if the melt is saturated in H_2O it can remain mobile for a longer period of time, allowing more time for rind-forming reactions to take place as well as erosion and deformation of eroded rinds. The presence of a free-fluid phase may also increase the rate of rind formation because chemical diffusivities are faster in water than in silicate melts, thus satisfying the second condition above. Enclaves and the host magma are likely at thermal equilibrium during the later stages of a magma chamber (i.e. when rinds are predicted to form), and our thermodynamic calculations suggest that both are within the thermal stability of biotite by that time, thus satisfying the third condition above. Reactive formation of rheologically weak rinds may be the rate-limiting step for efficient homogenization of mafic materials in felsic-dominated systems. We suggest that schlieren deformation fabrics and orientations reflect late-stage magma chamber processes involving flow of a crystal-rich mush.

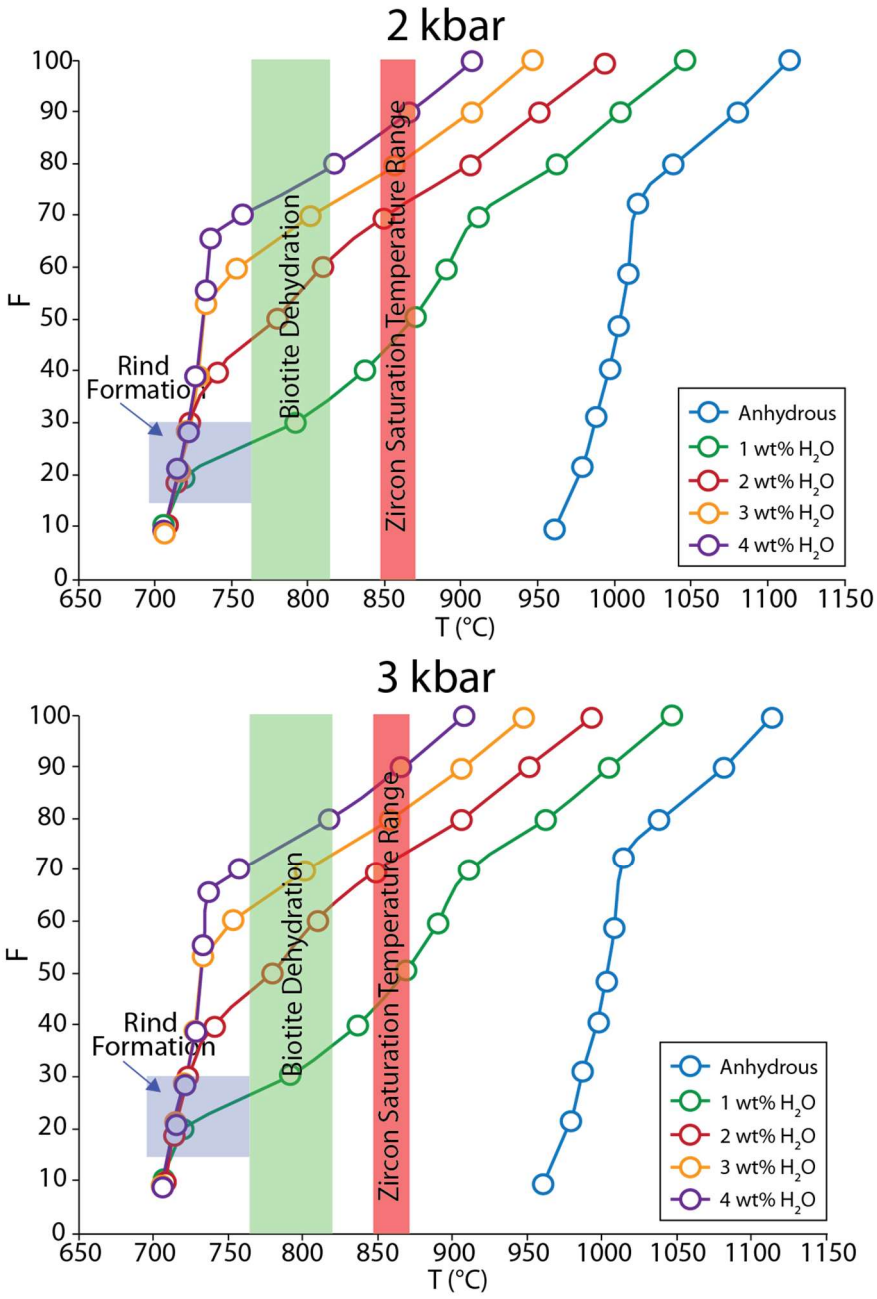

Figure 2.9. Rind formation constrained by crystallization models of host monzogranite using MELTS (Ghioros and Sack, 1995; Asimow and Ghiorso, 1998) and biotite thermal stability (Spear, 1995; Patiño Douce and Harris, 1998; Miller et al., 2003). Increasing H_2O content in the melt results in eutectic-like behavior by delaying the release of latent heat of crystallization and causing temperature to be buffered over larger ranges of melt fraction. This is crucial in maintaining continuous reaction and may be important for forming schlieren. Zircon saturation temperature estimates (Watson and Harrison, 1983; Miller et al., 2003) indicate that the host monzogranite was emplaced at temperatures above the thermal stability of biotite, thus indicating that the biotite in rinds was produced by reaction.

2.7.4 Reactive processes and implications for the formation of intermediate rocks

Reaction between mafic and felsic phases has been alluded to by others as a potentially important process in the generation of intermediate magmas. Chapman (1962) proposed the concept of a pseudo-chill margin on diabase dikes at Mount Desert Island, Maine. Although these dikes have a greater abundance of primary mafic minerals (pyroxenes, olivine) compared to the enclaves described here, the pseudo-chill margins share some petrographic characteristics with biotite-rich rinds. For example, both are finer-grained and more biotite-rich than associated mafic rocks. Chapman suggested that these margins formed by recrystallization at the dike-granitoid contact and do not necessarily represent true chill margins. This view was largely dismissed (Blake et al., 1965; Walker and Skelhorn, 1966), but our results support the suggestion by Chapman that these rinds are not isochemical chill margins. More recently, Beard et al. (2005) showed that silicic magmas can be generated by reaction between basalts and crustal xenoliths. Interestingly, they also observe that amphibole and biotite are both products of reactive processes.

In addition to work by Chapman (1962) and Beard et al. (2005), other previous studies have noted fine-grained biotite-rich rinds along enclaves and mafic intrusions (Bishop, 1963; Blake et al., 1965; Frost and Mahood, 1987; Furman and Spera, 1985; Pabst, 1928; Sisson et al., 1996; Wiebe, 1994; Wiebe et al., 1997). The fact that biotite-rich rinds have been observed in a variety of felsic plutons suggests that reactive processes may play a role in generating intermediate compositions and implies that the reactive processes recognized in the Bernasconi Hills pluton occur elsewhere as well. However it remains to be seen whether mixing, even with the help of reactive processes, is the dominant mechanism by which intermediate magmas are formed.

2.8 Conclusions

We have shown that fine-grained, biotite-rich rinds on mafic enclaves are generated by reaction between solid mafic enclaves and a residual melt or fluid and that these rinds erode from enclaves to mix with the host magma. This is in contrast to previously proposed hypotheses of isochemical quenching, binary mixing, and in-situ differentiation and is supported by the following evidence: 1) rinds are more potassic (~1.6-2.6 wt%), more mafic (~3.4 wt% MgO and ~12-13 wt% Fe_2O_3, respectively), and more encriched in REEs than both enclaves and host monzogranite; 2) enclaves are mineralogically zoned with biotite-rich rinds mantling hornblende and quartz-rich interiors; 3) hornblende is often most abundant within the enclave interior, adjacent to rinds and is suggestive of textural re-equilibration; 4) rinds are observed eroding from enclaves into the host magma followed by the formation of new rinds on freshly eroded surfaces throughout the strain history of an enclave; 5) differences in aspect ratios of enclaves and biotite-rich selvages (petrographically equivalent to rinds) indicate that rinds are preferentially deformed and may be mechanically mixed into the host magma.

Petrographic observations and phase relations show that rind formation can only occur when the following conditions are met: 1) K_2O and H_2O activities in the residual liquid are high enough to stabilize biotite, 2) enclaves and magma are within the thermal stability limit of biotite, and 3) transport rates of K into the enclave are fast enough to facilitate reaction before the host magma becomes rheologically locked. Rare earth element enrichments in rinds suggest that rinds form at low melt fractions (F=0.15-0.3) and thermodynamic calculations indicate that reactions take place over a temperature range of 700-770°C and thus late in the life of the magma body when much of the bulk magma is crystallized. However, the eutectic-like behavior of H_2O-

saturated melts (Figure 2.9) suggests that the host melt may remain rheologically active over a range of F within this temperature interval.

Our model of reaction-limited mixing indicates that schlieren in the Bernasconi Hills Pluton represent the mechanical mixing of eroded rinds into the host magma and suggests that structures associated with schlieren are representative of late-stage magmatic processes rather than conditions of emplacement. Because mafic-felsic mixing is limited by these late-stage chemical reactions, it seems likely that mixing of mafic magmas into felsic host magmas is not efficient unless the life of a magma chamber can be prolonged just above its solidus.

Chapter 3

Geochemical signals of mafic-felsic mixing: case study of enclave swarms in the Bernasconi Hills pluton, California[2]

[2]This chapter is in review for the Geological Society of America Bulletin as Farner, M.J., Lee, C.-T.A., Mikus, M.L. "Geochemical signals of mafic-felsic mixing: case study of enclave swarms in the Bernasconi Hills pluton, California".

Mafic enclaves are ubiquitous in granitic plutons and represent evidence of mingling between mafic and felsic magmas. To better understand whether such mingling, as seen on the outcrop scale (m), plays an important role in the generation of intermediate magmas at the crustal (>km) scale, we characterize geochemical signatures of mixing through a fine-scale geochemical study of a mafic enclave swarm (Bernasconi Hills in the northern Peninsular Ranges Batholith, California USA). The enclaves are basaltic to andesitic in composition and occur as angular to rounded clasts and as highly attenuated schlieren within a host pluton with silica contents ranging from dacitic to rhyolitic in composition. Centimeter to meter-scale sampling shows clear textural, mineralogical and compositional evidence for incipient mixing between the mafic enclaves and felsic host. The enclaves and host magmas define linear element-element arrays between the basaltic enclaves and dacitic end-member of the host magma (65-70 wt. % SiO_2). In particular, crystal fractionation generates strongly arcuate P_2O_5-SiO_2 differentiation trends, so the linear arrays here are interpreted to reflect local scale mixing. Plagioclase phenocrysts within the host pluton are homogeneous, showing no evidence for reverse zonation typical of mafic recharge or reheating. This indicates that the enclaves were entrained as cold, solidified xenoliths rather than as hot, basaltic liquids, and that entrainment likely occurred near the end of the magma's thermal life, providing too little time for the host magma and its phenocrysts to have

chemically registered the entrainment of mafic enclaves. As such, mixing appears to have been largely mechanical, driven by flow within the magma body. However, despite textural and bulk rock geochemical evidence for local mixing, variation diagrams, such as K_2O and Zr versus SiO_2, clearly indicate that the most silicic components of the pluton (>70 wt. % SiO_2) did not participate in mixing. These highly silicic components are last stage residual liquids, which were locally and internally expelled, after the pluton had crystallized to the point at which the magma body locked up, terminating mechanical mixing. Finally, our case study of local scale mixing may shed some light on crustal scale geochemical systematics of arc crust. While P_2O_5-SiO_2 systematics at Bernasconi Hills show linear mixing arrays between basaltic and dacitic end-members, arc volcanic rocks tend to show arcuate patterns, suggesting that crystal fractionation explains most of the spectrum of arc lavas, including intermediate lavas, with mafic-felsic mixing playing a small role. Arc plutonic rocks, however, show both arcuate and linear arrays, suggesting that mixing may become more important during pluton formation and evolution.

3.1 Introduction

Mafic enclaves have been observed within felsic intrusive and extrusive rocks globally, motivating the notion that physical interaction of compositionally distinct magmas (mingling) is a common occurrence (Bacon, 1986; Clynne, 1999; Didier, 1973; Eichelberger, 1975; Frost and Mahood, 1987; Furman and Spera, 1985; Pabst, 1928; Vernon, 1984). In some instances, as illustrated by petrographic, geochemical and fluid dynamical studies, discrete magmas may mix to produce a compositional hybrid of the parental end-member magmas (Bacon, 1986; Clynne, 1999; Eichelberger, 1975; Frost and Mahood, 1987; Furman and Spera, 1985; Snyder and Tait, 1995). Such mafic-felsic magma mixing has been proposed to be an important mechanism in

producing andesitic magmas based upon the ubiquity of enclaves in igneous rocks, lack of intermediate melt inclusions observed in arc lavas, linear element-element arrays commonly observed between related mafic and felsic rocks and the abundance of plagioclase with resorbed textures in arc andesites (Bacon, 1986; Barbarin, 2005; Clynne, 1999; Eichelberger, 1975; Kent et al., 2010; Reubi and Blundy, 2009; Tepley et al., 1999). However, given the rheological and thermal contrasts between mafic and felsic melts (Frost and Mahood, 1987; Hodge and Jellinek, 2012; Ratajeski et al., 2001; Sparks and Marshall, 1986), efficient mafic-felsic mixing likely only occurs in basalt-dominated systems. Whether significant quantities of intermediate magmas, which require larger proportions of felsic magmas, can be generated is unclear.

To better define the geochemical characteristics of mixing, we examine here field relationships and geochemical systematics of mafic enclaves and host felsic granitoids in the Bernasconi Hills pluton, in the northern Peninsular Ranges Batholith in California (USA). The Bernasconi Hills pluton provides an excellent opportunity to examine mafic-felsic interaction because it has abundant mafic enclaves, is well exposed by quarrying and has been suggested as a clear example of magma mixing based upon petrographic studies and mineral chemistry (Mason and Cohen, 1990). We documented the field and geochemical relationships between mafic enclaves and host granitoids at 5 m increments along two measured transects through the quarried interior of the pluton. The mafic enclaves and host magma show evidence for incipient mechanical mixing, but the homogeneity of plagioclase phenocrysts in the host magma suggests that the enclaves were entrained as solid xenoliths and that entrainment occurred near the thermal death of the magma body. We discuss the results of our case study in the context of crustal-scale studies of the composition of arc lavas and plutons.

3.2 Geological Setting

3.2.1 Peninsular Ranges Batholith

The Peninsular Ranges Batholith was part of an extensive Mesozoic magmatic arc along the margin of western North America, caused by subduction of the Farallon Plate beneath the North American Plate (Figure 3.1) (Busby, 2004; Lee et al., 2007; Morton et al., 2014). The batholith intruded during the Cretaceous (125-85 Ma) and extends roughly 1500 km from Riverside, California, USA to the southern tip of the Baja California peninsula (Morton et al., 2014; Premo et al., 2014). Based upon field and geochemical studies, the batholith is generally divided into western and eastern portions (Baird et al., 1979; DePaolo, 1981; Gromet and Silver, 1987; Lee et al., 2007; Morton et al., 2014), where the boundary between the two is inferred to represent a tectonic suture between an accreted pre-batholithic island arc terrane to the west and Paleozoic North American craton to the east (Figure 3.1) (Busby, 2004; Lee et al., 2007; Morton et al., 2014). Recently, Morton et al. (2014) have subdivided the western and eastern portions of the batholith based upon extensive geologic, petrologic, structural and geochemical data. For simplicity, we retain the older west-east dichotomy in describing batholithic trends, but note that in this paper, the western Peninsular Ranges encompasses the older western zone, younger western zone and western transition zone defined by Morton et al. (2014). Similarly, the eastern Peninsular Ranges referred to here includes the eastern transition zone and eastern zone of Morton et al. (2014).

Plutons in the western Peninsular Ranges Batholith intruded through an accreted island arc terrane and emplaced at shallow to mid-crustal depths (2-6 kbar), based upon Al-in-hornblende barometry (Ague and Brimhall, 1988; Morton et al., 2014). The western plutons span

most of the intrusive history of the batholith (~125-95 Ma) and exhibit a continuous geochemical differentiation trend from gabbroic compositions through highly evolved granites (Lee and Morton, 2015; Lee et al., 2007; Morton et al., 2014; Premo et al., 2014). Despite extensive geochemical evolution, radiogenic isotopic studies show that initial $^{87}Sr/^{86}Sr$ for the western Peninsular Ranges is uniformly low (Kistler et al., 2014).

East of the suture, plutons intruded into the North American continent and were emplaced at mid-crustal depths (4-6.5 kbar), based upon Al-in-hornblende barometry (Ague and Brimhall, 1988; Morton et al., 2014). Eastern plutons were emplaced late (~95-85) in the history of the batholith compared to the western plutons and are more compositionally evolved, on average. The eastern plutons also exhibit a more restricted geochemical range (tonalite to granite) compared to their western counterparts, which has in part been attributed to assimilation of pre-existing lithologies (DePaolo, 1981; Lee et al., 2007; Morton et al., 2014).

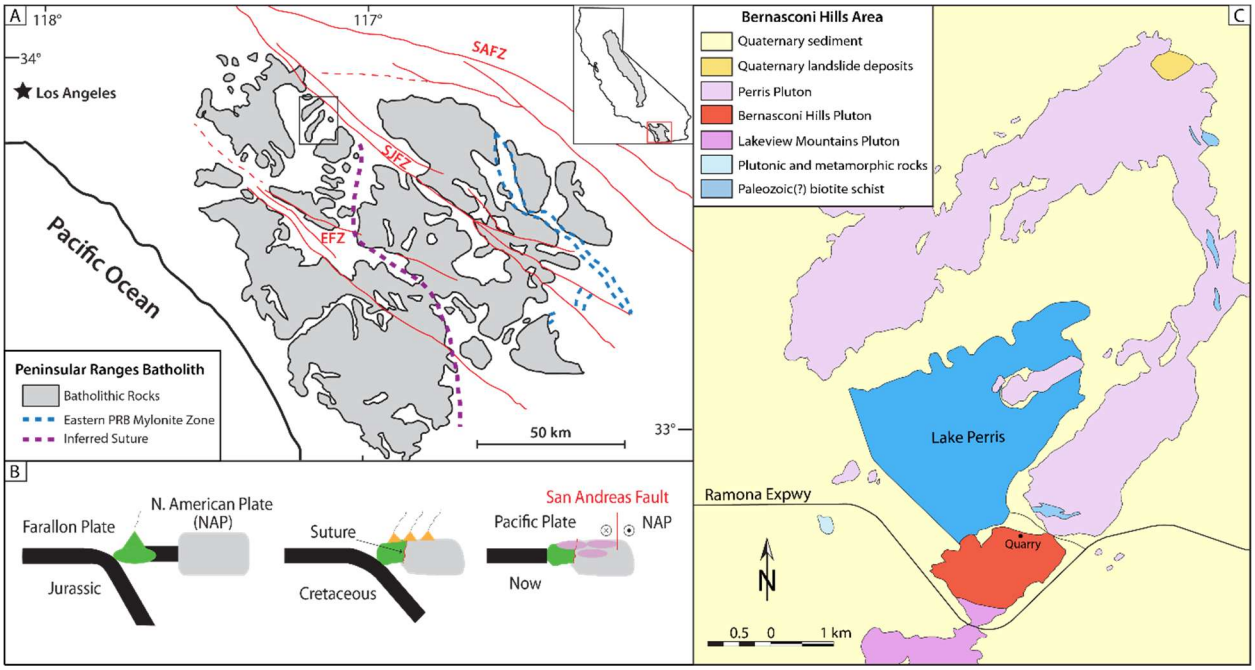

Figure 3.1. (A) Location of the northern Peninsular Ranges Batholith (PRB) and major tectonic features in the region (simplified from Kistler et al. (2014)). The batholith is divided into three tectonic blocks (from west to east:

Santa Ana, Perris and San Jacinto blocks) by right lateral strike-slip motion along the Elsinore (EFZ) and San Jacinto (SJFZ) Fault Zones, which strike sub-parallel to the San Andreas Faults Zone (SAFZ). (B) Schematic tectonic history of the Peninsular Ranges Batholith from the Jurassic to the present day illustrating suturing of an island arc to the North American Plate (NAP) and subsequent intrusion of the batholith. (C) Geologic map of the Bernasconi Hills pluton and surrounding area with the location of the quarry (after Morton and Matti, 2001 and Morton, 2003).

3.2.2 Bernasconi Hills pluton

The Bernasconi Hills pluton (33.839° N, 117.168° W) is a ~2 km^2 wide (Mason and Cohen, 1990) granitic intrusion exposed near the city of Moreno Valley, California (USA), in the northern Peninsular Ranges, west of the suture (Figure 3.1). The pluton is composed of biotite-hornblende-granite and granodiorite with smaller amounts of tonalite present. Fine-grained mafic enclaves are common throughout the pluton and occur within dense swarms and individual bodies as angular to rounded clasts within the host granitoid and range in size from centimeters to over a meter along the long axis (Figure 3.2). Enclaves occur throughout the pluton and are characterized by fine-grained biotite-rich rinds on their margins and equigranular cores dominated by quartz and plagioclase (Farner et al., 2014; Mason and Cohen, 1990). Enclave rinds are often associated with schlieren, which are particularly abundant adjacent to enclave swarms and larger (> 1 m) enclaves.

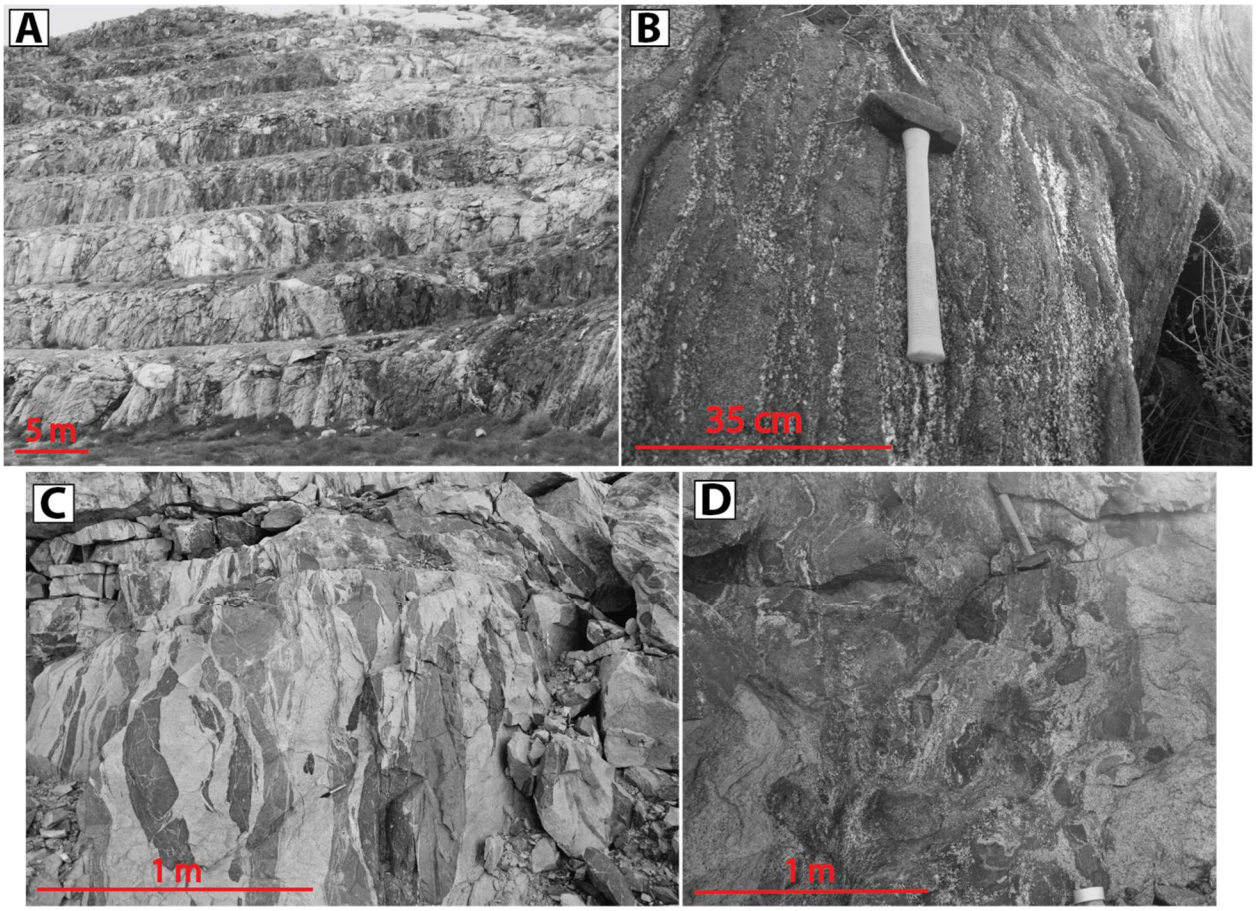

Figure 3.2. (A) Partial view of the quarried section of the Bernasconi Hills pluton with a large enclave swarm within the host granitoid. Individual terraces are ~3 m high for scale. (B) Close-up view of a dense enclave swarm near the quarry (hammer is approximately 35 cm long). (C) Enclave swarm within the quarry with some slightly attenuated enclaves (pen is approximately 10 cm long). (D) Sheared enclaves and associated schlieren.

This study focuses on a recently quarried portion of the pluton because it provides a continuous cross section through the pluton, from the margin to the center. The main face of the quarry has been cut into terraces and is approximately 170 m across and 140 m high from the quarry floor. The quarry wall exhibits enclave swarms ranging in width from a few meters across up to ~ 15 m with variable mafic/felsic material ratios. Additionally, the quarry also exposes evidence of intimate mingling between mafic and felsic materials.

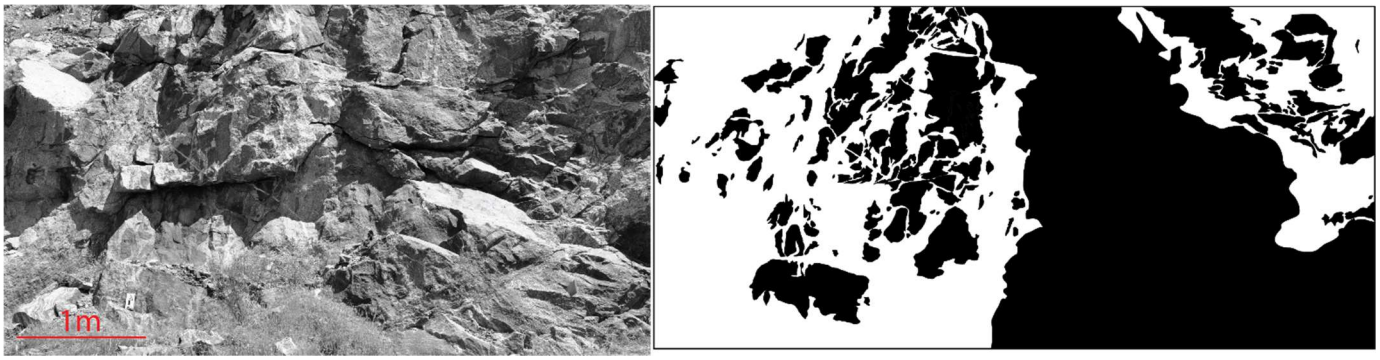

Figure 3.3. Field photo and corresponding outcrop map from one section of our sampling transects showing a large mafic body being disaggregated into mafic enclaves.

3.2.3 Petrography

Enclaves

Mafic enclaves in the Bernasconi Hills pluton are mineralogically zoned between a biotite-rich outer rind and biotite-poor interior. The interior portion is composed of quartz (~35 %), plagioclase (~20 %) and hornblende (~32 %) with rare biotite (~13 %). Quartz generally occurs as equigranular grains and is most abundant near the enclave center. Plagioclase is present as subhedral grains and occurs in roughly equal proportions throughout the enclave, with no distinct gradation in abundance. Hornblende is the most common silica-poor mineral in the enclave interior and typically forms clots of anhedral deep green to brown crystals around quartz and plagioclase. Notably, hornblende is most abundant near the enclave interior-rind boundary, and gradually decreases in abundance toward the center of the enclave interior. Biotite is not common in the enclave interior, but when present it occurs as subhedral to euhedral yellow-brown crystals and is observed in association with hornblende.

Enclave rinds are defined by their very fine-grained texture, higher proportion of silica-poor minerals and high biotite content (30 %). Biotite occurs as subhedral to euhedral yellow-brown crystals oriented parallel to the rind-host contact. Additionally, biotite is most abundant near the rind-host rock

contact and becomes less common going towards the rind-enclave interior boundary. Quartz (~35 %) and plagioclase (~10 %) are also present in the rinds and generally occur as equigranular crystals aligned parallel to biotite sheets. Hornblende (25 %) occurs as stubby green-brown crystals and is aligned subparallel to biotite. These observations were previously reported by Farner et al. (2014), who interpreted the rinds as reaction products between the mafic xenolith and late residual silicic liquids in the host magma.

Granitoids

We identify two groups of host granitoid rocks based upon the presence of K-feldspar. K-feldspar-bearing rocks contain (1-3 mm) subhedral to euhedral K-feldspar phenocrysts (~22 %), subhedral plagioclase (~26 %), anhedral quartz (~ 40 %) and rare biotite and hornblende (~2 % each). K-feldspar phenocrysts are generally inclusion-free, but do contain occasional inclusions of rounded quartz. Symplectic intergrowths of K-feldspar and quartz as well as myrmekite are common along the margins of K-feldspar phenocrysts and only occur in K-feldspar-bearing rocks. Interestingly, K-feldspar-bearing granitoids are primarily observed near the center of the intrusion as K-feldspar is virtually absent everywhere else. In comparison, K-feldspar-absent rocks compose the bulk of the pluton and are composed of quartz (~ 41 %) and plagioclase (~42) with small amounts of biotite (~6 %) and hornblende (~5 %). Quartz and plagioclase both occur as large anhedral grains with biotite and hornblende as small subhedral interstitial phases.

3.3 Methods

3.3.1 Sampling methods

Samples were collected along two linear transects (60 m and 120 m long, respectively) across the quarried face of the pluton (Figure 3.2). Each transect was subdivided into individual 5 m-wide segments. Samples of both the host granitoid and adjacent enclaves (when present) were taken from each segment in order to directly compare spatially associated host and enclave

compositions. Additionally, the proportion of mafic to felsic material was estimated for each segment. In the field, enclaves were identified as fine-grained, dark gray clasts enclosed within lighter, coarse-grained host rocks. Enclave rinds were distinguished by their very fine-grained texture, abundance of biotite and close spatial association to enclaves. Schlieren were defined by their highly attenuated shape (up 1 m long), fine-grained texture and occurrence along the margins of enclave swarms or as isolated bodies within the host pluton.

3.3.2 Whole-rock geochemistry

Fused glass disks were prepared for each sample beginning by grinding rock fragments in a ceramic Spex mill until a fine-grained powder was obtained. Following this, 3.5 g of sample powder was mixed with 7.0 g of dilithium tetraborate ($Li_2B_4O_7$) and the mixture was quantitatively transferred to a graphite crucible. The mixture was then heated to 1000°C in a furnace for five minutes and quenched. Each fused disk was then crushed and re-fused to dissolve any remaining mineral inclusions.

Major element compositions were determined for all fused glass disks by wavelength dispersive X-ray fluorescence spectrometry (XRF) with a ThermoARL Advant'XP+ sequential X-ray fluorescence spectrometer at Washington State University, Pullman. Fused glass disks of United States Geological Survey (USGS) rock standards AVG-1, BCR-1, BIR-1, DNC-1, G-2, GSP-1, STM-1, PCC-1 were used as external standards. Rock standards BCR-P and GSP-1 were measured after every 28 unknown samples to monitor in-run precision (Johnson et al., 1999).

Minor and trace element concentrations were determined at Rice University for the same glass disks analyzed by XRF using laser ablation inductively coupled plasma mass spectrometry (LA-ICP-MS) with a ThermoFinnigan Element 2 magnetic sector mass spectrometer equipped

with a New Wave 213 nm laser ablation system in medium mass resolution mode (m/Δm ~4000). Prior to measurement, the instrument was tuned by controlling the flow of the sample gas (Ar) to achieve a sensitivity of ~250,000 cps on 15 ppm La in USGS basaltic glass standard BHVO2g in low-resolution mode with a 55 μm diameter spot size. When measuring samples, the laser was operated with an 80 μm diameter spot size, 10 Hz pulse frequency, ~11-15 J/cm^2 fluence and sample gas (He) flow rate of ~850 mL/min. External standards used were USGS basaltic glass standards BHVO2g, BIR2g and BCR2g. Raw data were converted to concentrations using an in-house data reduction program (http://cintylee.org/s/Laser-RAWDATA-TEMPLATE.xls) that subtracts background signal intensities and elemental fractionations with external standards from the measured signal. Signal intensities were then normalized to an internal standard (^{30}Si) and time-resolved intervals were integrated to yield elemental concentrations.

3.3.3 Chemistry of plagioclase in host granitoid

Compositional transects were constructed for plagioclase phenocrysts in 150 μm-thick polished thin sections of host granitoid samples, using the same LA-ICP-MS set-up described above in medium mass resolution mode with a 55 μm spot size. External standards used were USGS glass standards BHVO2g and BCR2g with ^{43}Ca as an internal standard. Each crystal was measured from rim to rim along a linear transect with no gaps between individual 55 μm spots. Inclusion-ridden crystals were avoided as much as possible, but when necessary, we measured parallel to the main transect to avoid small inclusions.

3.3.4 Micro-XRF elemental maps

Elemental mapping of individual plagioclase crystals in 150 μm thick sections of granitic samples was carried out with a Horiba XGT-7200 X-ray analytical microscope at Rice University (see Jiang et al., 2015 for additional details). Mapping was performed under full vacuum conditions, using a 50 μm capillary, accelerating voltage of 30 kV and 400 s survey time over 3-4 accumulations.

3.4 Results

3.4.1 Major element geochemistry

Whole-rock compositions for all samples are reported in Appendix B and major element oxide variation diagrams are shown in Figure 3.4. Most of the host granitoid samples show limited compositional variation and plot as a cluster for all major element oxides except Na_2O and K_2O (Figure 3.4). There is substantial scatter with respect to K_2O contents, with compositions differing by 1-3 wt. % at a constant SiO_2 content. In particular, when $SiO_2 > 72$ wt. %, K_2O appears to increase and decrease simultaneously. While the majority of granitoid samples plot within a single cluster, four samples have similar compositions to adjacent mafic enclaves. These samples are from a ~ 15 m wide, dense enclave swarm that cross-cuts the quarried section of the Bernasconi Hills pluton (Mason and Cohen, 1990; Morton et al., 2014) and despite the compositional similarity to enclaves, host rocks associated with this swarm are texturally distinct from the enclaves and were distinguished by their coarse texture and lighter color compared to adjacent enclaves.

The mafic enclaves span a wide array of compositions compared to their host granitoids and range from basaltic to andesitic bulk compositions. Some of the more SiO_2-rich enclaves approach similar compositions to host rocks, but do not overlap with the main group of host

compositions (Figure 3.4). The least evolved enclaves generally occur in association with enclave swarms and large (> 1 m wide) globular bodies of mafic material intruded into the host pluton. Enclaves show a wide range of Na_2O contents at a given SiO_2 that decreases with increasing SiO_2. Enclave rinds have similar SiO_2 to enclaves, but are enriched in K_2O and FeO^* because they contain markedly more biotite than enclaves. Additionally, the rinds are comparatively depleted in CaO and MgO, which reflects a lack of hornblende. Schlieren have widely variable SiO_2 content, but broadly overlap with the enclaves and have similar K_2O, MgO and CaO to rinds.

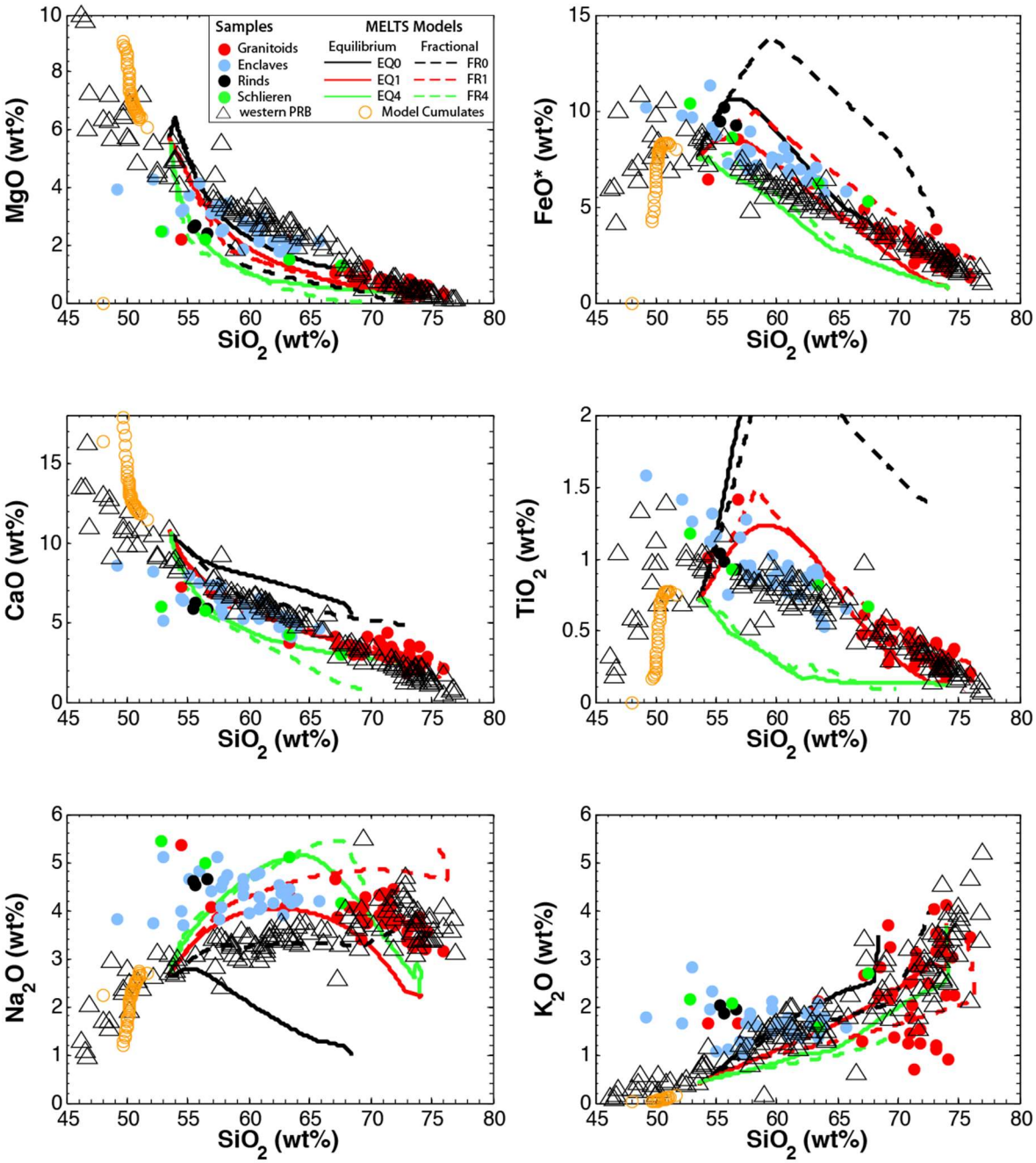

Figure 3.4. Major element oxide compositions (on an anhydrous basis) of host granitoids, mafic enclaves, enclave rinds and schlieren plotted with data compiled from the western Peninsular Ranges Batholith (WPRB) (Lee et al., 2007). Calculated liquid compositions from Rhyolite-MELTS computations for equilibrium (EQ) and fractional (FR) crystallization of a basaltic parental magma with 0 (black), 1 (red) and 4 (green) wt. % initial H2O are shown for comparison. Modeled cumulate compositions (open circles) for equilibrium fractionation with 1 wt. % H_2O are shown (corresponding to solid red line).

3.4.2 Trace element geochemistry

Whole-rock concentrations for Zr are reported in Appendix B and P_2O_5, and Zr versus SiO_2 trends are shown in Figure 3.5. We observe a broadly linear trend between host granitoids and mafic enclaves with respect to P_2O_5 versus SiO_2 (Figure 3.5). The P_2O_5 and SiO_2 contents of the host granitoids generally overlap with the compiled data from the western Peninsular Ranges, although a few samples plot away from the main group. Mafic enclaves have slightly less P_2O_5 compared to the granitoids and plot just under the main trend defined by the compiled western Peninsular Ranges Batholith data (Figure 3.5). We also observe limited overlap between enclaves and granitoids with respect to Zr versus SiO_2. There is a broadly linear array between enclaves and dacitic compositions of the host granitoid (<70 wt. % SiO_2) (Figure 3.5). Zr contents of granitoids with >70 wt. % SiO_2 decrease with increasing SiO_2 and do not fall on the linear array defined by the enclaves and the dacitic components of the host granitoid.

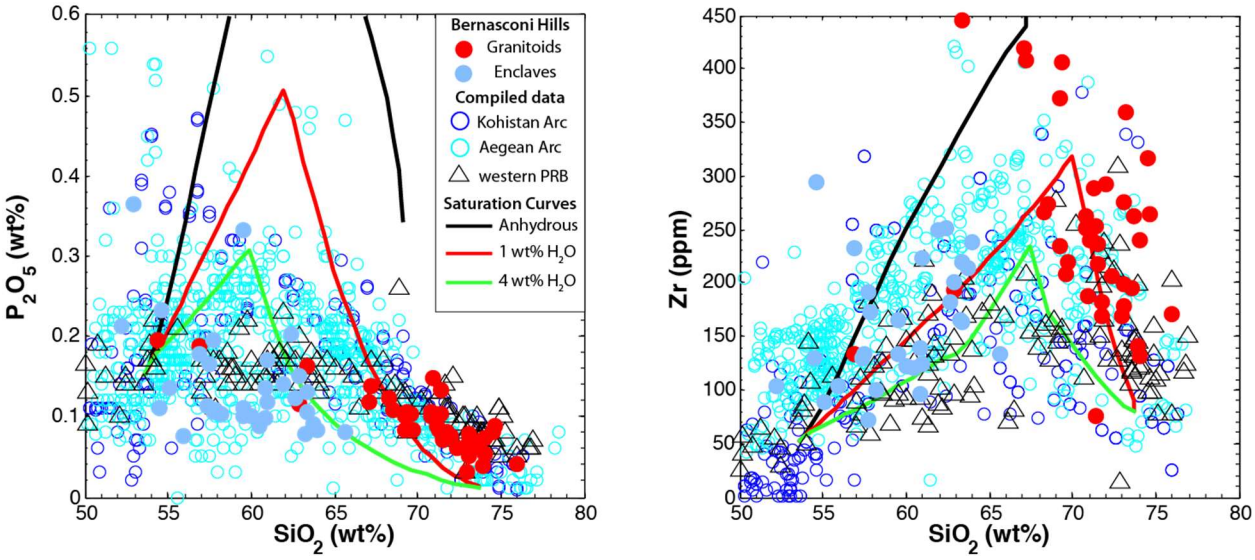

Figure 3.5. P_2O_5 and Zr systematics of granitoids and enclaves from the Bernasconi Hills pluton with data compiled for the western Peninsular Ranges Batholith, Kohistan arc section and Aegean Arc lavas. Calculated apatite and zircon saturation curves are plotted for anhydrous, 1 and 4 wt% H_2O at 0.4 GPa.

3.4.3 Compositional transects of plagioclase in host granitoid

Individual spot measurements from each plagioclase transect are reported in Appendix C and rim-to-rim profiles for each phenocryst are shown in Figure 3.6. The relatively flat compositional profiles show that all of the plagioclase crystals are unzoned. This homogeneity is also observed in micro-XRF maps of Ca and K in individual crystals (Figure 3.7).

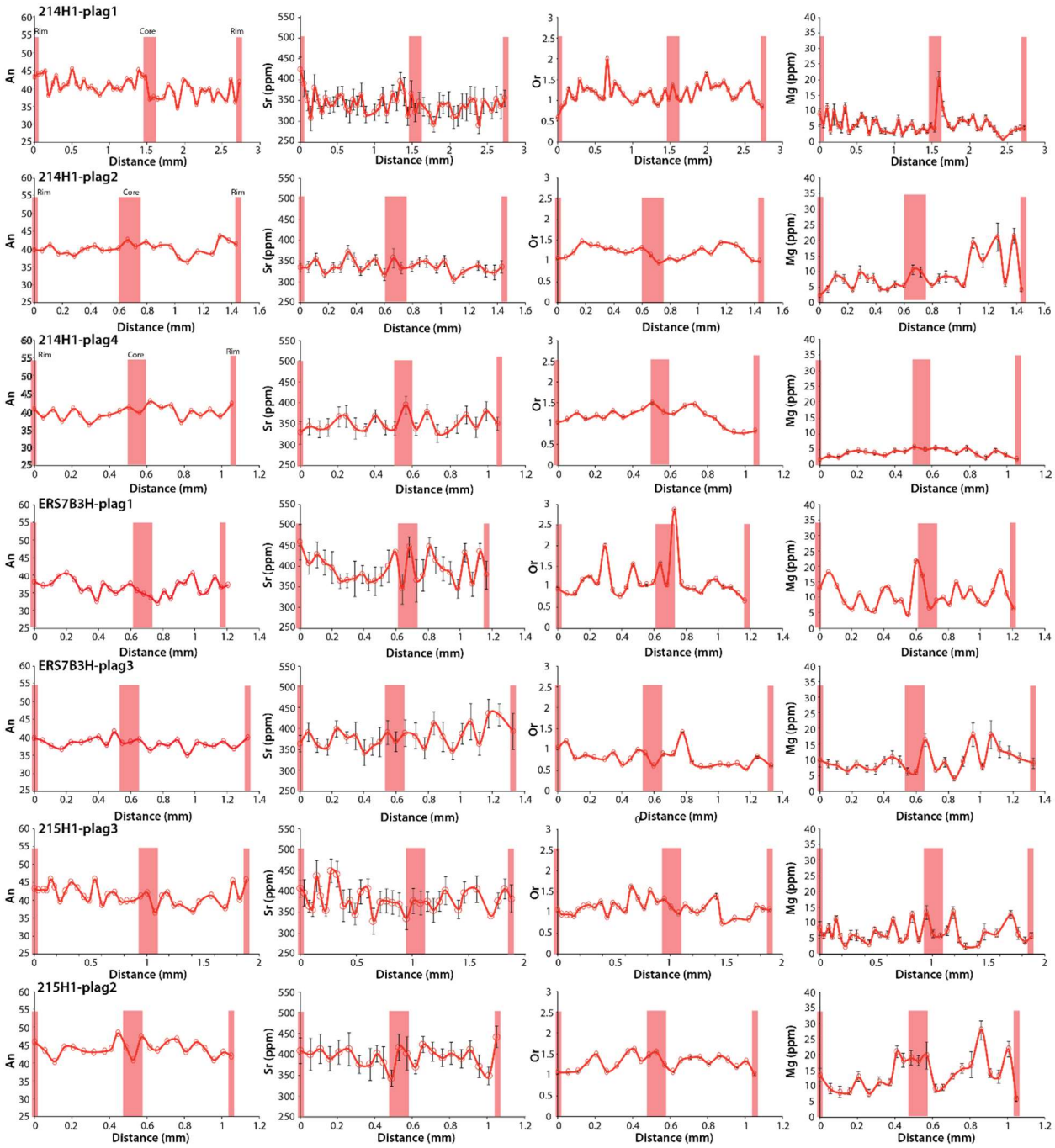

Figure 3.6. Compositional transects across plagioclase phenocrysts in granitoid samples with rim and core locations denoted by transparent red bars. Phenocrysts near and away from mafic enclaves were examined, but the relatively flat, unzoned profiles shown here indicate that the crystals do not record any mafic recharge events.

3.5 Discussion

3.5.1 Textural constraints on the origin of the enclaves

Mafic enclaves may originate through several processes including (1) quenching of discrete globules of basaltic magma against cooler felsic host magma (Vernon, 1984; Wager and Bailey, 1953), (2) entrainment and alteration of wallrock xenoliths (Liao et al., 2013; Stimac et al., 1995), (3) entrainment of cogenetic cumulate xenoliths (Barbarin, 2005) and (4) disaggregation of mafic dikes (Barbarin, 2005). Because enclaves may form in a variety of ways, it is important to determine the petrogenesis of an enclave population when assessing their relationship to the host intrusion.

Textural and field relations provide some insights into the origins of the enclaves. The enclaves are fine-grained and equigranular, possibly consistent with rapid cooling. However, finer grained quench rinds are not observed. Instead, there are biotite-rich reaction rinds on all surfaces, including angular surfaces formed clearly by fracturing (Farner et al., 2014; Mason and Cohen, 1990). These observations likely exclude an origin by direct injection and quenching of hot mafic liquids into the felsic host. We suggest that the enclaves represent mafic rocks that were forcefully entrained by the host felsic magma. One possible origin is via entrainment of metamorphic country rock, but we find no textural or mineralogic relicts of metamorphic rocks in the enclave populations as has been described in other plutons, which show clear evidence for wallrock entrainment (Liao et al., 2013). We also do not see any cumulate textures in the enclaves as they are instead characterized by more equigranular textures (Farner et al., 2014). These observations suggest that the enclave protoliths were probably solidified mafic liquids, which were then forcefully entrained as solid clasts into the felsic host magma and disaggregated (Figures 3.2 and 3.3).

3.5.2 Major element constraints on origin of enclaves

The major element systematics of the Bernasconi enclaves and host magma overlap roughly with the Peninsular Ranges Batholith. In detail, CaO, MgO, TiO_2, and FeO^* decrease linearly with SiO_2 (Figure 3.4) while K_2O increases linearly with SiO_2, but shows a pronounced upwards kink in K_2O at ~70 wt. % SiO_2 in the Peninsular Ranges and Bernasconi pluton. The only significant differences in major element systematics between Bernasconi enclaves and the Peninsular Ranges Batholith are in Na_2O and to a lesser extent, K_2O in the most mafic samples. Enclave Na_2O contents are systematically higher at a given SiO_2 content than in Peninsular Ranges samples and K_2O appears to be enriched in some enclaves. We note, however, that these enrichments in Na_2O and K_2O could be due to very local reaction between the enclaves and the host magma, which generates biotite- and possibly alkali feldspar-rich reaction rinds (Farner et al., 2014).

These major element trends are typical of arc magmatic systems, but these trends can potentially be explained by mafic-felsic mixing or crystal fractionation. We first use the thermodynamic Rhyolite-MELTS program (Ghiorso and Gualda, 2015; Gualda et al., 2012) as a qualitative guide for evaluating whether the mafic enclaves and the felsic host could have once represented silicate liquids formed by crystal fractionation. We chose Rhyolite-MELTS because it is capable of modeling liquid fractionation from evolved basaltic to silicic compositions. There are limitations of using a thermodynamic program for liquid line of descent to model natural processes, which are certainly more complicated. Thus, we use modeling only to guide intuition, not to exactly reproduce observations. Calculations were made for isobaric equilibrium and fractional crystallization (liquid line of descent) scenarios at 0.4 GPa, which we adopted based upon Al-in-hornblende barometry by Ague and Brimhall (1988). An oxygen fugacity fixed at

the fayalite-magnetite-quartz buffer was assumed. We used a gabbro from the western Peninsular Ranges Batholith as an estimate of a primitive basaltic composition (as wt. %, 52.1 SiO_2, 0.68 TiO_2, 18.3 Al_2O_3, 7.24 FeO^*, 5.55 MgO, 10.5 CaO, 2.6 Na_2O, and 0.38 K_2O on a volatile-free basis) with 0, 1 and 4 wt % initial bulk H_2O content. This composition represents a differentiated basalt that is plausibly parental to more differentiated plutonic rocks in the western Peninsular Ranges Batholith (Lee et al., 2007; Morton et al., 2014). We avoided gabbro compositions that were known to form as cumulates based on textural evidence in the field. In any case, the parental composition chosen here does not represent a primary mantle-derived magma as no such magmas are preserved in the Peninsular Ranges Batholith.

The results of our calculations are shown in Figure3.4. It can be seen that the overall major element trends can be explained by crystal fractionation of a hydrous magma. In particular, the decrease in FeO^* and TiO_2, which is typical of calc-alkaline differentiation trends, can be explained by magnetite fractionation. The upwards kink in K_2O at ~70 wt. % SiO_2 can also be explained as extremely late residual liquids after crystal fractionation. What the enclaves probably cannot represent are cumulates from a mafic magma as their silica contents are too high. Both the enclaves and the felsic host compositions can thus represent liquids, though it is not necessary from the qualitative modeling here that they derive petrogenetically from the same parent. We conclude that the most mafic enclaves represent solidified fragments of former basaltic liquids entrained into a felsic magma. Both the basaltic and felsic end-members represent liquids generated by crystal fractionation.

The compositional smearing between the mafic enclaves and felsic host, however, can also be explained by mixing as binary mixing generates linear arrays in element-element variation diagrams. From thermodynamic modeling of crystal fractionation, it is not possible to

distinguish between crystal fractionation or mixing between mafic and felsic end-members to generate the linear geochemical arrays seen here. We will discuss additional evidence for mixing in the next section. However, we can state with confidence that mixing with the most silicic components (>73 wt. % SiO_2) in the host magma is precluded because such a process would generate a linear array in K_2O-SiO_2 space from 50 to >73 wt. % SiO_2, but a distinct upwards kink in K_2O at ~70 wt. % SiO_2 is seen. Mixing, however, between a mafic end-member and a less silicic end-member, such as a dacitic component (66-70 wt. % SiO_2), is not precluded by the foregoing discussion. We note that enclaves and host rocks within a large (~ 15 m wide) enclave swarm in the quarry wall with a high (45-80) mafic/felsic ratio have more similar major element compositions (Figures 3.2A and 3.4), but are texturally distinct; this suggests that there has been mixing between basaltic and dacitic end-members on the local (m) scale.

3.5.3 Phosphorus-zirconium systematics on origin of enclaves

To further evaluate whether the local compositional trends in our case study pertain to mixing or fractionation, we turn to P and Zr systematics. Apatite and zircon are the dominant rock-forming minerals in granitoids that contain P and Zr, respectively, as one of their main structural components, thus fractionation of P and Zr in magma is primarily controlled by the presence or absence of these minerals during crystal fractionation (Lee and Bachmann, 2014). P and Zr behave incompatibly when apatite and zircon have not saturated and then compatibly after saturation in these phases, generating distinctly nonlinear P and Zr versus SiO_2 variation diagrams. We apply the methods of (Lee and Bachmann, 2014) in our case study to further examine enclave-host granitoid relations. Apatite and zircon saturation curves were calculated using the solubility models of Harrison and Watson (1984); Watson and Harrison (1983) at 0.4 GPa (Ague and Brimhall, 1988), with initial P_2O_5 and Zr content of 0.15 wt. % and 52 ppm,

respectively, for the Rhyolite-MELTS fractionation series described above. These initial concentrations of P and Zr were determined from mafic liquid end-members inferred from PRB compositional data as described in Lee and Bachmann (2014). The major elements were modeled using Rhyolite-MELTS but Zr and P were post-processed by tracking Zr and P solubility.

Simple crystal fractionation leads to strongly kinked P and Zr versus SiO_2 variation diagrams, with P and Zr initially rising in the magma until a maximum is reached beyond which P and Zr decrease according to their solubilities when apatite and zircon become saturated (Figure 5). The peaks in P and Zr occur at different SiO_2 contents, owing to the different times at which apatite and zircon saturate. The Bernasconi enclaves and host magmas show no peak in P_2O_5-SiO_2, instead showing a decreasing linear trend in P_2O_5 from 55 to 70 wt. % SiO_2, a feature that can only be explained by mixing between a basaltic end-member (the enclaves) and a dacitic end-member (the host). As noted above from K_2O-SiO_2 systematics (Figure 4), there is no evidence in P_2O_5 of mixing with the most silicic (>70 wt. % SiO_2) parts of the magma host. In terms of Zr, we see an increasing linear trend between the enclaves and dacitic compositions, but because the peak in Zr during crystal fractionation occurs at higher silica contents than P, the observed linear trend can be explained by both fractionation and mixing. Again, what is clear from Zr-SiO_2 systematics is that there is no mixing with the highest silica end-members in the host. Collectively, all the geochemical and textural data suggest that enclaves and a dacitic host magma mingled and partly homogenized on the cm to meter scale. During or after this local homogenization, the last residual liquids, rich in silica (>70 wt. % SiO_2) were expelled locally, but such liquids did not participate in any mixing or homogenization.

Following Lee and Bachmann (2014), we have plotted volcanic and plutonic rocks on the P and Zr diagrams for completeness. Shown are volcanic rocks from the Aegean arc (GEOROC database; http://georoc.mpch-mainz.gwdg.de/georoc/) and plutonic rocks from the Peninsular Ranges Batholith (Lee et al., 2007) and the Kohistan arc section (Jagoutz, 2014; Jagoutz et al., 2009). It can be seen that volcanic rocks follow the crystal fractionation lines: P in volcanic arcs is higher than that defined by mafic-felsic mixing. However, it is clear that some plutonic rocks fall in between the mixing array defined by the Bernasconi enclaves and the crystal fractionation curves defined by volcanic rocks and crystallization modeling. Lee and Bachmann (2014) did not discuss the significance of these differences between volcanic and plutonic P-SiO_2 systematics. However, in light of the results of this study on the Bernasconi enclave swarm, which shows distinct mixing, the difference between volcanic and plutonic rocks is likely important. Our observations suggest that extrusive rocks follow liquid lines of descent, from basalt to rhyolite, with little or no extensive mixing (Bachmann and Bergantz, 2004; Bachmann et al., 2014; Jagoutz, 2010; Lee and Bachmann, 2014; Lee and Morton, 2015; Lee et al., 2015a). However, mixing becomes more pronounced in plutonic rocks as suggested by Reubi and Blundy (2009).

3.5.4 Plagioclase compositional transects

Plagioclase phenocrysts provide a valuable record of magmatic processes and are commonly used to detect magmatic recharge events where fresh basaltic magma is injected into a crystallizing felsic magma body (Bachmann et al., 2002; Kent et al., 2010; Ruprecht and Wörner, 2007; Tepley et al., 1999). To illustrate, if a mafic magma intrudes into pre-existing felsic

magma, plagioclase in the host magma should record an increase in Ca, Fe and Mg with a corresponding decrease in K, Na, Rb and Ba if the mafic magma mixes efficiently into the felsic host. We have constructed compositional transects across plagioclase phenocrysts in the host granitoids (Figure 3.6) to evaluate whether enclave assimilation might be recorded as a recharge event. As shown in the results, our plagioclase crystals do not show any significant core to rim zoning and thus do not appear to record any mafic recharge events. This is corroborated with micro-XRF maps of plagioclase phenocrysts in thin section (Figure 3.7). The lack of zonation is perplexing given the abundance of mafic enclaves (Figures 3.2 and 3.3).

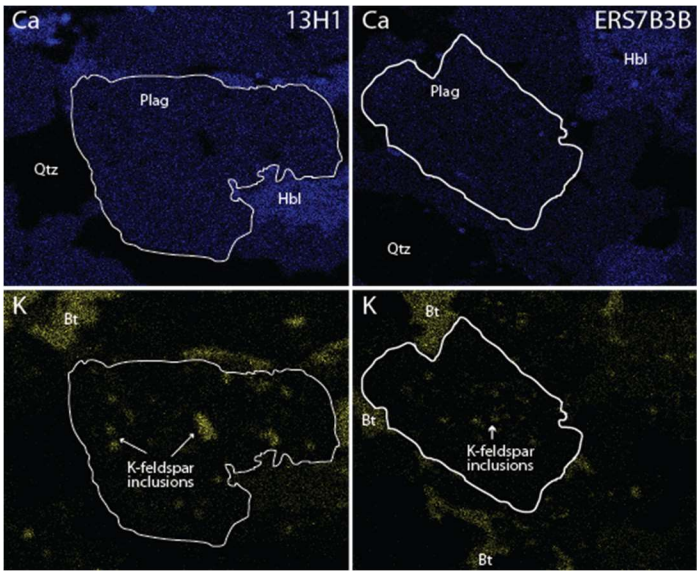

Figure 3.7. Micro-XRF compositional maps of Ca (blue) and K (yellow) in plagioclase phenocrysts (outlined in white) from two granitoid samples. Other phases present include quartz (Qtz), hornblende (Hbl), biotite (Bt) and K-feldspar.

One possible explanation for the unzoned signature is that the plagioclase crystals fully re-equilibrated by chemical diffusion, erasing any record of mafic magma injection. We can evaluate this scenario by comparing the diffusive timescales required for re-equilibration of our plagioclase crystals with the estimated lifespan of the pluton. We use constants given by Cherniak (2010) to determine the diffusivities of Ca, Na, K, Sr, and Mg in plagioclase (*D*

(700°C) = 1.9×10^{-22}, 3.3×10^{-18}, 4.3×10^{-20}, 1.1×10^{-21} and 1.7×10^{-21} m^2/s, respectively). Characteristic chemical diffusive timescales (t) scale with x^2/D, where x is the radius of the plagioclase crystal (0.6 and 1.5 mm for our smallest and largest crystals, respectively) and D is the diffusivity of the element in plagioclase. On the lengthscale of the plagioclase phenocrysts, diffusive re-equilibration timescales are >95 My for Ca, >5 ky for Na, > 0.44 My for K, >17 My for Sr and > 11 My for Mg. A maximum bound on the lifespan of the pluton can be estimated by assuming the pluton cooled conductively (allowing for convection would hasten crystallization of the pluton), wherein the cooling time scales with r^2/κ, where r is the radius of the pluton and κ is thermal diffusivity (~10^{-6} m^2/s). For an r of 1 km for the Bernasconi Hills pluton, the lifespan of the pluton must be less than ~30 ky, shorter than the chemical diffusive timescales of all elements of interest. Thus, the record of the magma's composition during plagioclase crystallization should have been preserved in the plagioclase phenocrysts and the lack of zonation indicates no mafic magma recharge despite the presence of mafic enclaves (Figures 3.2 and 3.3). This further supports our hypothesis that the enclaves formed by disaggregation of a solidified or quenched mafic magma within the host magma rather than true mixing of mafic and felsic liquids. The lack of chemical zonation also indicates that entrainment of enclaves must have occurred late in the lifespan of the Bernasconi pluton, providing little time for the effects of enclave assimilation to be "communicated" throughout the pluton before its solidification.

3.5.5 Summary model for the evolution of the Bernasconi enclave swarm

We propose the following model for the evolution of the Bernasconi enclave swarm as outlined in Figure 3.8. In the first stage, we envision a host magma with dacitic composition (~65-70 wt.% SiO_2) entraining solidified mafic magmas as xenolithic clasts during emplacement,

generating a magma body with bimodal end-member compositions. Both the mafic enclaves and felsic host form by crystal fractionation along a liquid line of descent, though the two end-members need not share the same parental magma. Following this, in the second stage, flow within the host magma stretches and attenuates the mafic enclaves, resulting in mechanical mixing as the lengthscales of the enclaves are attenuated down to the centimeter scale. Reaction between enclaves and felsic hosts also occurs simultaneously (Farner et al., 2014). Both mechanical and chemical processes modify the composition of enclaves towards more felsic compositions and the felsic host to more mafic compositions. Finally, stage 3 represents the dying stages of the magma body: as crystallization reaches completion, the magmatic system begins to lock up due to the increase in effective viscosity with increasing crystallinity. This locking up of the magma body substantially reduces the efficiency of mechanical mixing, but it is during this time when the last residual liquids, which are highly silicic, may segregate locally. These last stage silicic liquids segregate well after the mixing stage of the pluton. Segregation of these late stage silicic liquids leaves behind crystal-rich residues analogous to cumulates (Lee and Morton, 2015). However, expulsion of these late stage liquids is not efficient, leaving cumulates with significant amounts of trapped liquids. This generates silicic restites ("cumulates") with intermediate K_2O contents, as discussed by Lee and Morton (2015). Entrainment and mixing of the enclaves must occur relatively late in the lifespan of the magma body as plagioclase phenocrysts do not show any evidence of mafic-felsic interaction. We emphasize that some of these conclusions were drawn from variations in geochemistry that were too subtle to see directly in the field, thus our study provides an example of how geochemistry and textural studies should go hand-in-hand in studying the evolution of pluton bodies.

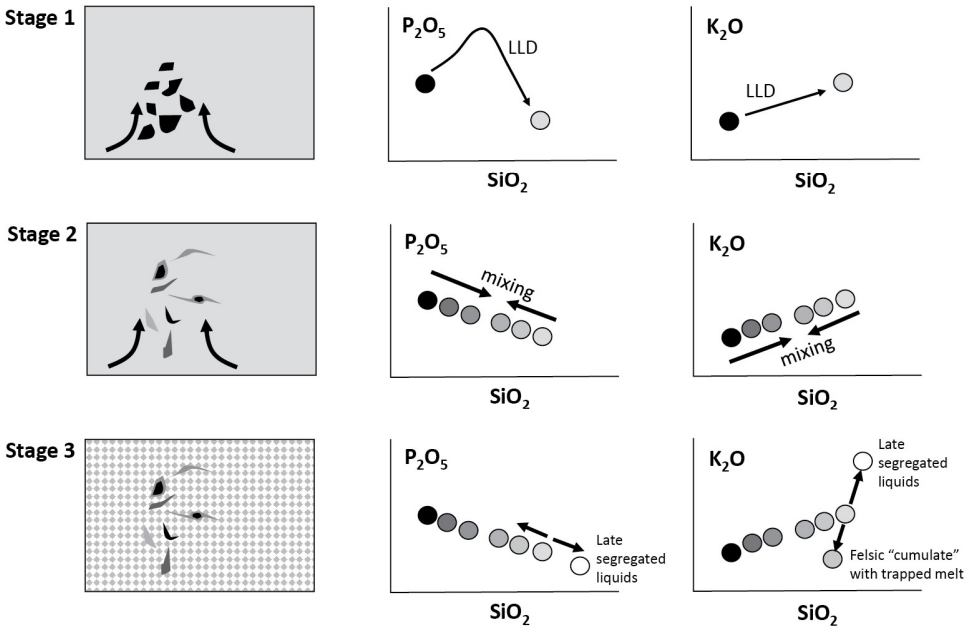

Figure 3.8. Conceptual model describing the evolution of the Bernasconi enclave swarm. In Stage 1, solidified enclaves are forcefully entrained by the felsic magma during emplacement of the pluton. Enclaves are initially solid and host magma is likely a crystal-bearing magma. Enclaves are disaggregated, generating angular clasts. Pluton consists of a bimodal composition, with mafic enclaves and felsic host. In Stage 2, enclaves become deformed by flow in the host magma. Reaction rinds form on enclaves. Attenuation of enclaves results in mechanical mixing, causing enclaves to become more silicic and portions of the host magma to become more mafic. This mixing is manifested as compositional smearing in element-element space, generating linear mixing arrays. In Stage 3, enclave deformation slows down as the magma continues to crystallize and lock up. The last residual liquids are represented by highly silicic interstitial liquids which segregate locally. These silicic components are manifested as K-rich rhyolitic compositions along with complementary K-poor "cumulates". Mafic-felsic mixing appears to occur only between enclaves and dacitic host. The most silicic components of the system never participate in mixing, suggesting they formed shortly after the magmatic system locked up by crystallization. P_2O_5 and K_2O versus SiO_2 diagrams are shown schematically to illustrate the geochemical effects of these different processes. Darkness of circle symbols in the geochemical diagrams and the mixing cartoons correspond qualitatively to silica content (dark = mafic and light = silicic).

Whether the Bernasconi Hills case study applies to arc magmas on a global scale is uncertain. Our observations suggest that mixing can be locally important, as in the case of Bernasconi Hills. On a larger scale, we showed that volcanic rocks show minimal evidence for mixing, that is, the entire spectrum of magmas, including intermediate lavas, can be explained by crystal fractionation. In contrast, plutonic rocks seem to have much more variable

characteristics, with some following simple crystal fractionation paths and others showing evidence of mafic-felsic mixing. The reason for these differences are not clear to us, but it is possible that extrusive lavas do not spend enough time in magma chambers to efficiently mix. Plutonic rocks may reside in deep crustal magma chambers for longer periods of time, allowing for more extensive mixing. Mafic recharge, nonetheless, must occur in volcanic systems, as evidenced by reverse zonation in plagioclase phenocrysts in many arc lavas (Kent et al., 2010; Tepley et al., 1999). However, such recharge may not actually cause extensive homogenization of the magma body as these recharge events appear to trigger eruptions, at least in shallow magma chambers. Entrainment of mafic lithologies into felsic magmas may also be a late stage phenomenon, limiting mixing to only the deepest and longest-lived magma bodies.

3.6 Conclusions

We have presented a case study of the Bernasconi Hills pluton in order to examine the role of mafic-felsic mixing in the formation of intermediate magmas. We observe extensive mingling between mafic enclaves and host granitoid in the field and our observations indicate that enclaves were produced by disaggregation of larger mafic bodies shortly before complete solidification of the host pluton. Major element oxide data and P_2O_5-Zr systematics of enclaves and host magmas indicate that geochemical homogenization has occurred, but is limited to the centimeter to meter lengthscale, suggesting limited mixing late in the magmatic life of the pluton. Unzoned plagioclase phenocrysts in the host granitoid suggest that the enclaves were either solid or solidified quickly when they came in contact with the felsic host magma, further supporting the notion that mixing operated only over short lengthscales and short timescales. Comparison of our results to volcanic and plutonic rocks suggests that mixing is not the most

important process in generating arc volcanic rocks but may be important in the generation of some plutonic rocks.

Chapter 4

Effects of crustal thickness on magmatic differentiation in subduction zone volcanism: a global study[3]

[3]This chapter is under review for Earth and Planetary Science Letters as Farner, M.J., Lee, C.-T.A. "Effects of crustal thickness on magmatic differentiation in subduction zone volcanism: a global study".

The majority of arc magmas are highly evolved due to differentiation within the lithosphere or crust. Some studies have suggested a relationship between crustal thickness and magmatic differentiation, but the exact nature of this relationship is unclear. Here, we examine the interplay of crustal thickness and magmatic differentiation using a global geochemical dataset compiled from active volcanic arcs and elevation as a proxy for crustal thickness. With increasing crustal thickness, average arc magma compositions become more silicic (andesitic) and enriched in incompatible elements, indicating that on average, arc magmas in thick crust are more evolved, which can be easily explained by the longer transit and cooling times of magmas traversing thick arc lithosphere and crust. As crustal thickness increases, arc magmas show higher degrees of iron depletion at a given MgO content, indicating that arc magmas saturate earlier in magnetite when traversing thick crust. This suggests that differentiation within thick crust occurs under more oxidizing conditions and that the origin of oxidation is due to intracrustal processes (contamination or recharge) or the role of thick crust in modulating melting degree in the mantle wedge. We also show that although arc magmas are on average more silicic in thick crust, the most silicic magmas (>70 wt. % SiO_2) are paradoxically found in thin crust settings, where average compositions are low in silica (basaltic). We suggest that extreme residual magmas, such as those exceeding 70 wt. % SiO_2, are preferentially extracted from shallow crustal magma bodies than from deep-seated magma bodies, the latter more commonly found in regions of thick crust. We suggest that this may be because the convective lifespan of crustal magma bodies is limited by conductive cooling through the overlying crustal lid and that late stage magma bodies in thick crust cool more slowly than in thin crust. When the crust is thin, cooling is rapid, preventing residual magmas from being extracted; in the rare case that residual magmas can be extracted, they represent the very last melt fractions, which are highly silicic. When the crust is thick, cooling is slow, so intermediate melt fractions can readily segregate and erupt to the surface, where they cool and crystallize before highly silicic residual melts can be generated.

4.1 Introduction

The continental crust is enriched in silica and depleted in iron relative to a parental basaltic magma and, at least since the Proterozoic, much of it originated in subduction zone settings through arc magmatism. Melting of the mantle wedge above subducting oceanic lithosphere generates basalts, which then rise into the upper plate lithosphere where they undergo cooling and crystallization to produce

evolved residual melts that go on to make the crust. Both the processes of mantle melting and intracrustal differentiation influence the compositions of arc magmas (Arndt and Goldstein, 1989; Herzberg and Rudnick, 2012; Jagoutz, 2010; Jagoutz and Schmidt, 2012; Kelemen, 1995; Lee, 2014; Lee and Bachmann, 2014; Lee et al., 2006; Plank, 2005; Plank and Langmuir, 1988; Rudnick, 1995; Turner and Langmuir, 2015a, b).

A number of studies have suggested that crustal thickness plays a role in controlling the composition of arc magmas. Plank and Langmuir (1988) and Turner and Langmuir (2015a,b) have shown that crustal thickness controls the composition of parental arc basalts by modulating the degree of mantle melting. Superimposed on mantle source effects are the effects of intracrustal differentiation, where fractional crystallization and other processes generate more evolved melts (Hildreth and Moorbath, 1988; Jagoutz and Schmidt, 2012; Lee and Bachmann, 2014). Progressive intracrustal differentiation eventually masks most of the original mantle signatures, such that by the time magmas evolve to compositions typical of average continental crust, intracrustal differentiation overwhelms much of the source signal. For example, the andesitic (silicic) nature of continental crust is a result of intracrustal differentiation, and not so much due to mantle source effects, which generate basalts. Crustal thickness has also been invoked to explain the composition of more evolved arc magmas, with suggestions that thick crust favors more silicic compositions (Chapman et al., 2015; Dhuime et al., 2015; Lee et al., 2015b; Mantle and Collins, 2008).

In this paper, we explore the effects of crustal thickness on intracrustal differentiation by examining how the average composition of arc magmas varies globally with arc elevation, which we use as a proxy for crustal thickness. We find that arc magmas in thick crust have higher silica content, are more depleted in iron and more enriched in incompatible elements than magmas that traverse thin arc crust. Our observations indicate that arc magmas traversing thick crust have experienced more crystal fractionation. The greater extent of iron depletion in arc crust in thick magmatic arcs reflects earlier onset of magnetite saturation, which suggests that arc magmas traversing thick crust, such as in continental arcs, are more oxidized than arc magmas traversing thin crust, such as in island arcs. Importantly, these

signatures that typify arc magmas in thick crust are the same signatures that characterize average continental crust.

4.2 Global arc database

We examined only Pleistocene to Holocene age volcanic rocks to insure that rock compositions reflect recent volcanism and are comparable to estimates of modern-day crustal thickness. Whole-rock compositions of lavas (n = 52259) were compiled from the GEOROC database (http://georoc.mpch-mainz.gwdg.de/georoc/) for all presently active volcanic arcs using precompiled data for individual arc segments (Figure 4.1). Compiled data were filtered to include subaerial arc front volcanic rocks (n = 36,947) with geolocation data, a designated lithologic name (e.g. basalt, rhyolite), and major element oxide sums within the range 98-101.5 wt % to exclude altered rocks. Our compilation differs from other recent arc lava compilations (Plank and Langmuir, 1988; Turner and Langmuir, 2015a, b), which excluded low (< 4 wt %) MgO samples for the purpose of investigating the effects of the mantle source on the compositions of primitive magmas. The objective of those studies, in particular, was to quantify the composition of primitive arc magmas by extrapolating crustal differentiation trends to a fixed MgO content (6 wt. % MgO) rather than characterizing average compositions of arc magmas "as is". In this paper, we are interested in the extent of crustal differentiation, so all magma compositions were retained to obtain an average arc magma composition. We note that the majority of arc magmas have MgO contents <6 wt. %, owing to crustal differentiation.

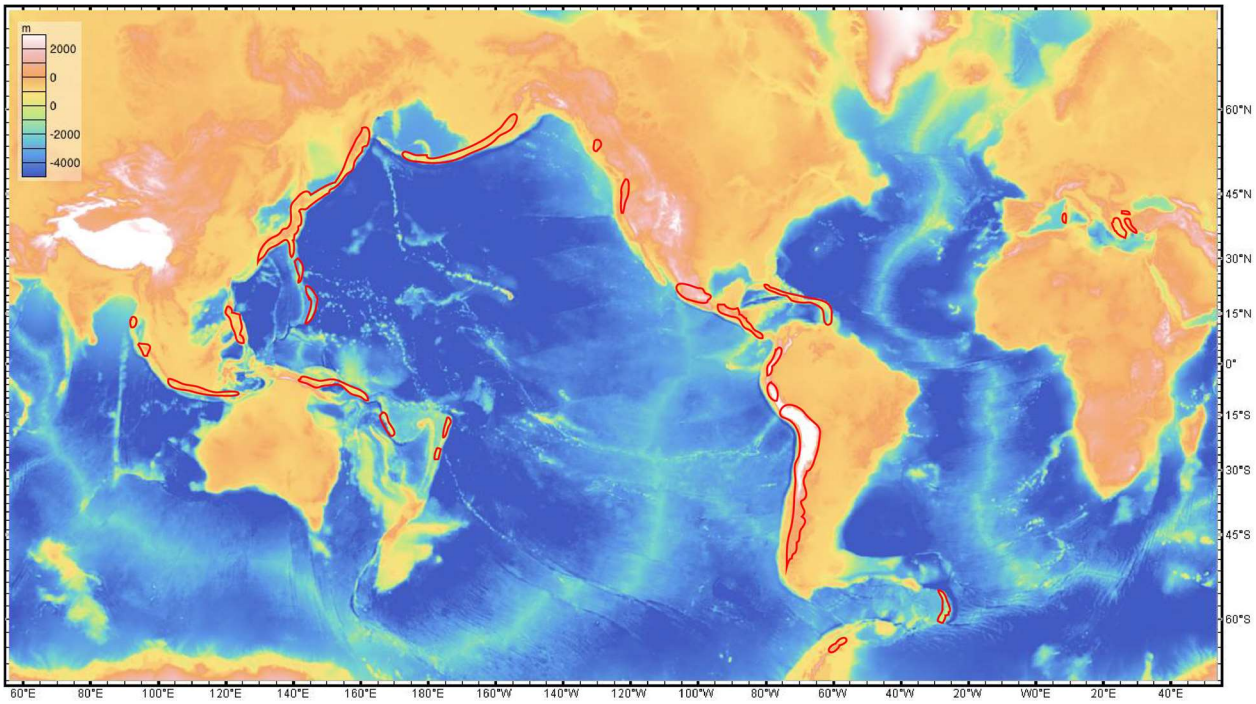

Figure 4.1. Elevation (m) map of the Earth with locations of compiled arc lavas outlined in red.

A number of studies have compared magma compositions with crustal thickness as constrained seismically by the depth of the Moho (Chapman et al., 2015; Hildreth and Moorbath, 1988; Mantle and Collins, 2008; Plank and Langmuir, 1988; Turner and Langmuir, 2015a, b), but because seismic studies are not available everywhere, the geographic coverage of such comparisons is not comprehensive. To cover all active arcs, we assume that over long enough lengthscales, the Earth is isostatically compensated, particularly beneath active arcs where the crust is hot and weak. Lee et al. (2015b) showed that elevations of mountains correlate to first order with Moho depth (Laske et al., 2013), indicating that high elevations are isostatically compensated by crustal thickness, with mantle contributions of second order. We use the empirical correlation of elevation versus crustal thickness in Lee et al. (2015b) to convert elevation to crustal thickness and estimate lithostatic pressure at the base of the crust (assuming an average crustal density of 2870 kg/m^3).

Elevations of geo-located samples were obtained using the ESRI ArcGIS software package. Elevations for individual samples were extracted from the National Oceanographic and Atmospheric Administration ETOPO2 digital elevation model (https://www.ngdc.noaa.gov/mgg/global/etopo2) modified in ArcGIS to have a 10 km × 10 km (~333 arc-second) horizontal grid spacing. We chose a 10 km ×10 km grid size in order to filter out non-isostatic topography, which occurs on a smaller lengthscale.

One complicating issue in data compilations is that such datasets could have sampling bias. For example, some scientifically popular volcanoes are clearly oversampled. To minimize sampling bias, we averaged compositional data over discrete volume units with horizontal dimensions of 10 km × 10 km and a vertical dimension of 100 m (L×W×h = 10 km×10 km×100m). With this approach, compositional data are spatially equal, that is, the dataset is not weighted towards any particular location.

4.3 Results: elevation-composition trends

More than 83% of arc magmas in our database have MgO contents less than 6 wt. % (Figure 4.2), significantly lower than primary arc basalts (>10 wt. % MgO). Thus, the great majority of arc magmas have undergone significant crystal fractionation. Systematic variations in mean and median compositions with elevation are evident when data are grouped in 100 m elevation intervals and averaged as described above (Appendices D and F). Basalt dominates at low elevations (Figure 4.2A-4.2C) and andesite dominates at high elevations (Figure 4.2D-4.2F) as can be seen by the increase of mean SiO_2 with increasing elevation (Figure 4.3A) as well as changes in the distribution of SiO_2 with elevation. Accompanying the increase in SiO_2 with increasing elevation are increases in K_2O (Figure 4.3F) and Rb/Sr (Figure 4E), reflecting progressive enrichment in incompatible elements with elevation and silica (Figures 4.3 and 4.4). In contrast, compatible elements like FeO^* (total Fe cast as Fe^{2+}), MgO, TiO_2, and CaO, along with geochemical indices like Mg# (molar Mg/(Mg+Fe)) decrease with increasing elevation (Figures 4.3B-4.3D and 4.4A-4.4D). We also show that elemental ratios, such as La/Yb and Gd/Yb, which are commonly attributed to garnet fractionation, increase with elevation (Figures 4.5A-4.5B).

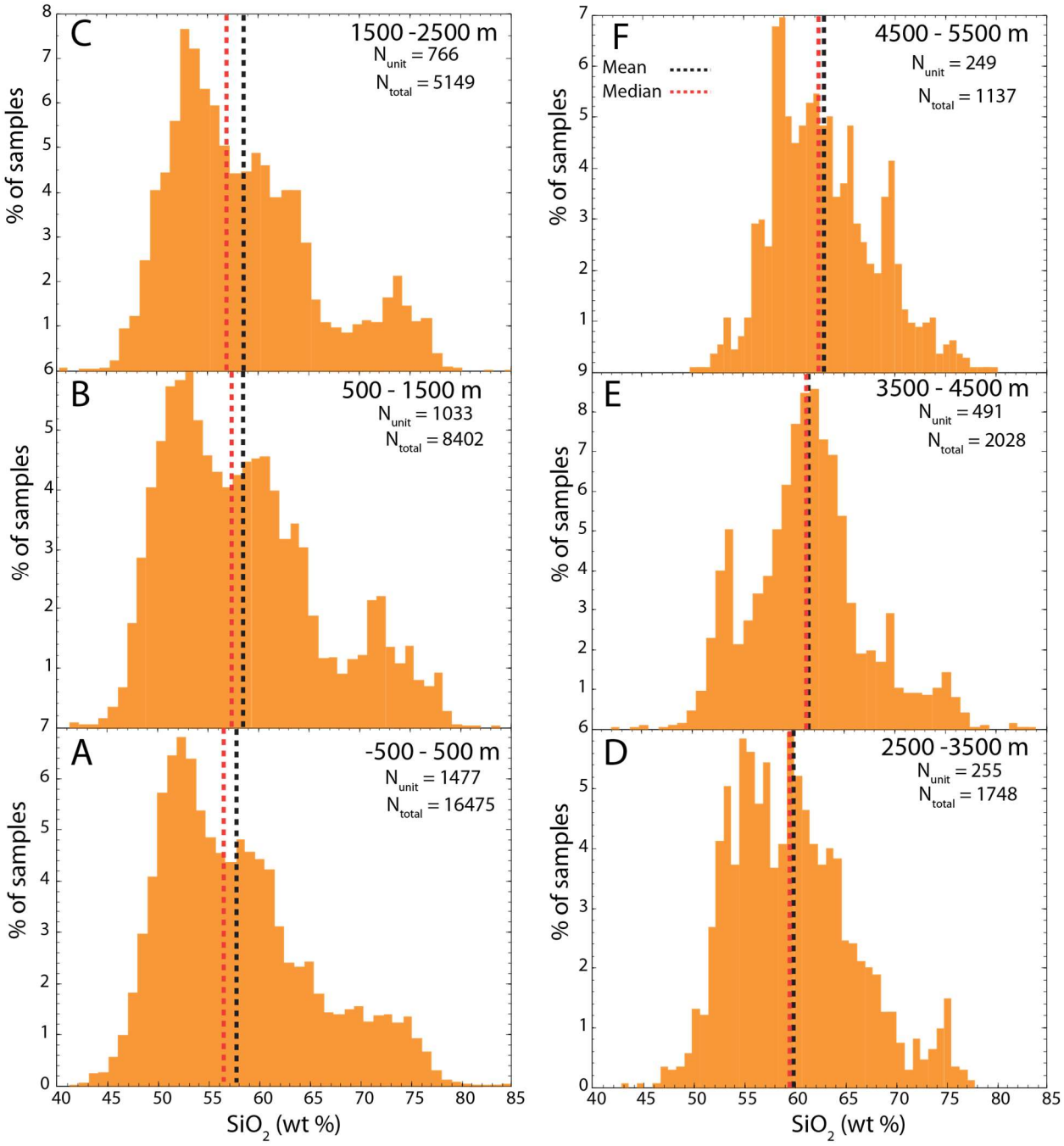

Figure 4.2. (A-F) Normalized histograms of SiO_2 (wt. % on a volatile free basis) of compiled lavas within selected 1000 m elevation bins. Elevations are averaged over a 10 km × 10 km square horizontal area. Geochemical data are spatially averaged over unit volumes of 100 m thickness and 10 km × 10 km horizontal area (L×W×h = 10 km×10 km×100m) to suppress biases associated with oversampling of individual volcanoes. Vertical lines represent mean (black) and median (red) of unit volume averages. Total number of samples within each elevation bin is given by N_{total}. Total number of unit volumes in each 1000 m elevation bin is given by N_{unit}.

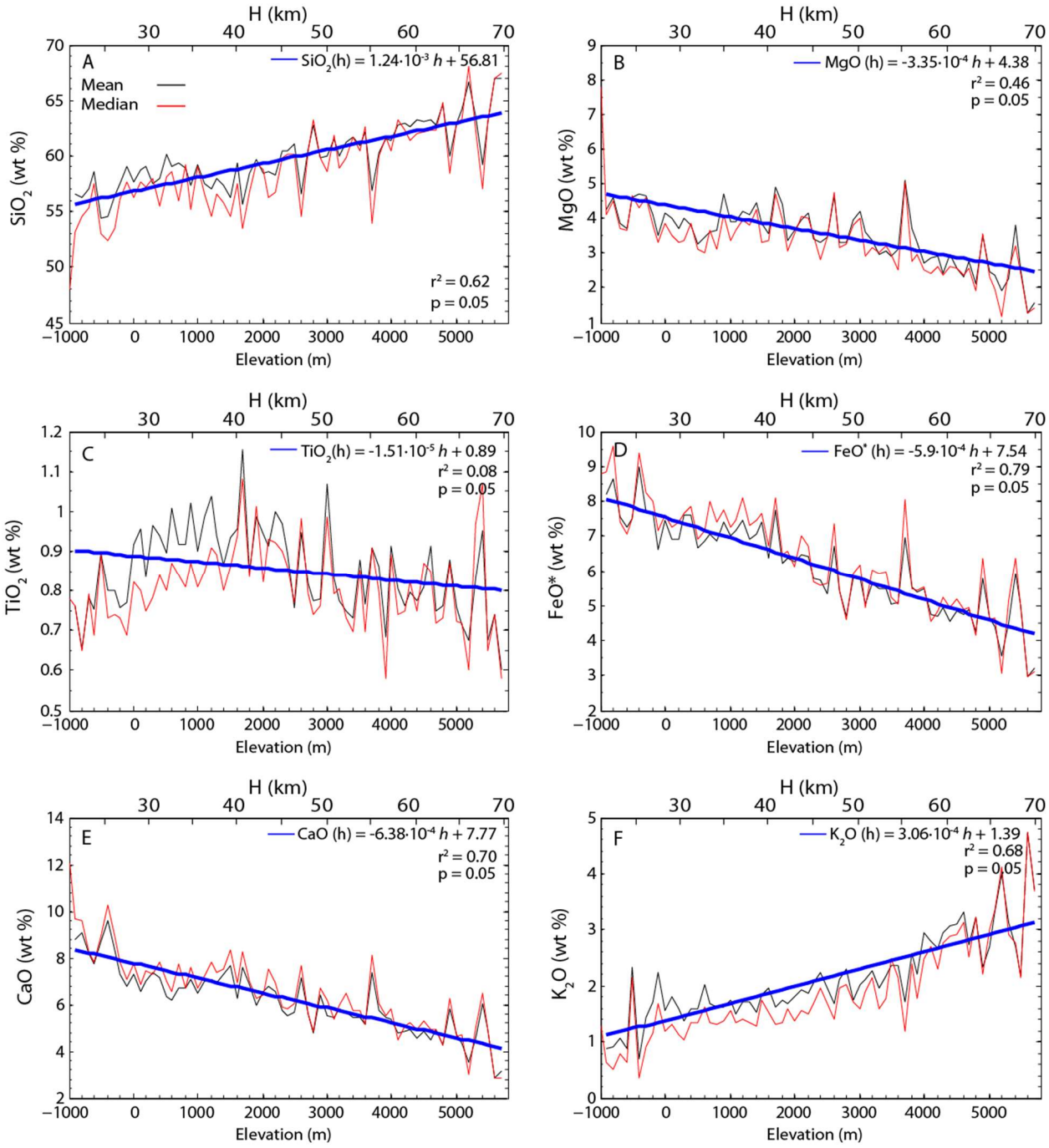

Figure 4.3. (A-F) Mean and median major element contents of arc lavas shown as functions of elevation (averaged over 10 km ×10 km × 100 m unit volumes) with estimated crustal thickness. As elevation increases, silica (A) and potassium (F) increase while compatible major element contents (B-E) decrease. Equations for compositional-elevation regressions are given in supplementary materials along with calculated r^2 and p-values for the regression.

Recognizing that elevation correlates with crustal thickness (Lee et al., 2015b), the above observations confirm previously noted compositional relationships with crustal thickness (Chapman et al., 2015; Chiardia, 2015; Dhuime et al., 2015; Hildreth and Moorbath, 1988; Mantle and Collins, 2008; Plank and Langmuir, 1988; Turner and Langmuir, 2015a, b), but our use of elevation as an indirect proxy for crustal thickness allows for more comprehensive coverage of all active arcs: from island arcs with thin crust and low elevations to continental arcs with thick crust and high elevations. Two new observations, however, are revealed as a consequence of this comprehensive sampling. First, we observe systematic variations in the calc-alkaline signature of magmatic differentiation with elevation. Following Zimmer et al. (2010), the calc-alkaline signature of a magmatic differentiation series is defined by the magnitude of FeO^* depletion relative to the primary magma's FeO^* content. As can be seen from the global data systematics in Figure 4.4B, the FeO^* content of primary arc magmas does not vary significantly. For these reasons, we measure the degree of iron depletion in evolved magmas using FeO^* at 5 wt. % MgO, the latter a widely used indicator of the extent of differentiation. We calculate FeO^* at 5 wt. % MgO (FeO^*_{5MgO}) by averaging all samples between 4 and 6 wt. % MgO. In Figure 4.6A, it can be seen that FeO^*_{5MgO} decreases with increasing elevation, indicating that magmas, which traverse thicker crust, such as in continental arcs, differentiate along calc-alkaline paths (greater Fe depletion) whereas those that traverse thinner crust, such as in island arcs, are more tholeiitic (less Fe depletion). This can also be observed in Figure 4.6B where arc lavas, on average, become more iron-depleted and alkali-enriched with increasing elevation. These observations also suggest that increasing SiO_2 content of the magma correlates with an increasing calc-alkaline signature of magma during differentiation.

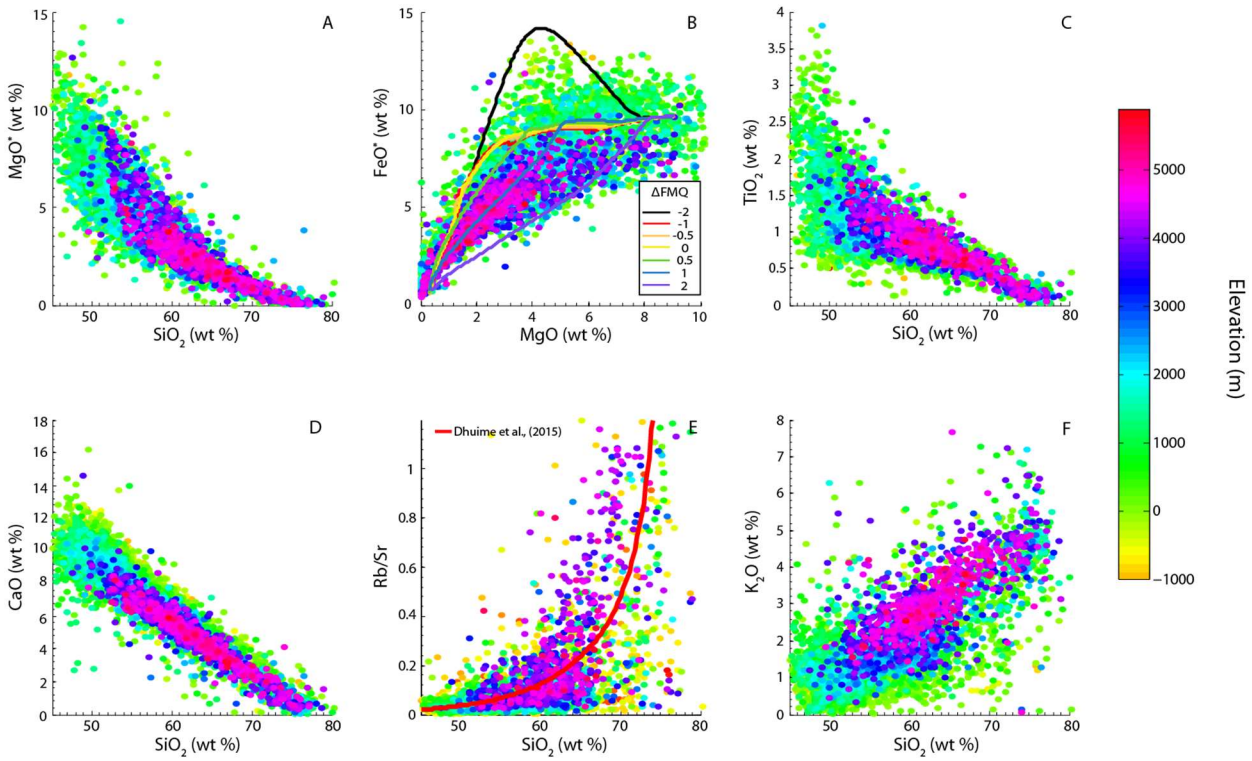

Figure 4.4. (A-F) Variation diagrams of selected elements and elemental ratios versus SiO_2 colored by elevation. Elemental concentrations are shown for all10 km×10 km×100 m unit volumes for a given elevation interval. As elevation and SiO_2 increase, compatible major element contents decrease and lavas tend toward more evolved, iron-depleted compositions. Panel B shows closed system liquid line of descent paths from a primitive hydrous (4 wt. %) basalt for different oxygen fugacities relative to the fayalite-magnetite-quartz buffer in log_{10} units (see text for details). In panel E, Rb/Sr versus SiO_2 correlation from Dhuime et al. (2015) is shown for comparison. Note that data are layered on the plot so that the highest elevation samples are on top.

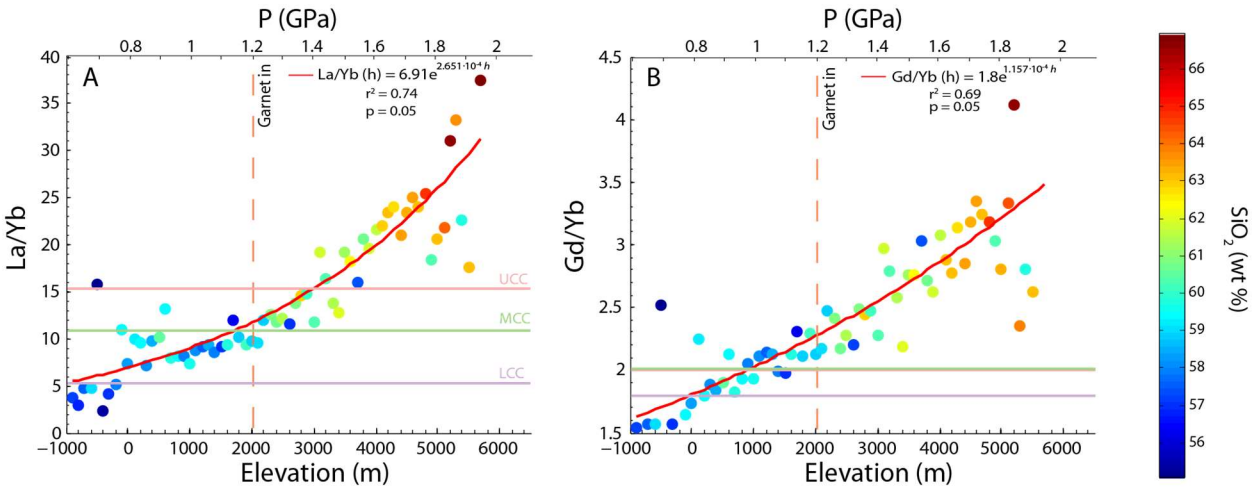

Figure 4.5. (A-B) Global mean La/Yb and Gd/Yb, colored by average SiO_2 content, plotted against elevation and corresponding effective lithostatic pressure at the Moho as determined from inferred crustal thickness. Garnet-in pressure is from Alonso-Perez et al., 2008. UCC = upper continental crust, MCC = middle continental crust, LCC = lower continental crust from Rudnick and Gao (2003). All numbers are based on elemental concentrations averaged over 10 km × 10 km × 100 m unit volumes.

The second observation is that although there is systematic variation in mean and median compositions with elevation, the difference between the mean and median decreases with increasing elevation (Figure 4.3A-4.3F; Appendices D and F). The systematic variation in the difference between mean and median values is reflected in the symmetric frequency distributions at high elevations and skewed or even bimodal distributions at low elevations (Figure 4.2A-4.2D), the latter due to a high silica tail that extends to rhyolitic compositions (Figure 4.2E-4.2F). These changes in distribution apply to elevation-composition trends regardless of which digital elevation model is used (Figure 4.2), once again confirming that the trends reported here are not artifacts of the elevation model or statistical binning. Curiously, although lavas average more silicic at high elevations, the most silicic (rhyolitic) end-members are found primarily at low elevations, where basalts dominate (Figure 4.2A), and are poorly represented at high elevations, where andesites dominate (Figure 2F). It does not seem likely that this over-representation of highly silicic magmas in regions of thin crust or its under-representation in thick crust is a result of vertical sampling bias because a similar observation was reported by Lee and Morton (2015)

with respect to plutonic rocks from the Cretaceous Peninsular Ranges Batholith in southern California, USA. Using heavy rare earth element systematics as a constraint on crustal thickness, they showed that plutons with andesitic compositions dominate in thick crust, but there is a paucity of highly silicic magmas (> 70 wt. % SiO_2), such as granites. In thin crust, plutons average slightly less silicic than in thick crust, but the most silicic magmas in the batholith are found in thin crust. Given that both volcanic and plutonic rocks yield similar patterns in silica content distribution with crustal thickness, the observed over-representation of silicic magmas in thin crust is likely the result of magmatic processes not sampling biases.

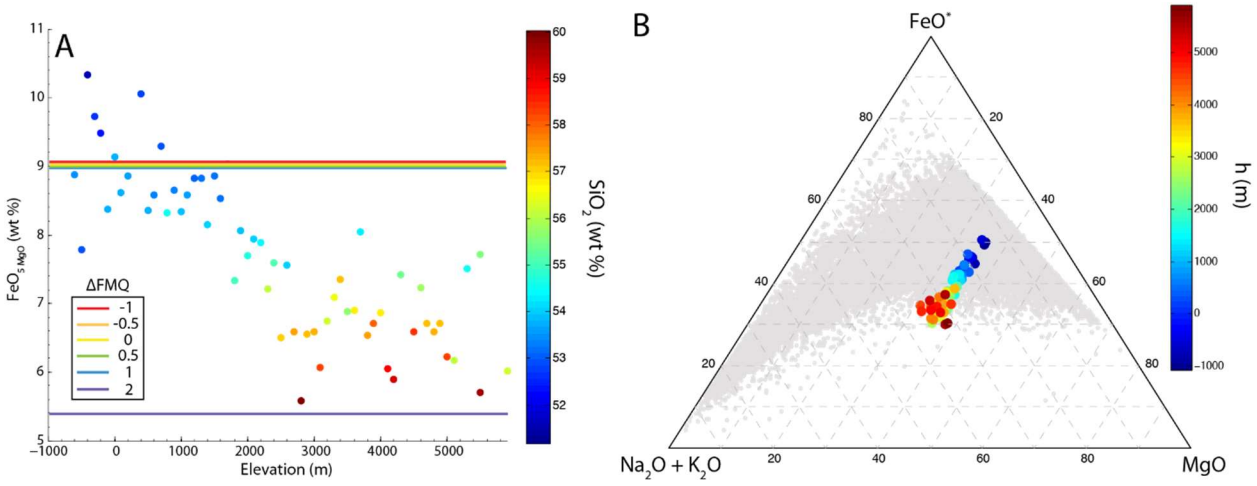

Figure 4.6. (A) Global FeO^*_{5MgO} (* = total Fe as FeO; 5MgO indicates FeO* is the average of all samples between 4-6 wt. % MgO) as a function of elevation, color coded for SiO_2. Oxygen fugacity contours are taken from liquid lines of descent using Rhyolite-MELTS modeling shown in Figure 4b at MgO = 5 wt. %. (B) K_2O+Na_2O-FeO^*-MgO ternary diagram illustrating increasing calc-alkalinity with elevation (colors reflect elevation). Gray symbols represent all individual samples in the dataset. Larger symbols represent compositional data averaged over 10 km × 10 km × 100 m unit volumes.

4.4 Discussion

4.4.1 Magmatic differentiation during transport from the mantle to crustal magma reservoirs

As noted above, elevation can be translated into equivalent crustal thickness (Lee et al., 2015b), so the above compositional variations indicate variations with crustal thickness. Qualitatively, the more

evolved nature of magmas with increasing crustal thickness is intuitive and unsurprising, but a more quantitative context is warranted. We begin by examining the variation of effective residual melt fraction *F* with crustal thickness. We can estimate the effective melt fraction *F* represented by an evolved magma relative to a parental basalt as the inverse of the enrichment of a highly incompatible element in the evolved magma (*C*) relative to that in the parental magma (C_o), that is, $F = C_o/C$ (Appendix F). Following Lee and Morton (2015), the estimated melt fraction is independent of whether the melt represents a residual melt formed by down-temperature crystal fractionation of a basaltic magma or a derivative melt formed by up-temperature partial re-melting of a pre-existing rock, even though the physical meanings of such melts are different. The progressive increase of K_2O with increasing SiO_2 (Figures 4.3F and 4.4F) indicates that potassium behaves perfectly incompatibly throughout magmatic differentiation, consistent with the well-known observation that K-bearing phases like biotite and alkali feldspar saturate very late in the crystallization sequence of most magmas, making it an ideal element to estimate effective melt fractions (Glazner and Johnson, 2013; Whitney, 1988).

Using an initial K_2O content (C_o) of 0.43 wt. %, determined by taking the average of the most primitive arc basalts in the dataset (MgO > 12 wt. %), we can estimate how effective residual melt fraction varies as a function of crustal thickness (Figure 4.7). We recognize that calculated residual *F* values depend on natural variations in C_o, which is controlled by the extent of melting or metasomatism in the mantle (Turner and Langmuir, 2015a, b), but variations in source conditions are within a factor of 2 or 3, whereas the enrichment in highly evolved arc magmas can exceed a factor of 10, so our approach is insensitive to these uncertainties for highly evolved magmas, where extreme enrichments have been imparted by extensive crystal fractionation. As shown in Figure 4.7, lavas at low elevations are represented by evolved basalts and basaltic andesites corresponding to effective residual melt fractions of ~30%, and at high elevations, lavas are represented by dacites corresponding to residual melt fractions of less than 20%. By comparison, rhyolitic magmas represent residual melt fractions less than 10%. If most of the observed magmatic series forms by crystal fractionation, as is widely thought, these trends imply that when magmas traverse thicker crust, they undergo more extensive crystal fractionation, generating

more evolved residual magmas. While partial melting and assimilation of pre-existing crust certainly do influence magma compositions, the coherency of fractionation trends observed globally in volcanic suites indicates that crustal assimilation is likely second order compared to crystal fractionation (Jagoutz, 2010). The dominance of crystal fractionation is corroborated by nonlinear Zr and P versus SiO_2 systematics (Lee and Bachmann, 2014).

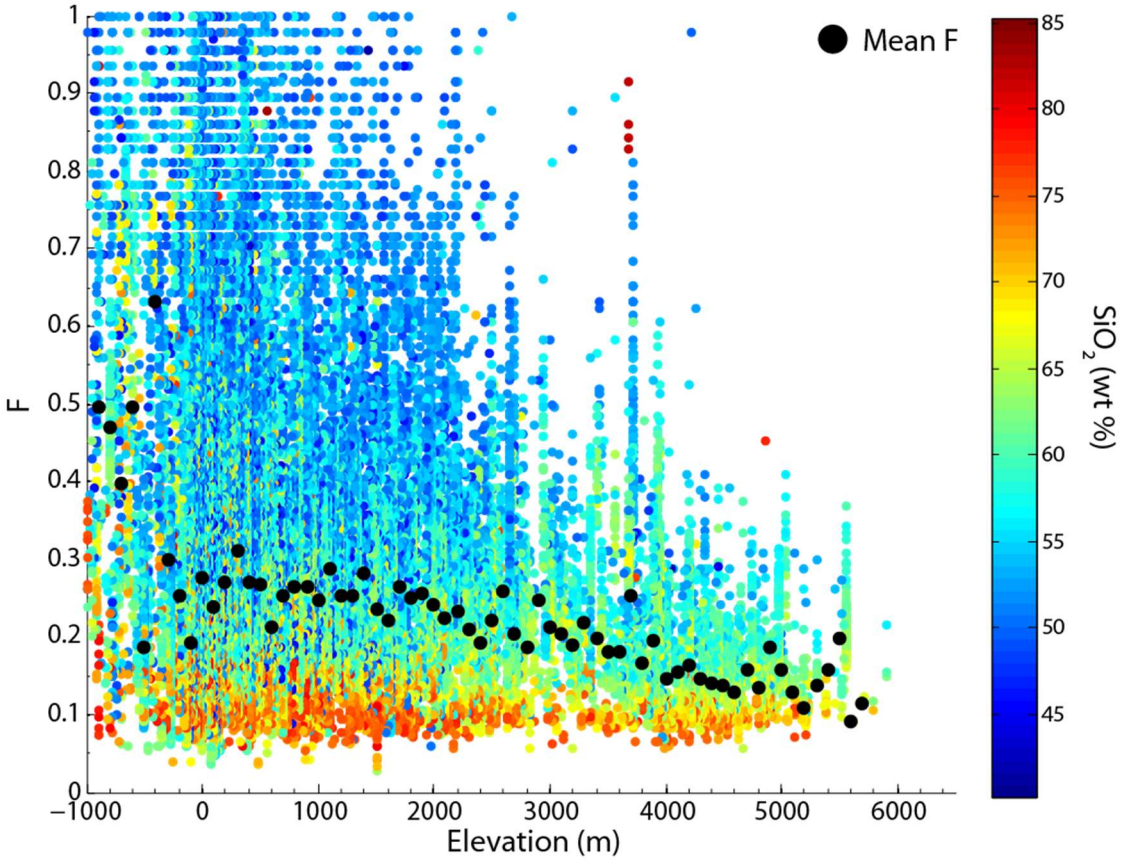

Figure 4.7. Calculated effective residual melt fraction (*F*) as a function of elevation for all compiled data (see text for explanations). Samples are colored by SiO_2 content. Mean effective residual melt fractions for each 100 m elevation interval are shown as black circles. Residual melt fractions are calculated assuming a primitive basalt composition with 0.43 wt. % K_2O, based upon our dataset.

The decrease in effective residual melt fraction *F* with crustal thickness may not be surprising because qualitatively it would seem that the transit time of magmas migrating through thick crust might be longer than that through thin crust, allowing more time for cooling and crystal fractionation. The

longer the transit time, the greater the loss of heat from the magma to the cold country rock, resulting in greater amounts of crystallization. The actual transport of magmas through the crust is undoubtedly complicated, but this concept can be illustrated with a simple model of the transit time of magma traversing the crust.

We consider melt rising through the crust in a dike cooling by conductive heat loss to the surrounding wallrock (Figure 4.8A). In our simple case, we only consider the down-temperature evolution the melt with crystallization occurring on the walls of the dike and the residual melt remaining in the center of the dike. Assuming that mantle-derived magmas rise through the lithospheric mantle and crust via dikes, eventually coalescing into a crustal magma body, the transit time from the mantle to the crustal magma body is approximately L/u, where L is the distance between the Moho and the magma chamber (length of the dike) and u is the average velocity of the magma rising through the dike. Velocity is approximated by laminar channel flow driven by the intrinsic buoyancy of the magma relative to the wallrock, that is, $u \sim \Delta\rho g r^2/3\eta$, where $\Delta\rho$ is the density difference between the wallrock and melt ($\Delta\rho \sim$ 200 kg/m^3), r is the radius of the dike and η is dynamic viscosity (η =100 Pas). Crystallization extent is tracked by modeling the average temperature T_m of the magma in the ascending dike using equations given by Carslaw and Jaeger (1959) for the conductive cooling of a slab, with a constant boundary temperature representing the wallrock (T_w) of 500 °C

$$T_m(\tau) = T_w + \frac{8T_0}{\pi^2}\sum_{n=0}\frac{1}{(2n+1)^2}e^{-\kappa(2n+1)^2\pi^2\tau/4r^2} \quad (4.1)$$

where T_o is the initial temperature difference between the melt and wallrock temperature, κ is thermal diffusivity (10^{-6} m^2/s), r is radius of the dike and τ is the characteristic transit time ($\tau = z/u$). This constant temperature boundary condition is obviously a simplification, but we treat it as an average effective temperature.

We assume an initial melt temperature equal to the liquidus temperature of a primitive basalt from our dataset (as wt% on a volatile-free basis, 50.74 SiO_2, 0.71 TiO_2, 16.70 Al_2O_3, 9.66 FeO^*, 9.11

MgO, 10.85 CaO, 1.83 Na_2O, and 0.40 K_2O) as calculated by the Rhyolite-MELTS thermodynamic program at 0.4 GPa (Ghiorso and Gualda, 2015; Gualda et al., 2012). Using the cooling model above, we track changes in melt fraction and SiO_2 content of the cooling melt as parameterized functions of temperature based upon Rhyolite-MELTS output for closed-system crystallization such that

$$F(T) = \sum_{i=0}^{7} a_i \overline{T^i} \qquad (4.2)$$

$$SiO_2(T) = \sum_{i=0}^{6} b_i \overline{T^i} \quad (4.3)$$

$$\bar{T} = \frac{T_m - T_s}{T_l - T_s} \quad (4.4)$$

where temperature $\bar{T}$ is normalized to the difference between the liquidus T_l and solidus temperatures T_s and a_i and b_i are empirical constants based upon Rhyolite-MELTS calculations for isobaric cooling of the primitive basalt composition at 0.4 GPa pressure, and oxygen fugacity fixed to the fayalite-magnetite-quartz buffer and 4 wt % initial H_2O (Plank et al., 2013). The compositional parameters for Eqs. 4.2-4.4 can be found in Appendix E. Pressure effects on these parameters play a smaller role and are not considered here.

The extent of differentiation, which scales with extent of dike cooling, depends on the effective Peclet number of the system, which is a measure of the thermal diffusion timescale relative to the dike transport timescale. Taking the thermal diffusion timescale as $t_{th} \sim r^2/\kappa$, where κ is thermal diffusivity (10^{-6} m^2/s) and the dike transport timescale is L/u, where L is the distance from the mantle to the crustal magma chamber, the expression for the Peclet number is

$$\mathrm{Pe} = \frac{\Delta\rho g r^4}{L\eta\kappa} \qquad (4.5)$$

At high Pe, corresponding to rapid transport, long diffusive lengthscales (large r or low η) or short transit distance (L), magmas entering the crustal magma body will have only minimally cooled and differentiated and will therefore be basaltic. At low Pe numbers, corresponding to slow transport, short diffusive

lengthscales, or long transit distances, magmas will have cooled and crystallized more extensively and therefore be more evolved. If transit distance *L* scales roughly with crustal thickness, we predict that magmas should become more evolved with increasing crustal thickness, all other variables being the same (Figure 4.8B).

We recognize that the physics of this transit time model are simplified. For example, we have ignored fracture strength of the wallrock and non-buoyancy-driven overpressures that may drive magma ascent. Our approach, however, is still sufficient to show that observed variations in average silica content in island and continental arcs can, to first order, be explained by different crustal transit times. More sophisticated models are warranted, but the overall relationship between crustal thickness and extent of differentiation will not change.

4.4.2 Lifespan of crustal magma bodies and the composition of late segregated melts

While the average extent of fractionation can be readily explained by the transit time of magma ascent, the same model cannot explain the apparent paradox in which the most silicic magmas occur in thin crust, where lavas average basaltic (Figure 4.2A). One possible explanation is that silicic magmas do not erupt to the surface in thick crust because such magmas cool, crystallize and stall during the long transit times of traversing thick crust. If this is the case, the lack of high silica rocks in regions of thick crust would be due to a bias introduced from sampling only shallowly emplaced rocks, but recent studies have shown that plutonic, which represent snapshots of magmas at depth, and volcanic rocks are similar in bulk composition (Keller et al., 2015). Furthermore, high silica plutons are uncommon in thick crust (Lee and Morton, 2015). Thus, the lack of high silica magmas in arcs with thick crust is due to geological processes and not an artifact of vertical sampling bias. This suggests that in regions of thick crust, highly silicic melts in general are not segregated into discrete magma bodies at the surface or at depth (leucogranites are common in such environments, but they are typically of small volume), but in regions

of thin crust, small amounts of silicic magmas are able to segregate while intermediate magmas are under-represented (giving a bimodal distribution of silica).

In the previous section, we examined the initial transit of melt through the crust, which we term stage 1. In this section, we consider the subsequent stage in which the accumulated intracrustal magma body cools (stage 2). In a cooling magma body, the residual melt fraction decreases and becomes more silicic with progressive cooling and crystallization. The composition of segregated melts is determined by the relative timescales of melt segregation and the thermal lifespan of the magma body, the latter defined as the time the magma body spends above the solidus. If the magma body's thermal lifespan τ_{life} is greater than the time for crystal-melt segregation τ_{seg}, melt segregation occurs before complete crystallization of the magma body, so melts of intermediate melt fraction and composition segregate. If these intermediate melt compositions erupt to the surface and quench, then highly evolved melts, like rhyolites, never have a chance to form. At the other extreme, if $\tau_{life} << \tau_{seg}$, then the magma body freezes in place before any residual melts can be expelled, so the bulk composition of this magma body will remain primitive. If $\tau_{life} \sim \tau_{seg}$, melt segregation might occur, but only late in the magma body's life, resulting in the expulsion of only low melt fraction, silicic magmas. In such a scenario, small volume silicic magma bodies, representing segregated residual liquids, should occur in the same area as more primitive, basaltic magmas, which remain compositionally similar to the parental magma.

To better quantify the above concepts, we modeled the lifespan of a crustal magma body by assuming a convecting magma body in which heat loss from the magma body is controlled by the thickness of the overlying crust, which serves as a conductive lid (Figure 4.8A). Approximating the convecting magma body as well mixed and homogeneous in temperature and that the temperature gradient in the overlying conductive lid is approximately linear, the heat balance of the magma body is approximate by

$$\left(\rho c + \rho L \frac{dF}{dT}\right)\frac{dT}{dt} y = q_b - k\frac{T}{z} \qquad (4.6)$$

where ρ is the density of the magma (crystals + melt), c is the heat capacity of the magma, L is the total latent heat, F is melt fraction, T is the temperature of the magma, y is the thickness of the magma body, z is the thickness of the overlying crustal conductive lid, and k is thermal conductivity (see supplemental data). The left-hand side represents the heat content of the magma body and includes the effect of latent heat, where dF/dT represents the efficiency of latent heat release per unit temperature change. The first term on the right-hand side represents basal mantle heat flux (q_b) into the magma body and the second term represents conductive heat loss to the surface of the Earth through the crustal lid, where surface temperature is assumed to be zero (Huber et al., 2009). Integration of this equation, valid only above the solidus, shows that the magma body cools exponentially with time

$$T = \left(T_o - \frac{q_b z}{k}\right)\exp\left(-\frac{t}{\beta z}\right) + \frac{q_b z}{k} \qquad (4.7)$$

where T_o is the initial temperature of the magma body and $\beta = \left(1 + \frac{L}{c}\frac{dF}{dT}\right)\frac{y\rho c}{k}$.

The actual time τ_{life} to cool to near solidus temperatures, T_s, is then given by

$$\tau_{life} = \beta z \ln\left(\frac{T_o - q_b z/k}{T_s - q_b z/k}\right) \qquad (4.8)$$

The characteristic timescale of cooling scales linearly with the thickness z of the overlying crustal lid. However, because the temperature of a steady state geotherm increases with depth, it takes much longer to cool a deep magma body so the *time for solidification* increases nonlinearly with depth; this can be verified by inspecting the denominator in the parenthesis term in Eq. 4.8. Deep crustal magma bodies thus live longer than shallow ones; for example, a 2 km thick magma body at 5 km depth freezes in ~50 ky and at 10 km depth freezes in ~150 ky (Figure 4.8C).

By tracking how the composition of residual melts evolves during the cooling of the magma body (as done in the previous section), we can track how residual melt composition varies as a function of time. If melt segregation timescales are less than 50-100 ky (Cooper and Kent, 2014), it can be seen that the lifespans of magma bodies at depths greater than 10 km are longer than the segregation timescale $\tau_{life} > \tau_{seg}$), so intermediate magmas are expelled (Figure 4.8C). For magma bodies at depths of 5 km or less, $\tau_{life} < \tau_{seg}$, so magma bodies mostly freeze before any residual melts can segregate, preserving more primitive compositions. Any melts that do segregate can only be of late origin and must therefore be of low melt fraction and high silica content (Figure 4.8C). Segregation of silicic liquids, driven either by hindered settling or compaction, is inefficient: segregation timescales are on the order of 10-100 ky for hindered settling and 1-100 ky for compaction, indicating that even for small volumes of silicic melt, $\tau_{seg} \sim \tau_{life}$ in thin crust and $\tau_{life} >> \tau_{seg}$ in thick crust (Bachmann and Bergantz, 2004; Lee et al., 2015a).

If mantle-to-crust transit times (stage 1) and the depths of crustal magma bodies (stage 2) are controlled by crustal thickness, these models, despite their simplicity, can explain the distribution of silica in arc settings of different elevation and crustal thickness. As discussed above, thin crust favors less evolved, basaltic magmas, but allows for late segregation of silicic, low *F* residual melts, explaining why the most silicic magmas occur in thin arcs even when such arcs average basaltic. By comparison, thick crust favors intermediate magma compositions and prevents the formation of highly silicic magma bodies because melt segregation occurs well before most of the magma has crystallized and approached the highly silicic window. Instead, in thick crust, intermediate melts are segregated, which rise rapidly to the surface or erupt, freezing in the intermediate melts and never allowing an opportunity to generate highly silicic magmas.

We recognize that our two-stage model presented here is a simplification and there are many complications we have not considered. For example, growth of a thermal boundary layer within the magma body would slow cooling, while hydrothermal circulation in the upper crust would enhance cooling. We have also not considered how melt segregation rates vary as a function of cooling and melt

crystallinity. However, these complicating and, in some cases, competing processes will not change the first order conclusions drawn from our simple two stage model for magmatic differentiation.

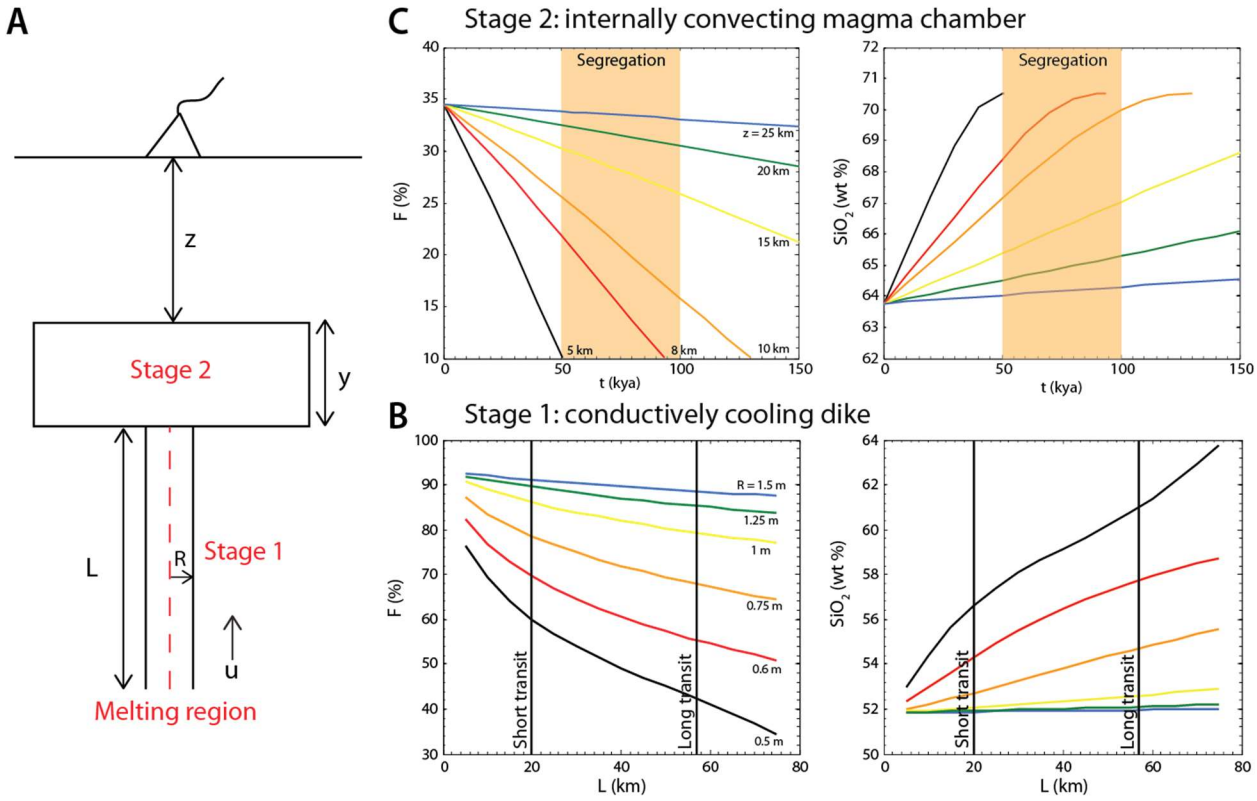

Figure 4.8. Modeling the thermal and compositional evolution of a basaltic parental melt. (A) Schematic illustration of a two-stage model of melt ascent and cooling. In stage 1, the melt rises through a dike while conductively cooling. After ascending through the dike, melt ponds in a crustal magma chamber. Magma chamber (stage 2) convectively cools, but vertical heat loss out of the magma chamber is limited by conductive heat loss through the crustal lid. (B) Results for stage 1 calculations showing the effect of transit distance (L) on crystallization extent as measured by residual melt fraction F. Crystallization paths for different dike radii, which control velocity of magma ascent, are shown. Corresponding SiO_2 as a function transit distance and dike radius is also shown. (C) Model results for stage 2 calculations showing the effect of varying thickness of the crustal lid (z) on residual melt fraction F and SiO_2 content, assuming a 2 km thick magma body. It is assumed that thickness of crustal lid, that is, the depth of the magma chamber, likely correlates on average with crustal thickness.

4.4.3 On calc-alkaline differentiation

Superimposed on the extent of magmatic differentiation are differences in the degree of iron depletion, or calc-alkalinity. As discussed above, FeO^*_{5MgO} decreases systematically as elevation increases

(Figure 4.6A), with arc magmas erupted through thin crust being less calc-alkaline than those erupted through thick crust. Any successful hypothesis for the origin of calc-alkaline differentiation must therefore explain why iron depletion correlates with crustal thickness and silica enrichment. One way to generate iron depletion is by mixing mafic parental magmas with iron-poor crustal materials or evolved melts, a process that would seem more likely in thick crust (Davidson et al., 1987; Dungan et al., 2001; Hildreth and Moorbath, 1988). However, to generate large quantities of iron-depleted intermediate magmas, such as andesites, by mixing basalts and iron-poor silicic melts, such as rhyolite, requires similar proportions of rhyolite and basalt based on the fact that basalts have ~50 wt. % SiO_2, rhyolites have ~70 wt. % SiO_2 and intermediate magmas have anywhere from 60-65 wt. % SiO_2. As shown in Figure 4.7, rhyolitic melts represent <10% residual melt fractions, so there is not enough rhyolitic melt formed to support the formation of intermediate magmas by mixing rhyolite with basalt.

The most popular hypothesis for iron depletion involves early saturation of magnetite, which is widely thought to be caused by high oxygen fugacities and also helps drive silica enrichment (Brounce et al., 2014; Sisson and Grove, 1993; Zimmer et al., 2010). For completeness, we have reproduced these effects of oxygen fugacity by modeling equilibrium crystallization of a primitive basalt (composition given above) with Rhyolite-MELTS using different oxygen fugacities (Figure 4.4B). Melting of subarc mantle, metasomatized by oxidized fluids derived from dehydration of the subducting oceanic lithosphere, has been the dominant mechanism invoked for generating oxidized magmas (Grove et al., 2012; Kelley and Cottrell, 2009), but why oxygen fugacity and water content would be higher in arc magmas traversing thick crust is not obvious. Another possibility is that thicker crust constrains flow in the mantle wedge, decreasing the extent of mantle wedge decompression and therefore the degree of mantle melting (Karlstrom et al., 2014; Plank and Langmuir, 1988; Turner and Langmuir, 2015a, b). Because hydrogen and ferric iron are highly incompatible during melting of mantle peridotite, lower degree melts of the mantle will be more oxidized and enriched in water. Consequently, mantle melts generated beneath thicker crust would tend to be more enriched in water and ferric iron, the latter manifested in melts as higher oxygen fugacity. In this "source" view, the conditions for calc-alkalinity

are defined in the mantle, but controlled primarily by melting process rather than composition (Gaetani, 2016; Turner and Langmuir, 2015a, b).

Magma chamber processes have also been invoked to explain the correlation of oxygen fugacity, water and crustal thickness, in part because of some suggestions that the mantle source of arc magmas is not particularly oxidized (Lee et al., 2005; Lee et al., 2012; Lee et al., 2010; Mallmann and O'Neill, 2009). Specifically, deep crustal magma chambers, preceding transport to (stage 1) and storage in the middle to upper crust (stage 2) and undergoing simultaneous crystal segregation and magmatic recharge will drive incompatible components, such as water and ferric iron, to rise in concentration in the melt, beginning with only moderate amounts of these two components. However, magmatic recharge could buffer the concentrations of compatible elements, such as Mg, which, in the absence of recharge, would decrease rapidly with crystal fractionation (Lee et al., 2014; O'Neill and Jenner, 2012). Lee et al. (2014) showed that simultaneous recharge and crystallization will generate semi-primitive parental magmas with high water and ferric iron content, from which subsequent crystal fractionation proceeds along a high oxygen fugacity, calc-alkaline trend. Notably, the ferric iron content of the recharging magma need not be unusually high to begin with to generate oxidized and water-rich derivative magmas through recharge. In this view, iron oxidation state is imparted during deep intracrustal differentiation.

It is beyond the scope of this paper to further evaluate these hypotheses. What is robust is that crustal thickness modulates the onset of iron depletion. Higher oxygen fugacities are favored in arc magmas traversing thick crust, suggesting that the dynamics of melt generation or fractionation control oxygen fugacity rather than source composition.

4.4.4 *Depth of differentiation*

Finally, we note that the correlation of crustal thickness with elemental ratios such as La/Yb and Gd/Yb (Figure 4.5), which indicate the involvement of garnet (a lower crustal mineral phase) during melting (Fujimaki et al., 1984; Green et al., 2000; Hauri et al., 1994; Sisson, 1994), confirms that magmas traversing thick crust undergo extensive crystal fractionation in the deep crust (Chapman et al., 2015;

Chiardia, 2015). These deep crustal fractionation zones very likely occur at the base of the crust. For thin crust, La/Yb and Gd/Yb do not vary with crustal thickness, but after crustal thickness exceeds ~43 km, they begin to rise. After converting crustal thickness to pressure, we find that this critical thickness corresponds remarkably with the pressure (1.2 GPa) at which garnet first stabilizes in hydrous mafic systems (Alonso-Perez et al., 2008). The presence of garnet-bearing cumulates in deeply exposed arc sections (DeBari and Sleep, 1991; Greene et al., 2006; Jagoutz, 2010; Jagoutz et al., 2009) and of garnet-bearing cumulate xenoliths from lower arc crust and upper mantle (Chin et al., 2014; Ducea and Saleeby, 1998; Erdman et al., 2016; Esperanca et al., 1988; Lee et al., 2006) demonstrate the importance of deep crustal differentiation in controlling subsequent differentiation in the crust.

4.5 Conclusions and implications for continent crustal formation

We showed that the average composition of arc magmas varies with crustal thickness. On average, arc magmas are more silicic and iron-depleted in thick crust compared to thin crust. This indicates that arc magmas undergo more extensive differentiation in thick crust, which can be readily understood by the longer transit times of magmas traversing thick crust. Using coupled thermal and thermodynamic modeling, our study provides a quantitative explanation of why continental arcs are andesitic and island arcs are basaltic.

Second, we showed that the most silicic magmas in arc settings are, surprisingly, not found in thick arcs, which average more silicic than magmas in thin arcs. Instead, it is in the more basaltic, thin arcs where the most silicic magmas are found. We show that the paucity of highly silicic magmas in thick arcs and their over-representation in thin arcs may be explained by the relative timescales of magma body lifespans and crystal-melt segregation rates, the former scaling with magma chamber depth, which roughly scales with crustal thickness.

Third, we showed that the more iron-depleted nature of arc magmas traversing thick crust indicates that the onset of magnetite differentiation occurs earlier in thick crust. This observation requires that the oxidation state of iron in magmas is higher in thick arcs compared to thin arcs.

To conclude, because the average composition of the continental crust is andesitic and iron-depleted, it seems that crustal thickening, which promotes deep crustal differentiation, is a crucial step in making continental crust. This suggests that continental crust may be preferentially formed in continental arcs or during magmatic orogenic events, where thin basaltic crusts (island arcs or oceanic crust) are thickened and reprocessed.

Chapter 5

On the timing of K-feldspar crystallization and origin of megacrysts in granitic rocks by late-stage liquid segregation

K-feldspar megacrysts in granitic rocks have prompted an ongoing debate on the timing of K-feldspar crystallization and growth of exceptionally large crystals. Field observations of megacrysts have suggested early saturation, while experimental work indicates K-feldspar crystallizes late. Here we resolve this apparent paradox by assessing the timing of K-feldspar crystallization in granitic rocks from the Bernasconi Hills pluton in the Peninsular Ranges of southern California. Textural observations show that rocks with K-feldspar contain relatively inclusion-free subhedral to euhedral crystals and have in excess of 1.5 wt % K_2O, whereas those without K-feldspar are comprised of quartz and plagioclase with interstitial biotite and contain < 1.5 wt % K_2O. Interestingly, the appearance of K-feldspar coincides with an increase in slope on a K_2O versus SiO_2 variation diagram that defines a continuous trend from K-rich, K-feldspar-bearing rocks to K-poor, K-feldspar-absent rocks. This suggests that K-feldspar-bearing rocks represent K-rich liquids segregated from plagioclase-quartz 'cumulates'. We estimate that alkali feldspar crystallization began late, with 10-16 % melt remaining, relative to a gabbroic parental composition, but occurred early in the crystallization of the segregated liquid. Comparison of our study with work on megacrystic granites suggests that megacrysts originate in a similar fashion and also crystallize late, compared to appropriate parental compositions. Near constant Zr-in-titanite temperatures reported for titanite inclusions within megacrysts indicate that crystals grow under near-isothermal conditions. Previous thermodynamic modeling on tonalitic compositions shows that near isothermal conditions are reached when the melt is H_2O-saturated, resulting in delayed release of latent heat. Collectively, this suggests that megacrysts grow under H_2O saturated conditions, late in the life of a magma body. Finally, we speculate that silicic lavas and ignimbrites with large sanidine may have a genetic relationship with megacrystic magmas.

5.1 Introduction

The timing of alkali feldspar crystallization in granitic magma has been debated extensively, particularly with regard to the origin of large megacrysts. Studies of K-feldspar crystallization have presented an apparent paradox with experimental work on granitic compositions indicating late crystallization, after all other phenocryst phases, while field observations of K-feldspar megacrysts suggest early saturation, in melt-rich settings, and long growth times (Johannes and Holtz, 1996; Johnson and Rutherford, 1986; Kerrick, 1969; Vernon and Paterson, 2008; Whitney, 1988). Further complication is presented by the occurrence of large (1-2 cm) sanidine phenocrysts in dacite and rhyolitic tuff (Bachmann et al., 2002; Balducci and Leoni, 1981; Clavero et al., 2004; Steven and Ratte, 1960), which indicate K-feldspar growth begins when the crystal content of the magma is below 40-50 %, prior to the rheological lock-up point for silicate melts (Huber et al., 2010; Marsh, 1981). Recent work on megacrystic granites supports late crystallization and has indicated that growth occurs under near-isothermal conditions (Moore and Sisson, 2008), possibly due to thermal buffering by recharge magmas (Glazner and Johnson, 2013; Johnson and Glazner, 2010; Moore and Sisson, 2008). However, it remains unclear how much of a role incremental magma injection plays in facilitating the growth of large crystals compared to down-temperature crystal fractionation. Furthermore, it remains perplexing as to how K-feldspar can saturate late, but still appear to have grown in a melt-rich setting.

Here, we examine the timing of K-feldspar growth using textural and geochemical systematics of granitoids from the Bernasconi Hills pluton, in the Peninsular Ranges Batholith in southern California. We identify two groups of samples based upon the presence of K-feldspar and K_2O content. K-feldspar-bearing samples have > 1.5 wt % K_2O and contain subhedral to euhedral K-feldspar phenocrysts. The feldspars themselves have rare quartz and plagioclase inclusions, but otherwise have the appearance of an early crystallizing phase (e.g. well defined crystal faces). In contrast, K-feldspar-absent samples have < 1.5 wt % K_2O and are composed of plagioclase and quartz with interstitial biotite. Examination of K_2O-SiO_2 systematics shows an increase in slope at ~70 wt % SiO_2, corresponding to K_2O contents of ~1.5 wt

% and coincident with the appearance of K-feldspar. Interestingly, several silicic, K_2O-poor samples plot along the same trend as K-feldspar-bearing samples. Based upon these textural and geochemical observations, we suggest that K-feldspar-bearing lithologies represent late segregated melts, while silicic K-feldspar-absent samples represent the complementary cumulates. Comparison of our case study to work on megacrystic granites further suggests that K-feldspar megacrysts form similarly to the feldspars described here, but grew to large sizes due to delayed latent heat release under prolonged H_2O-saturated conditions. We further speculate that large (1-2 cm) sanidine phenocrysts described in dacites and rhyolitic ignimbrites in several locations (Bachmann et al., 2002; Balducci and Leoni, 1981) may represent the eruptive equivalents to the late segregated liquids that give rise to K-feldspars in granitic plutons.

5.2 Methods

5.2.1 Geochemical Data

Whole-rock compositions for enclaves and host rocks samples from the Bernasconi Hills pluton were determined by X-ray fluorescence spectrometry of fused glass disks at Washington State University, Pullman (analytical details in Farner et al., submitted). Compositional data for megacrystic granites in this study were compiled from the literature along with estimates of modal mineralogy, when available (Bateman et al., 1988; Hirt, 1989; Morton et al., 2014)

5.2.2 Micro-XRF elemental mapping

Elemental mapping of thin sections and polished rock slabs was carried out using a Horiba XGT-7200 X-ray analytical microscope at Rice University. As described by Jiang et al. (2015), this instrument is equipped with two interchangeable X-ray guide tubes (50 and 400 μm diameter) with a Rh target and an energy dispersive Si drift detector capable of detecting elements in the mass range Na-U. Mapping was performed under full vacuum conditions with

the 50 μm guide tube, 30 kV accelerating voltage and 600 s survey time per frame over 4-5 accumulations. Compositional maps generated by micro-XRF were post-processed using the ImageJ software package to determine mineral modal proportions in each sample.

5.3 Results

Elemental mapping shows that samples fall into two textural groups defined by the presence of K-feldspar. Samples with K-feldspar characteristically lack biotite and contain > 1.5 wt % K_2O (Figures 5.1 and 5.2). K-feldspar crystals in these samples typically occur as subhedral to euhedral phenocrysts (Figure 1) and contain occasional rounded inclusions of quartz and plagioclase. Additionally, symplectic intergrowths of quartz and K-feldspar are common along the margins of K-feldspar phenocrysts and sometimes occur with rare myrmekite intergrowths. In contrast, K-feldspar-absent samples are composed mainly of quartz and plagioclase with interstitial biotite (Figure 5.1). These rocks contain < 1.5 wt % K_2O (Figure 5.2), and lack symplectic intergrowths. Interestingly, almost all of the K-feldspar-bearing samples occur near the center of the Bernasconi Hills pluton within a ~15 m wide zone that is free of mafic enclaves.

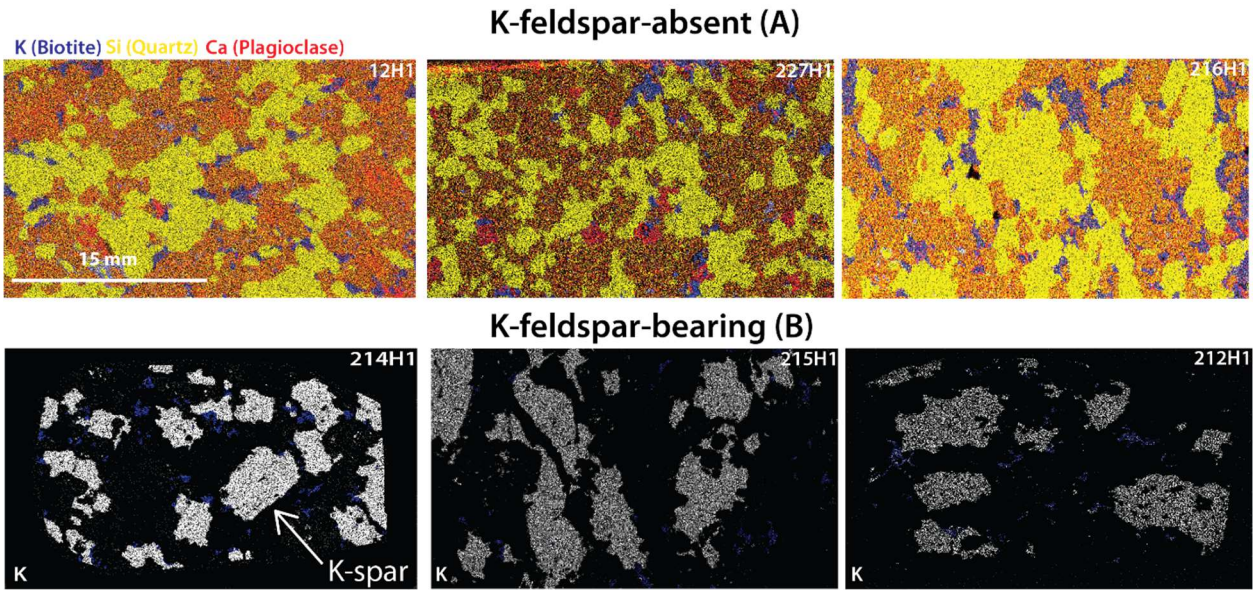

Figure 5.1. Micro-XRF compositional maps showing representative samples from our case study. (A) K-feldspar-absent rocks are composed primarily of plagioclase (red) and quartz (yellow) with small, interstitial biotite (blue). (B) K-feldspar-bearing rocks are dominated by subhedral to euhedral K-feldspar phenocrysts (white) and contain very little biotite (blues). Note that the scale bar applies to all photos.

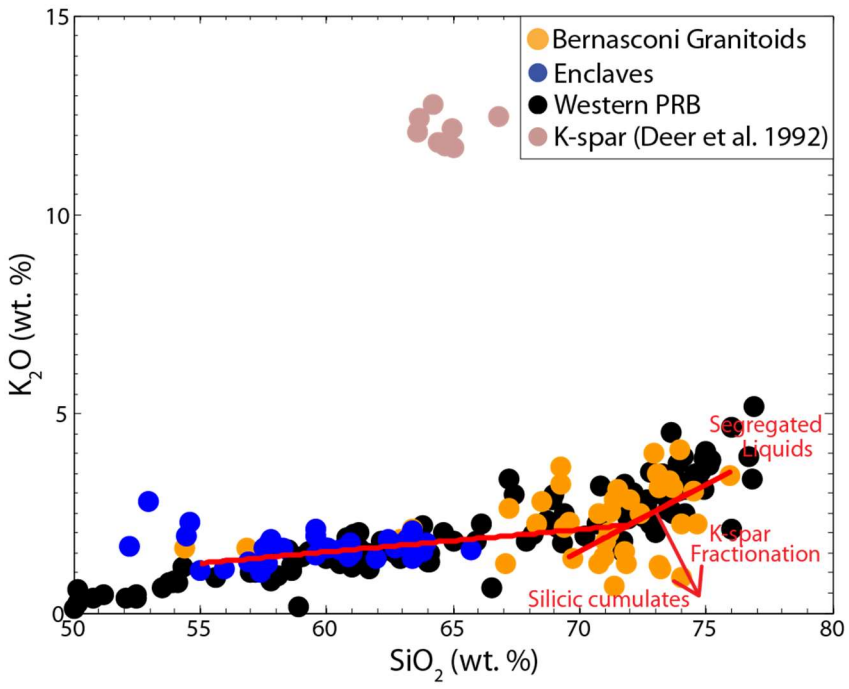

Figure 5.2. Variation diagram of K_2O versus SiO_2 for western Peninsular Ranges plutons and Bernasconi Hills granitoids and enclaves. Representative K-feldspar compositions are also plotted for comparison (Deer et al., 1992). Comparison of linear least-squares regression lines of Bernasconi Hills data for intermediate and silicic samples shows a distinct increase in slope starting at ~70 wt % SiO_2. The steep trend defined by samples with > 70 wt. % SiO_2 contains K-rich, K-feldspar-bearing rocks and K-poor plagioclase-quartz cumulates. Additionally, there is no decrease in K_2O with increasing SiO_2, indicating that K-rich melts do not segregate from K-feldspar.

5.4 Discussion

5.4.1 Timing of K-feldspar crystallization

Given the close spatial proximity of the textural groups described above, it is of interest to examine why K-feldspar crystallization primarily occurred in a narrow zone within the pluton. We begin by estimating the timing of K-feldspar crystallization relative to an evolved gabbroic composition from the western Peninsular Ranges (Lee et al., 2007; Morton et al., 2014). The gabbro composition used here represents a differentiated basalt thought to be parental to the more evolved magmas in the batholith. Assuming closed system behavior, we can estimate the effective melt fraction *F* remaining in a magma

reservoir relative to a parental composition as the inverse of the ratio of a perfectly incompatible element ($D_i = 0$) in an evolved magma (C) relative to the parent magma (C_o), such that $F = C_o/C$. Here, we estimate F with potassium because it varies by less than a factor of 2 in gabbroic reference compositions compared to the nearly ten-fold enrichment in Peninsular Ranges granitoids and hence behaves as a perfectly incompatible element during magma differentiation. Using potassium, we estimate that alkali feldspar crystallization begins when 10-16 % melt remains, relative to the parental composition (Figure 3). This agrees well with late K-feldspar crystallization noted in experimental studies (Johannes and Holtz, 1996; Johnson and Rutherford, 1986; Whitney, 1988), but does not explain the apparent evidence for crystallization in a melt-rich environment noted in field-based studies (Bachmann et al., 2002; Kerrick, 1969; Vernon and Paterson, 2008).

We can further evaluate the conditions of K-feldspar crystallization using K_2O-SiO_2 systematics of the Bernasconi Hills pluton and western Peninsular Ranges. As discussed by Lee and Morton (2015) for the Peninsular Ranges Batholith, incompatible-rich liquids and complementary incompatible depleted cumulates can be readily identified based upon kinks or changes in slope on element-element variation diagrams. In detail, silicic cumulates and residual liquids define a linear trend that is distinguished from the trend defined by low and intermediate SiO_2 samples by a substantial difference in slope (Lee and Morton, 2015). As illustrated in Figure 5.2, there is a distinct change in the trend of the data at ~70 wt. % SiO_2, where least squares regression lines for intermediate and silicic compositions intersect. Along the silicic regression, there are several K-feldspar-absent samples with > 68 wt % SiO_2 and low K_2O (< 1.5 wt. %) that plot along the same linear regression as K-feldspar-bearing samples with high SiO_2 and K_2O. Collectively, these geochemical systematics and textural observations suggest that K-feldspar-bearing rocks represent late stage K-rich liquids that segregated from silicic plagioclase-quartz cumulates. This further suggests that while K-feldspar forms late in the overall thermal history of the magma reservoir, it may saturate early in the cooling history of segregated melt, producing crystals with textural features of an early phase and thus appear to have grown in a melt-rich environment. Finally, above ~70 wt % SiO_2,

there is no change in slope of the data array, indicating that liquids do not segregate again after initial segregation from the silicic cumulate.

5.4.2 On the origin of megacrysts

Much of the debate on the timing of K-feldspar crystallization has been motivated by the size and euhedral character of megacrysts, which suggest crystallization began in a melt-rich environment, and hence, early in the cooling of a magma body (Bateman, 1992; Cox et al., 1996; Kerrick, 1969; Vernon, 1986). However, as described above, late-stage segregation may also produce crystals with these features, raising the possibility that megacrysts originate similarly to the K-feldspar described in our case study. Comparing compositional and modal data from our case study to data compiled from selected megacrystic granitoids, we find that there is substantial overlap between different megacrystic intrusions and our case study (Figure 5.3A). Additionally, using appropriate parental magma K_2O compositions for each intrusion, we estimate that K-feldspar crystallization occurs late in all cases, when ~10-20 % melt remains (Figure 5.3B). This indicates that megacrysts do form late, relative to parental magmas, and supports the notion that megacrysts derive from K-rich segregated liquids (Figure 5.4).

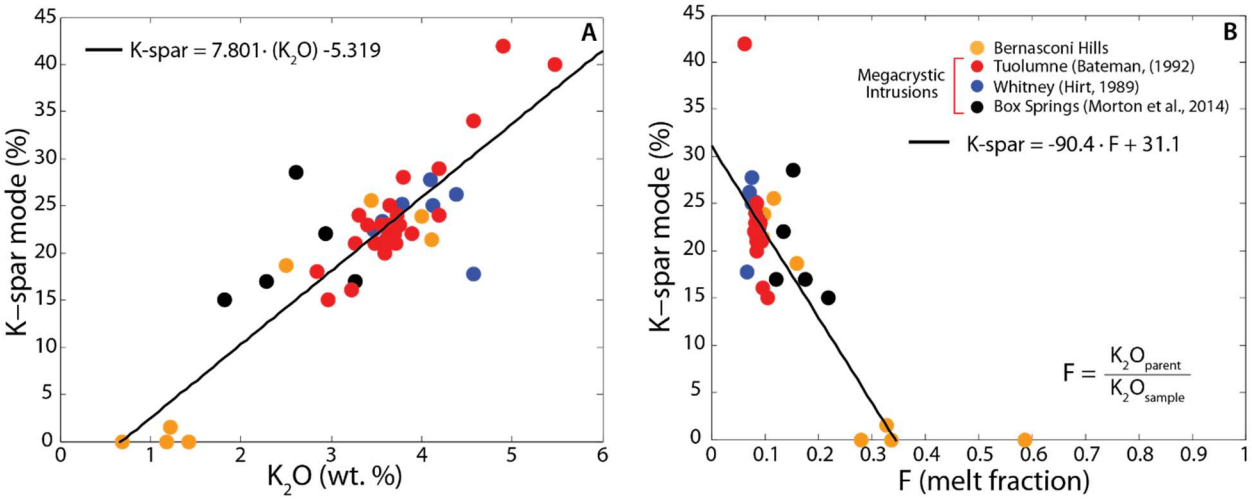

Figure 5.3. (A) K-feldspar content versus K_2O for Bernasconi Hills samples and data compiled from the Tuolumne and Whitney Intrusive Suites in the Sierra Nevada Batholith and the Box Springs Complex in the Peninsular Ranges Batholith (Bateman et al., 1988; Hirt, 1989; Morton et al., 2014). (B) K-feldspar mode versus estimated melt fraction (*F*) relative to parental compositions.

If late segregation of K-rich melts does indeed give rise to megacrysts, it is necessary to consider why some crystals grow to megacrystic sizes while others do not. Previously reported Zr-in-titanite temperature estimates for titanite inclusions in megacrysts (Moore and Sisson, 2008) indicate that megacryst growth occurs over a limited range of temperatures (~720-760°C), corresponding to near-solidus conditions for H_2O-saturated granitic melts (Holtz et al., 1992; Huang and Wyllie, 1975; Johannes and Holtz, 1996; Whitney, 1988). Based upon these estimates, it has been proposed that the temperature of the system is buffered by repeated intrusion of felsic magma into a feldspar-bearing magma reservoir (Glazner and Johnson, 2013; Johnson and Glazner, 2010; Moore and Sisson, 2008). Interestingly, temperature estimates for titanites adjacent to megacrysts show a slightly larger variation from core to rim, but are consistent with thermal buffering. Incremental injection of felsic magma may indeed operate at some level in buffering the temperature of a magma body (Coleman et al., 2004; Matzel et al., 2006), but it is not the only means of doing so.

Another possible way to maintain near-isothermal conditions is by delayed latent heat release under H_2O-saturated conditions. Thermodynamic modeling has illustrated that increasing H_2O content in silicic melt suppresses crystallization to near-solidus temperatures due to saturation of a coexisting fluid phase, which causes eutectic-like behavior and delays latent heat release (Farner et al., 2014; Lee et al., 2015a). As shown quantitatively by Lee et al. (2015), the delay in latent heat release increases the crystallization time of the melt by a factor of ~2, predicting a thermal lifespan for a water-saturated tonalitic magma of ~0.8 Ma, from liquidus to solidus. This provides ample time to grow a 5 cm wide crystal, based upon experimental growth rates on the order of 10^{-6}-10^{-10} cm/s for K-feldspar (Swanson, 1977) and predicts minimum growth rates (assuming growth takes 0.8 Ma) of $2 \cdot 10^{-13}$ and $9 \cdot 10^{-14}$ cm/s for crystals with radii of 2.5 and 5 cm (r_{xtal}), respectively, where growth rate is estimated by $G = r_{xtal}/\Delta t$. We emphasize that these represent minimum growth rate estimates as K-feldspar growth is likely faster under H_2O-saturated conditions since dissolved H_2O in the melt increases the diffusivities of virtually all elements (Zhang et al., 2010), thereby enhancing grain growth.

Experimental studies of granitic compositions approximated by the system Quartz-Albite-Orthoclase-H_2O (Qtz-Ab-Or-H_2O) further illustrate the consequences of H_2O saturation on crystallization and provide context for field observations. Under dry conditions, a single feldspar phase crystallizes with quartz until minimum melting temperatures are reached and all of the melt has crystallized. In contrast, H_2O saturation causes the appearance of a ternary eutectic in the Qtz-Ab-Or system because addition of free H_2O reduces the variance of the system and expands the melt stability field, thereby forcing co-precipitation of two feldspars enriched in the albite and orthoclase components, respectively (Holtz et al., 1992; Johannes and Holtz, 1996; Luth, 1969; Tuttle and Bowen, 1958). The co-precipitation of albite- and orthoclase-rich feldspar is particularly important as megacrystic granites generally contain two or more feldspars as disparate phases (Glazner and Johnson, 2013; Hirt, 1989; Johnson and Glazner, 2010; Morton et al., 2014), requiring that the orthoclase-rich megacrysts saturated first, followed by smaller albite-rich crystals under H_2O-saturated conditions. Additionally, observations of miarolitic cavities in several field studies further confirm that megacrystic melts are water-rich and likely hit saturation (Glazner and Johnson, 2013; Hirt, 1989; Johnson and Glazner, 2010; Vernon, 1986).

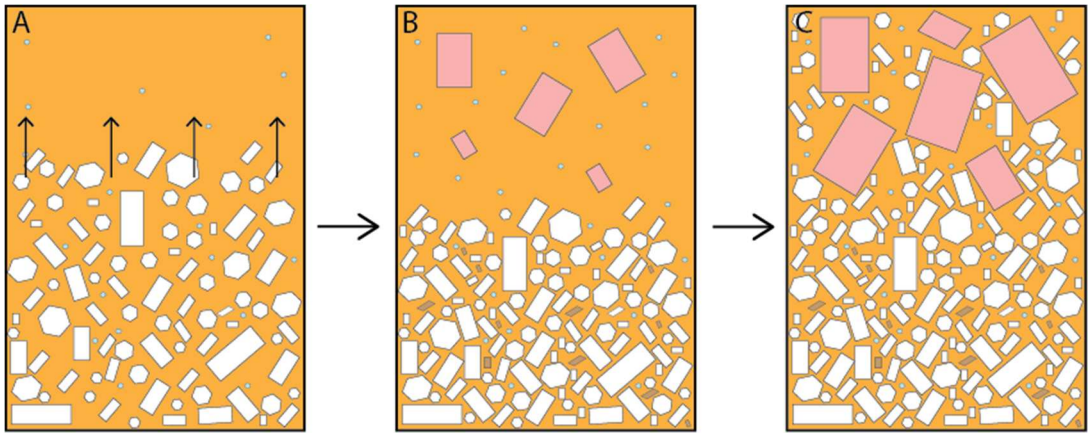

Figure 5.4. Schematic illustration of how K-feldspar crystals originate and grow from segregated melt. When the melt segregates, K-feldspar begins to grow. (A) Melt segregates from a cooling plagioclase-quartz matrix by compaction or hindered settling. (B) K-feldspar saturates and begins to grow, possibly under water-saturated conditions. (C) K-feldspar continues to grow from the water-saturated residual melt (Hexagon = quartz, rectangle = feldspars, parallelepiped = biotite, circle = free fluid phase).

5.4.3 Implications for the plutonic-volcanic connection

Several studies have reported 1-2 cm long sanidine phenocrysts in dacitic lavas and crystal-rich rhyolitic tuffs (Bachmann et al., 2002; Balducci and Leoni, 1981; Clavero et al., 2004; Steven and Ratte, 1960), which has prompted suggestions that such lavas may have a genetic relationship with K-feldspar-bearing granitoids (Bachmann et al., 2002). The occurrence of sanidine in volcanic rocks indicates that sanidine must have saturated while the crystallinity of the magma was below 40-50 % and hence still eruptible (Huber et al., 2010; Marsh, 1981), which is in contrast with late saturation observed by experimental studies. One possibility is that large sanidine phenocrysts may represent xenocrysts or disaggregated K-feldspar fragments from a cooling pluton and thus are not directly related to volcanic products (Glazner and Johnson, 2013). Another possibility is that evolved sanidine-bearing lavas represent late-stage segregated liquids, similar to those identified in the Bernasconi Hills pluton and Peninsular Ranges Batholith from geochemical systematics. As discussed above, incompatible-rich liquids may segregate late in the thermal history of a magma reservoir and precipitate K-feldspar as a liquidus phase, motivating the notion that these liquids could segregate and potentially erupt with a K-feldspar cargo.

5.5 Conclusions

We have examined the timing of K-feldspar growth using geochemical and textural systematics of granitic rocks from the Bernasconi Hills pluton in southern California. Our case study has identified two textural groups based upon the presence of K-feldspar where K-feldspar-bearing rocks have > 1.5 wt. % K_2O and contain subhedral to euhedral feldspars while K-feldspar-absent samples have < 1.5 wt. % K_2O. Geochemical systematics show that these rocks fall along a different trend from intermediate compositions samples and have complementary K-poor, plagioclase-quartz cumulates. Based upon textural and geochemical systematics we suggest that K-feldspar-bearing rocks represent late segregated liquids. Comparison with data from megacrystic granites further suggests that megacrysts originate in a similar fashion and grow to large sizes under H_2O-saturated conditions. Finally, we propose that silicic

volcanic rocks with large sanidine phenocrysts may represent the eruptive equivalents of late segregated liquids, implying a genetic relationship between dacitic and rhyolitic lavas and granitic plutons.

Chapter 6

Mapping geochemical and geologic variations in the Bernasconi Hills pluton

Mafic enclaves are common in granitic plutons and are taken as indicative of mafic-felsic magma interaction either by mingling or homogenization. Many studies of enclaves and their associated host rocks only consider compositional data in assessing the extent of interaction, neglecting important spatial relations. Here we present maps of two sampling transects with corresponding compositional data to place spatial constraint on enclave-host interaction. We also examine the trace element systematics of enclaves and granitoids. We find that enclaves are enriched in heavy rare earth elements compared to granitic rocks, which appears to be due to their higher hornblende content. Motivated by the high compatibility of heavy rare earth elements in hornblende, we show how specific compatible elements can be useful as indirect proxies of mineralogical variation. Finally, we apply this approach to K-feldspar using K_2O and Ba along with noted mineralogical variations from other work.

6.1 Introduction

Mafic enclaves are ubiquitous in silicic plutonic rocks and are observed in the field as dark centimeter to meter scale fragments within the surrounding host pluton. While enclaves generally have similar textural characteristics, they may variably represent entrained fragments of cogenetic cumulate, altered wallrock xenoliths, quenched mafic recharge magmas and disaggregated mafic dikes (Barbarin, 2005; Didier, 1973; Frost and Mahood, 1987; Liao et al.,

2013). Since enclaves can form through a variety of processes it is necessary to carefully evaluate their petrogenetic relationship to their host intrusion. Many enclave studies are primarily concerned with the textural and geochemical characteristics of individual enclaves and do not entirely place these observations into the context of their relationship with the enclosing host pluton or consider how the enclaves are distributed in the pluton. This may hinder a better understanding of a population of enclaves as they relate to the host intrusion.

In this case study, we present detailed field mapping accompanied by corresponding geochemical cross sections through the Bernasconi Hills pluton in southern California. We highlight the co-variation of geochemistry with map patterns and examine how mafic-felsic mingling is expressed on the compositions of spatially associated granitoids and enclaves. We also incorporate trace element data as a means of examining how mineralogy varies in enclaves and host rocks and how it is manifested in the field.

6.2 Geologic Background

6.2.1 Peninsular Ranges Batholith

The Peninsular Ranges Batholith represent part of an extensive magmatic arc active along the western margin of North America during the Mesozoic Era due to subduction of the Farallon Plate (Morton et al., 2014). The batholith begins to crop out near Riverside, California, USA and extends over 1500 km to the southern tip of the Baja California peninsula. Extensive field, geochemical and geochronologic studies of the Peninsular Ranges have demonstrated that the age and composition of the batholith vary from west to east across the batholith and have prompted the identification of an inferred tectonic suture between plutons that intruded an accreted island arc terrane to the west and plutons intruding the North American continent to the

east (DePaolo, 1981; Kistler et al., 2003; Kistler et al., 2014; Lee et al., 2007; Morton et al., 2014).

In detail, the western portion of the batholith contains a wide range of lithologies and is geochemically characterized by a continuous geochemical differentiation trend from evolved gabbroic compositions to high silica granites. As described by Lee and Morton (2015), plutons in the west are less silicic, on average, but some of the most evolved compositions in the northern part of the Peninsular Ranges are observed here. Plutons in the west yield shallow aluminum-in-hornblende emplacement pressures of 2-4 kbar and range in age between 130-95 Ma, spanning most of the intrusive history of the batholith (Morton et al., 2014; Premo et al., 2014).

Plutons east of the suture have a much more restricted geochemical range as mafic litholigies of any kind are virtually absent and high silica granites are apparently uncommon (Lee and Morton, 2015; Morton et al., 2014). Despite the paucity of high silica granites, the restricted geochemical range noted in eastern plutons has, in part, been attributed assimilation of sedimentary rocks based upon isotopic studies (DePaolo, 1981; Kistler et al., 2014). Compared to western plutons, intrusions east of the suture were emplaced more deeply (4-6.5 kbar) and later (95-85 Ma) based upon Al-in-hornblende barometry and zircon U-Pb geochronology (Morton et al., 2014; Premo et al., 2014).

6.2.2 Bernasconi Hills pluton

The Bernasconi Hills pluton is a small (~2 km wide) pluton exposed near Moreno Valley, California, in the western Peninsular Ranges (Mason and Cohen, 1990). The intrusion is mainly composed of biotite-hornblende granite and granodiorite with tonalite locally present throughout. As described in previous studies, fine grained mafic enclaves occur frequently in the pluton as

angular to rounded bodies with biotite-rich margins and equigranular cores dominated by quartz and plagioclase. Previous studies have identified enclave swarms throughout the pluton and noted a large (~15 m across, ~100 m high) swarm that cuts through the central portion of the pluton. This large swarm has been investigated in a companion paper to this study (Farner et al., submitted). This study is focused on a quarried portion of the pluton as it exposes a continuous section through the intrusion, making it an ideal place to correlate geochemical and mineralogical variations with variations in enclave distributions. Furthermore, the section also shows intimate mingling of the host granitoid and mafic enclaves. The quarried section consists of a series of ~3 m high terraces cut across ~170 m of the pluton and up to ~140 m from the base of the quarry.

6.3 Methods

6.3.1 Sampling Strategy

Samples were collected along two linear transects (60 and 120 m, respectively) across the quarried portion of the pluton. Each transect was divided into 5 m-wide segments and granite-enclave pairs were collected from each segment when possible. In some cases, enclaves were either not present or accessible at the outcrop, so some segments lack enclave data. This sampling approach enables us to construct geochemical cross sections of the pluton and associated enclaves for comparison with geologic maps of each transect, thus providing a spatial dimension to examining mafic-felsic interaction.

In several cases, particularly along the second transect, groundwater and moss growth have chemically weathered the rock face to a dark gray, causing host granitoids to superficially

resemble more mafic lithologies. Care was taken during sample collection to collect only minimally altered samples and remove any weathered material.

6.3.2 Enclave Mapping

Mafic enclaves along both sample transects described above were mapped from photographs of each 5 m segment stitched together in Adobe Illustrator. In order to ensure that the final maps are accurately stitched together, care was taking to make sure photos of each 5 m outcrop overlap with adjacent outcrops. Because our goal is to compare variations in enclave distribution with whole-rock compositions, each 5 m segment was scoured multiple times in order to map all enclave present. In some cases, it was necessary to modify the light balance or convert the color profile of the photographs because the sunlight in the original photo obscures portions of the outcrop, making it difficult to accurately identify enclaves.

6.3.3 Whole-rock geochemistry

Rock samples were ground to a fine powder in a ceramic Spex mill and whole-rock major element compositions were determined by wavelength dispersive X-ray fluorescence spectrometry (XRF) with a ThermoARL Advant'XP+ sequential XRF at Washington State University, Pullman (see Chapter 3, this volume for additional details).

Trace element compositions were determined by laser ablation inductively coupled plasma mass spectrometry (LA-ICP-MS) at Rice University with a ThermoFinnigan Element 2 magnetic sector mass spectrometer equipped with a New Wave 213 nm laser ablation system in both medium and low resolution modes ($m/\Delta m$ ~4000 and 300, respectively) with an 80 μm spot size. External standards were United State Geological Survey basaltic standards BHVO2g and

BCR2g and National Institute of Standards and Technology glass standard NIST-612. Prior to measuring unknowns, the instrument was tuned by adjusting the flow of the sample gas (Ar) to achieve a sensitivity of ~250000 cps on 15 ppm La in BHVO2g. Measured signal intensities were converted into concentrations using an in-house reduction program (http://cintylee.org/s/Laser-RAWDATA-TEMPLATE.xls), which subtracts background signal intensities and corrects for elemental fractionation with external standards. Signal intensities were then normalized using ^{30}Si and ^{43}Ca as internal standards for medium and low resolution measurements, respectively and time-resolved intervals were integrated to yield concentrations. Compositional data for major oxides and trace elements is given in Appendix B and Appendix G, respectively.

6.4 Results

6.4.1 Spatial distribution of mafic enclaves

Our mapping highlights the variability of enclave distributions in the pluton. One interesting observation is that enclaves often occur in locally dense populations, which we term enclave swarms (Figures 6.1 and 6.2). As described by several previous studies at Bernasconi Hills (Farner et al., submitted; Mason and Cohen, 1990), swarms superficially resemble mafic dikes that appear to have been disaggregated into discreet enclaves. In many cases, enclaves within and near swarms are highly attenuated and associated with biotite-rich schlieren. Additionally, enclaves near the margins of swarms have thick (~1 cm wide) biotite-rich rinds. In some cases, individual enclaves appear to preserve multiple generations of rinds with one rind developing as a previous layer delaminates from the parent enclave.

The first transect (Figure 6.1) provides excellent examples of enclave swarms as the rock face is relatively unweathered and it is easy to observe small, localized swarms in fine detail. Rocks along the second transect (Figure 6.2) have been altered to a dark gray color by moss growth and groundwater, making it difficult to clearly distinguish enclaves from granitoids in some places. A prominent ~15 m wide enclave swarm is partially shown in transect 2 (Figure 6.2) and is the largest congregation of enclaves in the pluton, rising through most of the quarry wall (~140 m), but much of this is obscured at the outcrop scale due to intense weathering of the enclaves and adjacent granitoid.

Coherent mafic bodies occur in several areas of the pluton, away from swarms (Figure 6.1). In the field, these are represented by 1-3 m wide volumes of dark gray rocks within the granitoid that do not appear to have been disaggregated into enclaves. Enclaves near mafic bodies are more angular and much less attenuated than enclaves within and around swarms. Rinds appear to be more uncommon in these settings and schlieren are also sparse, although in some instances, particularly along transect 1, ~1-2 cm biotite phenocrysts occur in the interior of mafic bodies.

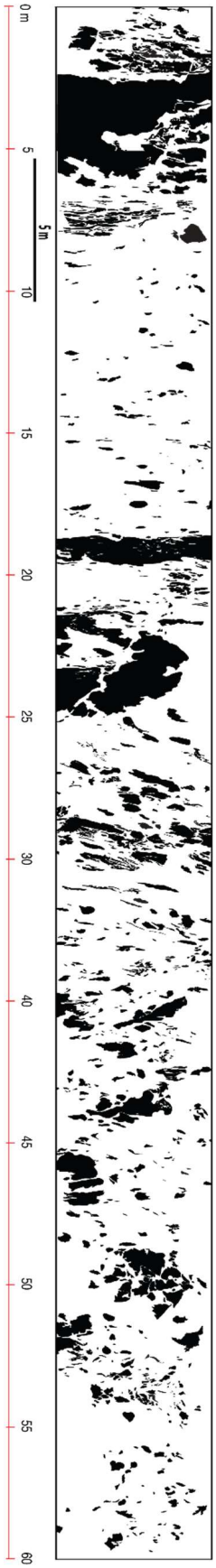
0 m
5
5m
10
15
20
25
30
40
45
50
55
60

Figure 6.1 (above) Map of transect 1 of the Bernasconi Hills pluton. Black indicates mafic enclaves and white indicates host granitoid rocks. Distance along the transect is noted in meters along the bottom of the map

6.4.2 Relationship with geochemistry

Examination of geochemical transects (Figures 6.3-6.6) shows that the host pluton has a relatively constant composition with respect to major elements except for K_2O and Na_2O. In both transects, we observe variations in the alkalis on the order of 1-2 wt. % (Figures 6.3 and 6.5), most likely reflecting variations in feldspar abundance (particularly K-feldspar) and composition. In the second transect, granitoid compositions approach and overlap with enclave compositions between ~95-110 m, co-incident with the ~15 m wide enclave swarm previously discussed. Trace element contents are much more variable in the host pluton, particularly with respect to Ba, Sr and heavy rare earth elements (HREE) (Figures 6.4and 6.6).

Enclave major element compositions are variable over the length of transect 1 (Figure 6.3) and show systematic increases in FeO^* (total Fe cast as Fe^{2+}), MgO, and CaO with a corresponding decrease in SiO_2 over the same distance, corresponding to the appearance of a large mafic body. The alkalis also increase in this area concomitant with increasing Rb and U, but it is slightly offset from the changes noted for FeO^*, MgO and CaO. Enclaves in transect 2 are broadly similar in composition, but appear to vary at the scale of ~5-10 m (Figure 6.5). Curiosly, enclaves are enriched in U and HREEs compared to the granitoids (Figures 6.7).

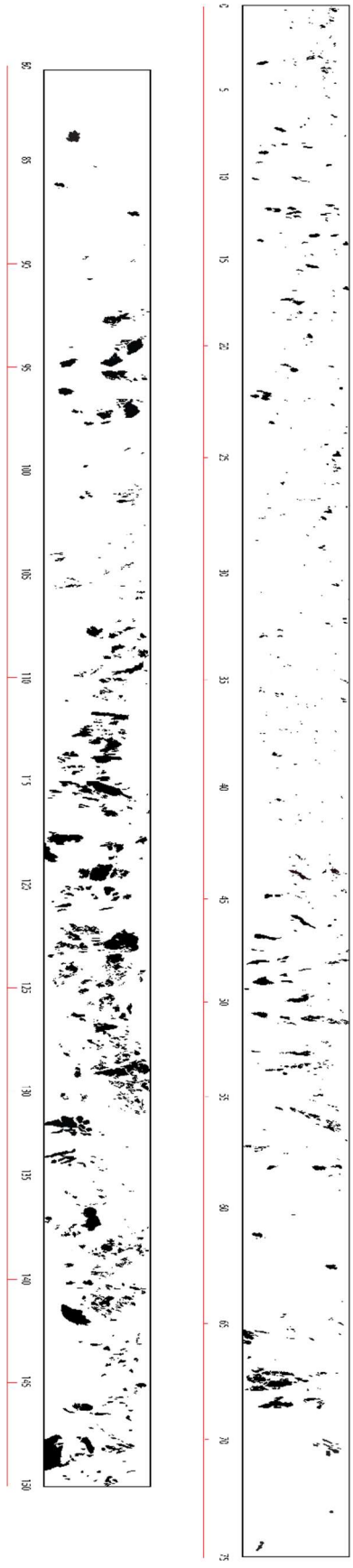

Figure 6.2. (above) Map of transect 2 of the Bernasconi Hills pluton. As in the previous map, black indicates mafic enclaves and white indicates host granitoid rocks. The map is broken into two sections to allow it to fit on the page. Distance along the transect is noted in meters at the bottom of the map.

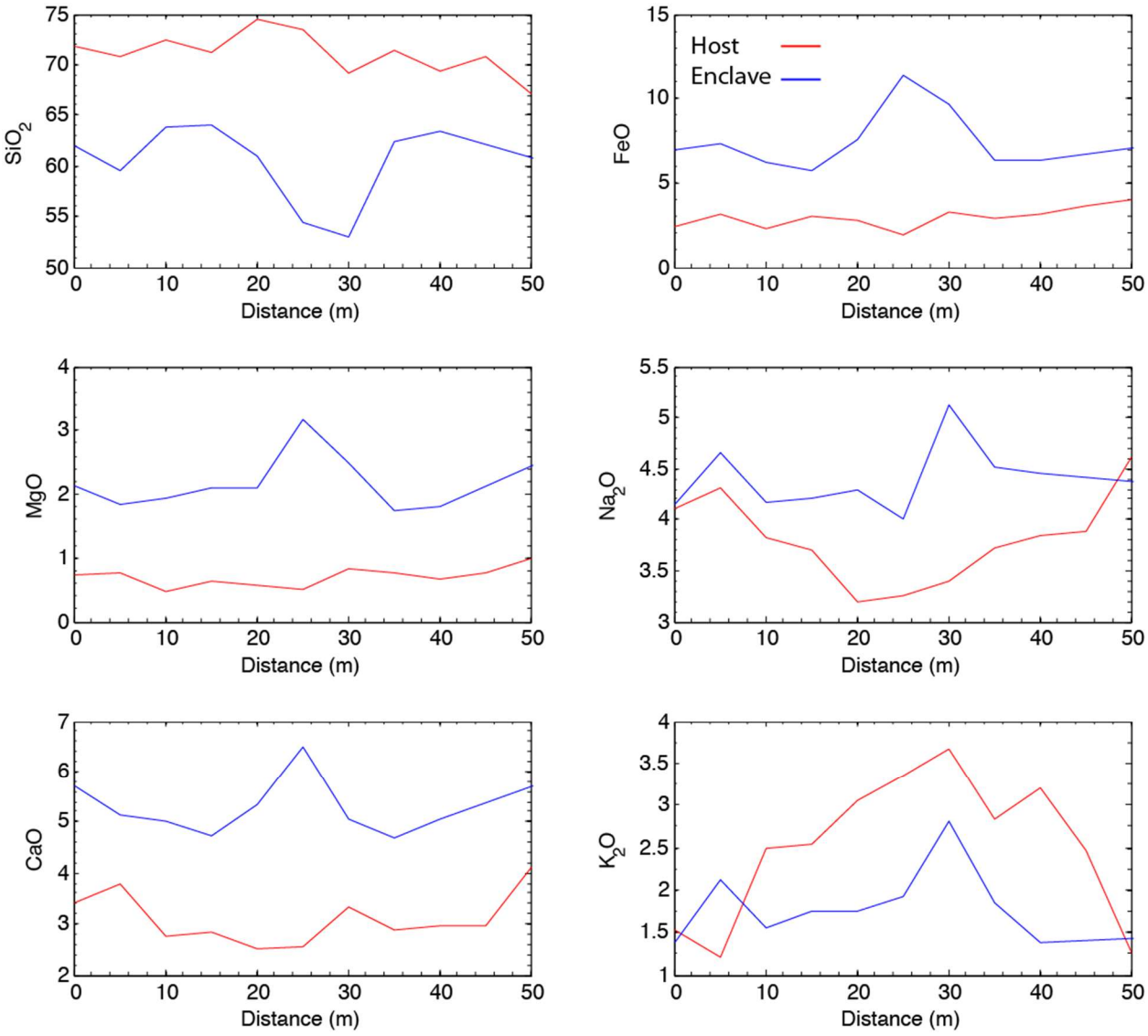

Figure 6.3. Major element geochemical section corresponding to transect 1. Granitoids are shown in red and enclaves are in blue.

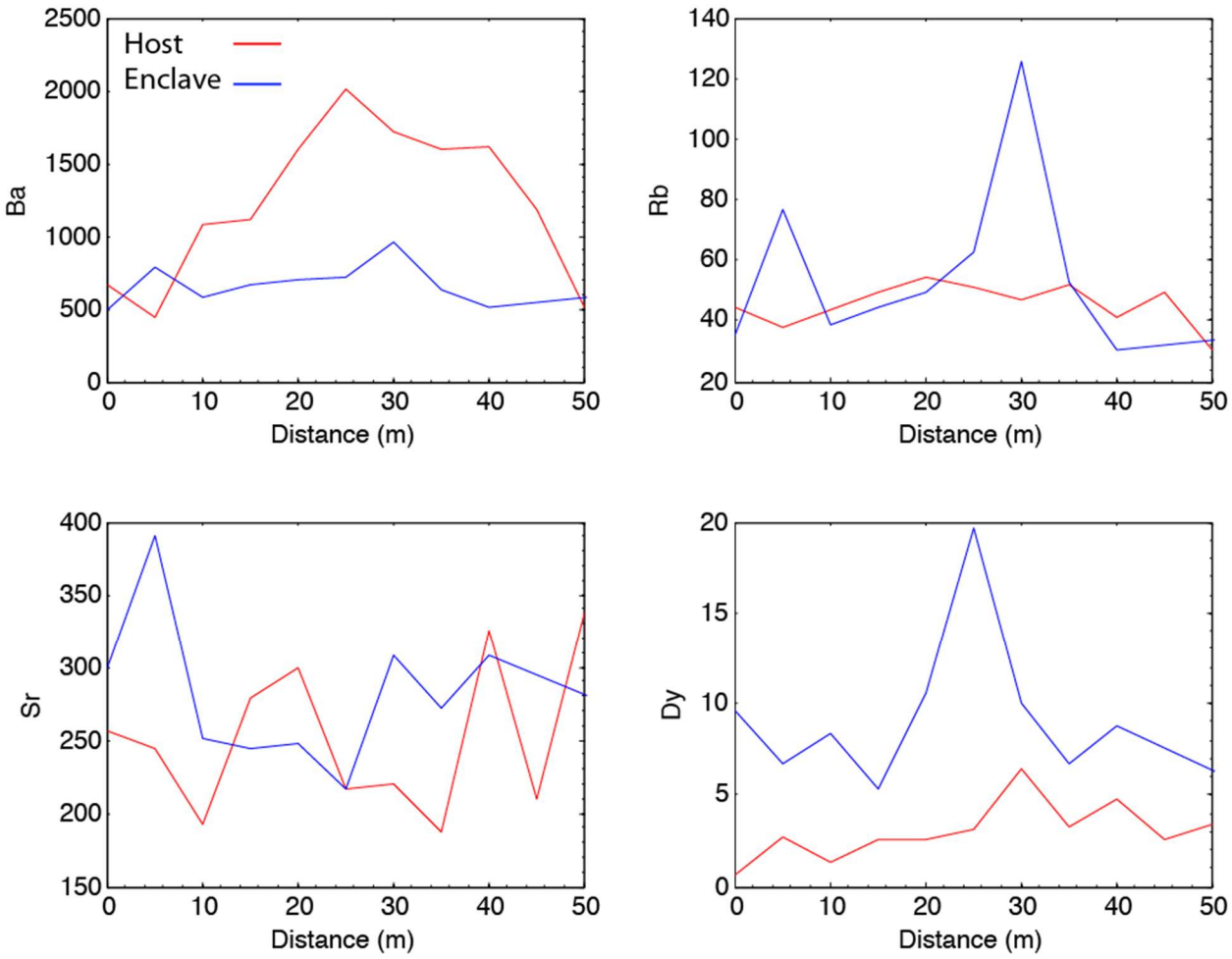

Figure 6.4. Geochemical section of selected trace elements along transect 1. Granitoids are shown in red and enclaves are in blue.

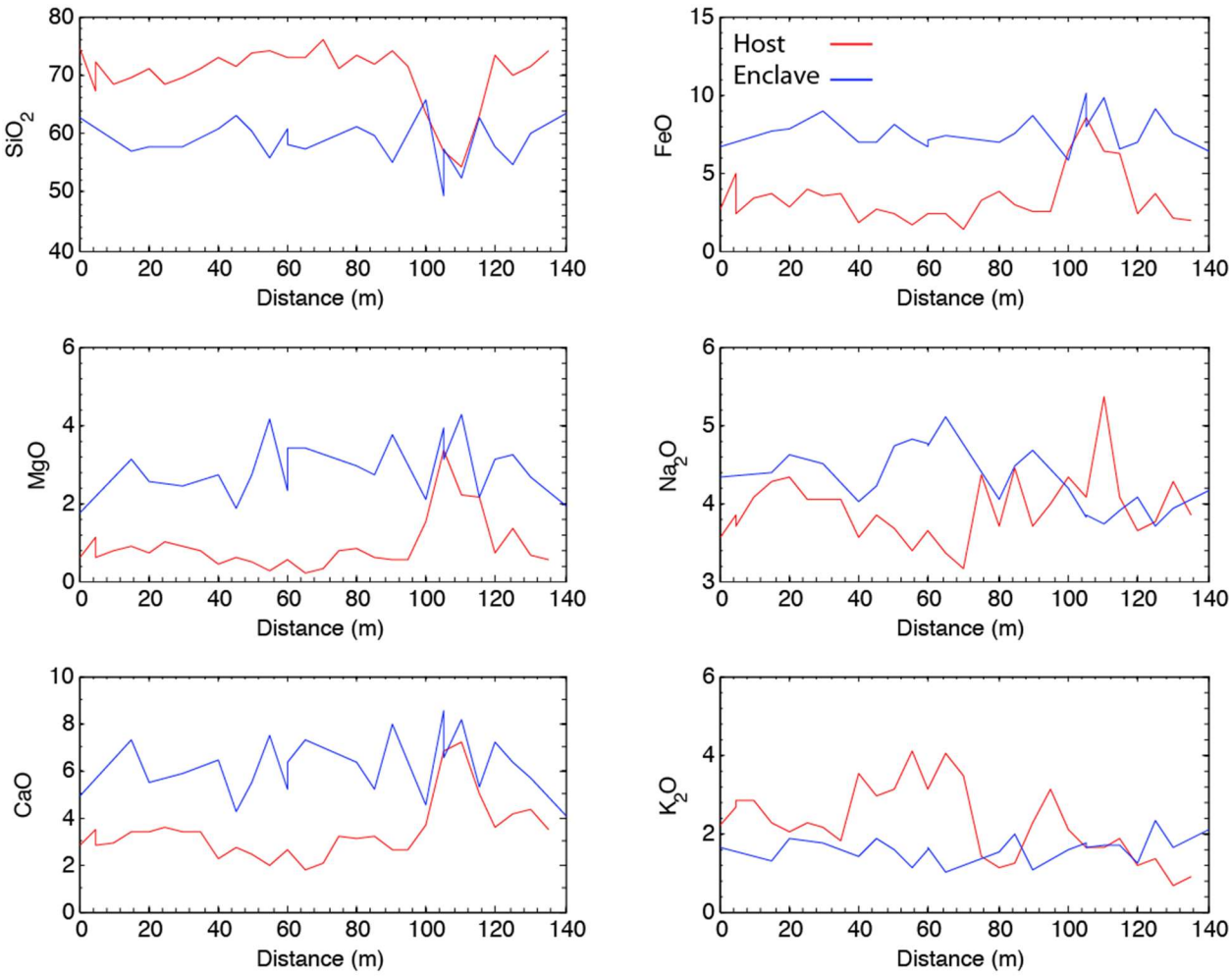

Figure 6.5. Major element geochemical sections corresponding to transect 2. Granitoids are shown in red and enclaves are in blue.

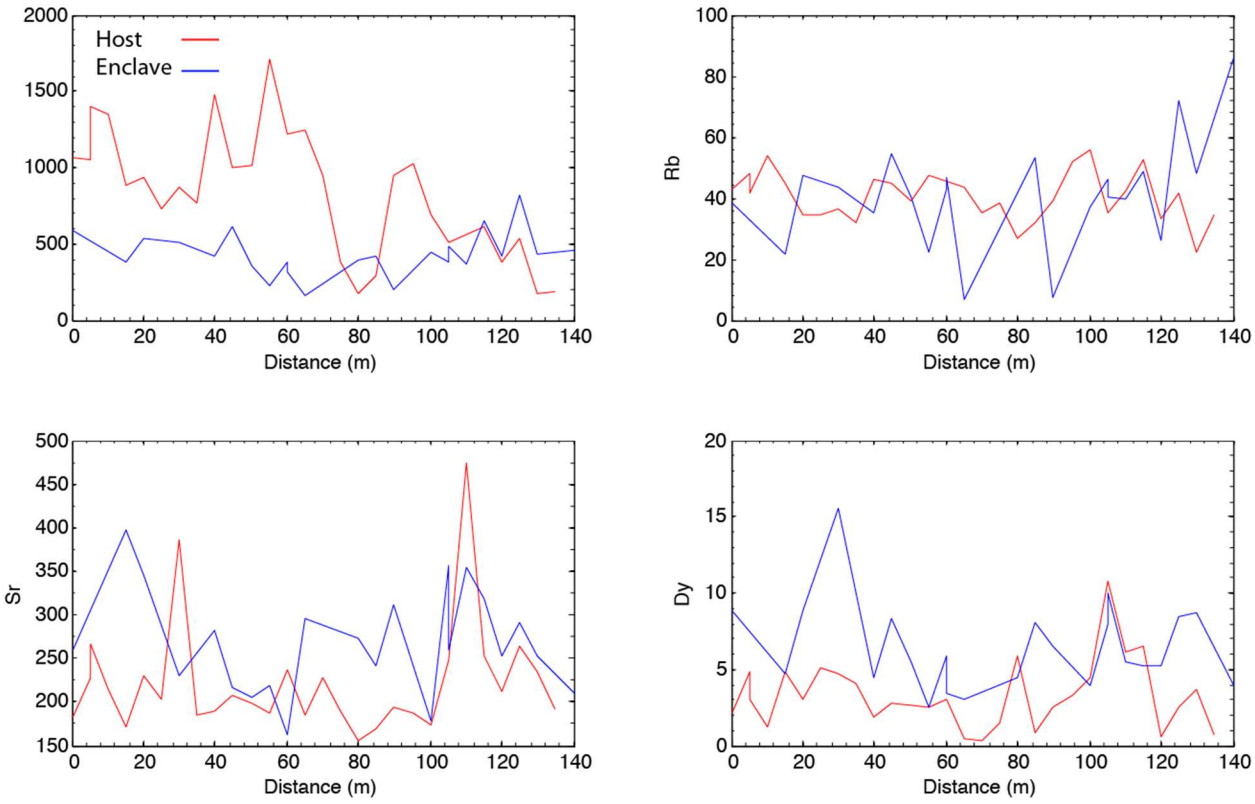

Figure 6.6. Geochemical sections of selected trace elements corresponding to transect 2. Granitoids are shown in red and enclaves are in blue.

6.5 Discussion

6.5.1 Comparing variations in enclave abundance and composition

We begin by comparing mapped enclaves with the variations in composition described above. Starting with transect 1, the most distinct variation in enclave composition occurs with the appearance of a mafic body between ~22-25 m and extends past the body into an enclave swarm at ~30 m. As shown in Figure 6.3, MgO, CaO, and FeO^* in the enclaves all increase over the width of the mafic body while SiO_2 decreases. By comparison, granitoid compositions do vary by more than a few wt. %, except for sodium and potassium, over this transect. Enclaves in this area are some of the most SiO_2-poor in the pluton (Figure 6.3), suggesting that they were likely mostly solidified upon intrusion into the pluton and did not interact with the host magma. It is

interesting to note that the observed spike in both sodium and potassium content occur near the margin of the enclave swarm at ~30 m. Given that biotite-rich rinds and schlieren are most abundant along the margins of swarms, this likely reflects elevated biotite and hornblende abundances. A similar alkali spike is also observed at ~5 m along the transect (Figure 6.3), co-incident with a mafic body containing biotite phenocrysts.

Enclaves are less densely concentrated along most of transect 2 compared to the first transect, except for the enclave swarm noted between ~95-110 m (Figure 6.2). Previous mapping (Morton, 2003) shows that this swarm cuts through the central portion of the pluton and continues outside of the quarry, near the climbing rock locality of Mason and Cohen (1990). Remarkably, enclaves and their host granitoids retain their distinct textural and mineralogical characteristics within this wide enclave swarm. The swarm is clearly identifiable in our geochemical dross sections by the close overlap of enclave and granitoid compositions (Figures 6.5 and 6.6). This was also noted in previous work on the swarm (Farner et al., submitted) and is thought to represent incipient magma mixing, where compositional smearing is observed between two petrographically distinct rocks. Collective, this indicates that enclaves were mostly solidified upon entrainment in the Bernasconi magma chamber and that mixing in the Bernasconi Hills pluton occurs locally, on the ~1 m scale.

6.5.2 Trace element systematics of enclaves and granitoids

We can further interrogate mapped lithologic variations using trace element systematics of the enclaves and host rocks. We focus here on the heavy rare earth elements as these show the greatest variation between granitoids and enclaves. As shown in Figure 6.7, granitoids exhibit a range of enrichment and depletion in trace elements relative to the bulk continental crust (BCC)

of Rudnick and Gao (2003), particularly with respect to the heavy rare earth elements. By comparison, nearly all sampled enclaves are enriched in HREEs relative to BCC. There is some compositional overlap between enclaves and host rocks within the large enclave swarm along transect 2. One probable reason that the enclaves are enriched in HREEs may be because they characteristically have much more hornblende than the granitoids and hornblende is the only abundant mineral phase observed in the pluton that HREEs are highly compatible in (Farner et al., 2014; Sisson, 1994). The composition of hornblende is highly variable and it is thus difficult to accurately model hornblende fractionation due to poor constraint on elemental partitioning. However, we can use our geological mapping in conjunction with compositional data as a proxy for hornblende variation in the pluton. To this end, we can use variation in Dy contents as a function of distance along sampling transects as an indirect proxy of hornblende content because although other HREEs work for mapping hornblende variations, Dy is one of the most compatible HREEs in hornblende. We find that the greatest Dy contents in enclave correspond to some of the most mafic enclave compositions, which in turn are manifested in the field by the coherent mafic body describe in transect 1 and the large enclave swarm described in transect 2.

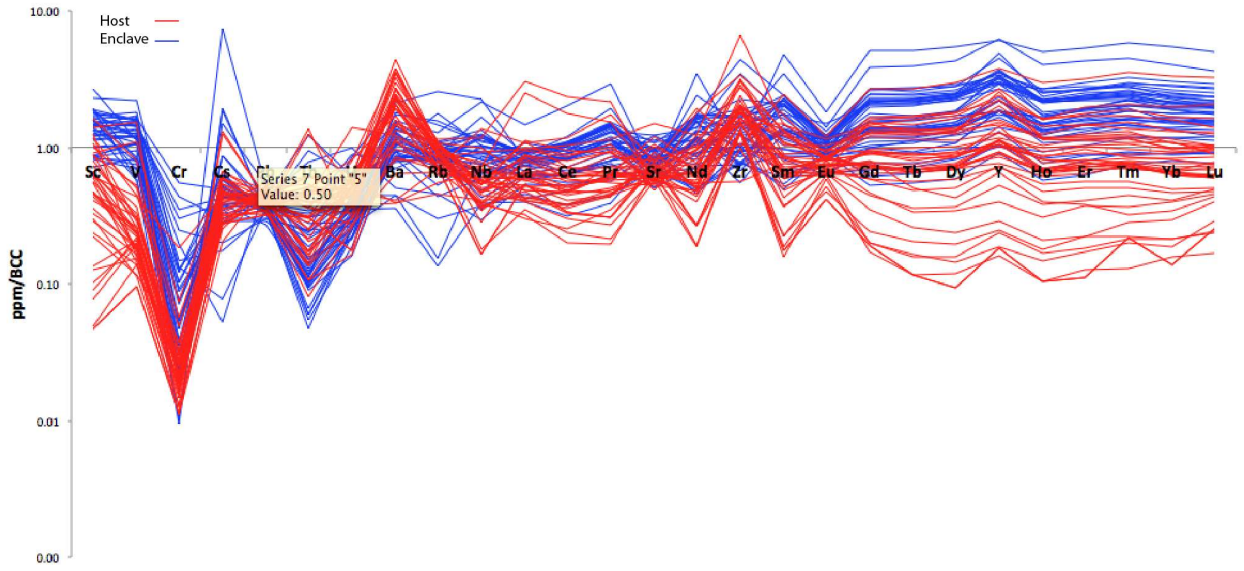

Figure 6.7. (above) Spidergram of trace element contents of host granitoids (red) and mafic enclaves (blue).

In a similar fashion, we can use other elements as indicators of specific mineral phases. For example, K_2O and Ba are both highly compatible in K-feldspar compared to other minerals present in Bernasconi Hills. As shown in Figures 6.X and 6.X, both elements co-vary and are enriched along the same portions of a given transect. In particular, we note are ~15 m wide zone along the second transect () where K_2O and Ba contents are elevated relative to adjacent sample segments. Previous work on the variation of K-feldspar abundance in the Bernasconi Hills pluton has identified this portion of the intrusion as one of the only areas that K-feldspar occurs (Chapter 5, this volume). Here, 1-2 mm long K-feldspar phenocrysts were described and hypothesized to represent evolved late-stage residual liquids that segregated from a plagioclase-quartz silicic cumulate.

The purpose in highlighting the use of specific elements for mapping mineralogical variations in tandem with geologic mapping is to demonstrate the utility in examining small scale variations in constraining broader magmatic processes. Here we have illustrated how such an approach can aid broader interpretations of an intrusion and corroborate previous interpretations, in particular the relationship of mafic enclaves to their host rocks.

6.6 Conclusion

This study presented geologic maps and corresponding geochemical sections through two transects of the Bernasconi Hills pluton in order to correlate lithologic variations observed in the field to geochemical variations in systematically collected samples corresponding to the mapped area. Using this approach, we are able to highlight and provide spatial constraint on incipient mixing between host granitoid rocks and enclaves within a large enclave swarm. Additionally,

we identify enrichments in the heavy rare earth content of enclaves relative bulk continental crust and host granitoids. Since hornblende is the only abundant phase in the pluton where HREEs are highly compatible, we are able to use variations in Dy content in enclaves as an indirect proxy for mapping hornblende content. We further illustrate the use of highly compatible trace elements with Ba to corroborate the occurrence of K-feldspar in granitic host rocks, as constrained from previous work.

References

Ague, J.J., Brimhall, G.H., 1988. Magmatic arc asymmetry and distribution of anomalous plutonic belts in the batholiths of California: effects of assimilation, crustal thickness, and depth of crystallization. Geological Society of America Bulletin 100, 912-927.
Alonso-Perez, R., Muntener, O., Ulmer, P., 2008. Igneous garnet and amphibole fractionation in the roots of island arcs: experimental constraints on andesitic melts. Contributions to Mineralogy and Petrology 157, 541-558.
Anderson, A.T.J., Swihart, G.H., Artioli, G., Geiger, C.A., 1984. Segregation vesicles, gas filter-pressing, and igneous differentiation. Journal of Geology 92, 55-72.
Arndt, N.T., Goldstein, S.L., 1989. An open boundary between lower continental crust and mantle: its role in crust formation and crustal recycling. Tectonophysics 161, 201-212.
Arth, J.G., 1976. Behavior of trace elements during magmatic processes - a summary of theoretical models and their applications. Journal of Research of U.S. Geological Survey 4, 41-47.
Asimow, P.D., Ghiorso, M.S., 1998. Algorithmic modifications extending MELTS to calculate subsolidus phase relations. American Mineralogist 83, 1127-1131.
Bachmann, O., Bergantz, G.W., 2004. On the origin of crystal-poor rhyolite: extracted from batholithic crystal mushes. Journal of Petrology 45, 1565-1582.
Bachmann, O., Deering, C.D., Lipman, P.W., Plummer, C., 2014. Building zoned ignimbrites by recycling silicic cumulates: insight from the 1000 km3 Carpenter Ridge Tuff, CO. Contributions to Mineralogy and Petrology 167.
Bachmann, O., Dungan, M.A., Lipman, P.W., 2002. The Fish Canyon magma body, San Juan Volcanic Field, Colorado: rejuvenation and eruption of an upper-crustal batholith. Journal of Petrology 43, 1469-1503.
Bacon, C.R., 1986. Magmatic inclusions in silicic and intermediate volcanic rocks. Journal of Geophysical Research 91, 6091-6112.
Baird, A.K., Baird, K.W., Welday, E.E., 1979. Batholithic rocks of the northern Peninsular and Transverse Ranges, southern California: chemical compositions and variation, in: Abot, P.L., Todd, V.R. (Ed.), Mesozoic Crystalline Rocks: Peninsular Range Batholith and Pegmatites, Point Sal Ophiolite. Dept of Geological Sciences, San Diego State University, San Diego, pp. 111-132.
Balducci, S., Leoni, L., 1981. Sanidine phenocrysts from M. Amaita trachytes and Roccastrada rhyolites. Neues Jahrbuch fur Mineralogie 143, 15-36.
Barbarin, B., 2005. Mafic magmatic enclaves and mafic rocks associated with some granitoids of the central Sierra Nevada batholith, California: nature, origin, and relations with the hosts. Lithos 80, 155-177.
Bateman, P.C., 1992. Plutonism in the central part of the Sierra Nevada batholith, California.
Bateman, P.C., Chappell, B.W., Kistler, R.W., Peck, D.L., Busacca, A., 1988. Tuolumne Meadows Quadrangle, California - analytic data, in: Survey, U.S.G. (Ed.), p. 52.
Bea, F., Pereira, M.D., Stroh, A., 1994. Mineral/leucosome trace element partitioning in a peraluminous migmatite (a laster ablation-ICP-MS study). Chemical Geology 117, 291-312.
Beard, J.S., Ragland, P.C., Crawford, M.L., 2005. Reactive bulk assimilation: amodel for crust-mantle mixing in silicic magmas. Geology 33, 681-684.

Bishop, A.C., 1963. Dark margins at igneous contacts: a critical study with reference to those in Jersey, C.I. Proceedings of the Geological Association 74, 289-300.
Blake, D.H., Elwell, R.W.D., Gibson, I.L., Skelhorn, R.R., Walker, G.P.L., 1965. Some relationships resulting from the intimate association of acid and basic magmas. Journal of the Geological Society of London 121, 31-49.
Brounce, M.N., Kelley, K.A., Cottrell, E., 2014. Variations in Fe3+/∑Fe of Mariana arc basalts and mantle wedge fO2. Journal of Petrology 55, 2513-2536.
Busby, C., 2004. Continental growth at convergent margins facing large ocean basins: a case study from Mesozoic convergent-margin basins of Baja California, Mexico. Tectonophysics 392, 241-277.
Busby, C., Hagan, J.C., Putirka, K.D., Pluhar, C.J., Gans, P.B., Wagner, D.L., Rood, D., DeOreo, S.B., Skilling, I., 2008. The ancestral Cascades Arc; Cenozoic evolution of the central Sierra Nevada (California) and the birth of the new plate boundary., Geological Society of America Special Volume, pp. 331-378.
Carslaw, H.S., Jaeger, J.C., 1959. Conduction of heat in solids. Clarendon Press, Oxford.
Chapman, C.A., 1962. Diabase-granite composite dikes, with pillow-like structure, Mount Desert Island, Maine. Journal of Geology 70, 539-564.
Chapman, J.B., Ducea, M.N., DeCelles, P.G., Profleta, L., 2015. Tracking changes in crustal thickness during Orogenic evolution with Sr/Y: an example from the North American Cordillera. Geology 43, 919-922.
Cherniak, D.J., 2010. Cation diffusion in feldspars, in: Zhang, Y., Cherniak, D.J. (Ed.), Diffusion in minerals in melts, pp. 691-733.
Chiardia, M., 2015. Crustal thickness control on Sr/Y signatures of recent arc magmas: an Earth scale perspective. Scientific Reports 5.
Chin, E.J., Lee, C.-T.A., Barnes, J.D., 2014. Thickening, refertilization, and the deep lithospheric filter in continental arcs: constraints from major and trace elements and oxygen isotopes. Earth and Planetary Science Letters 397, 184-200.
Clavero, J.E., Sparks, R.S.J., Pringle, M.S., Polanco, E., Gardeweg, M.C., 2004. Evolution and volcanic hazards of Taapaca Volcanic Complex, central Andes of northern Chile. Journal of the Geological Society 161, 603-618.
Clynne, M.A., 1999. A complex magma mixing origin for rocks erupted in 1915, Lassen Peak, California. Journal of Petrology 40, 105-132.
Coleman, D.S., Gray, W., Glazner, A.F., 2004. Rethinking the emplacement and evolution of zoned plutons: geochronologic evidence for incremental assembly of the Tuolumne Intrusive Suite, California. Geology 32, 433-436.
Cooper, K.M., Kent, A.J.R., 2014. Rapid remobilization of magmatic crystals kept in cold storage. Nature 506, 480-487.
Cox, R.A., Dempster, T.J., Bell, B.R., Rogers, G., 1996. Crystallization of the Shap Granite: evidence from zoned K-feldspar megacrysts. Journal of the Geological Society 153, 625-635.
Davidson, J.P., Dungan, M., Ferguson, K.M., Colucci, M.T., 1987. Crust-magma interactions and the evolution of arc magmas: the San Pedro-Pellado volcanic complex, southern Chilean Andes. Geology 15, 443-446.
DeBari, S.M., Sleep, N.H., 1991. High-Mg, low-Al bulk composition of the Talkeetna island arc, Alaska: implications for primary magmas and the nature of arc crust. Geological Society of America Bulletin 103, 37-47.
Deer, W.A., Howie, R.A., Zussman, J., 1992. The rock-forming minerals, 2 ed. Pearson.

DePaolo, D.J., 1981. A neodymium and strontium isotopic study of the Mesozoic calc-alkaline granitic batholiths of the Sierra Nevada and Peninsular Ranges, California. Journal of Geophysical Research 86, 10470-10488.
Dhuime, B., Wuestefeld, A., Hawkesworth, C.J., 2015. Emergence of meodern continental crust about 3 billion years ago. Nature Geoscience 8, 552-554.
Didier, J., 1973. Granites and their enclaves. Elsevier, Amsterdam.
Ducea, M.N., Saleeby, J.B., 1998. The age and origin of a thick mafic-ultramafic keel from beneath the Sierra Nevada batholith. Earth and Planetary Science Letters 90, 26-40.
Dungan, M., Wulff, A., Thompson, R., 2001. Eruptive stratigraphy of the Tatara-San Pedro Complex, 36°S, southern volcanic zone, Chilean Andes: reconstruction method and implications for magma evolution at long-lived arc volcanic centers. Journal of Petrology 42, 555-626.
Eberz, G.W., Nicholls, I.A., 1990. Chemical modification of enclave magma by post-emplacement crystal fractionation, diffusion and metasomatism. Contributions to Mineralogy and Petrology 104, 47-55.
Eichelberger, J.C., 1975. Origin of andesite and dacite: evidence of mixing at Glass Mountain in California and at other circum-Pacific volcanoes. Geological Society of America Bulletin 86, 1381-1391.
Eichelberger, J.C., Izbekov, P.E., Browne, B.L., 2006. Bulk chemical trends at arc volcanoes are not liquid lines of descent. Lithos 87, 135-154.
Erdman, M.E., Lee, C.-T.A., Levander, A., Jiang, H., 2016. Role of arc magmatism and lower crustal foundering in controlling elevation history of the Nevadaplano and Colorado Plateau: a case study of pyroxenitic lower crust from central Arizon, USA. Earth and Planetary Science Letters 439, 48-57.
Esperanca, S., Carlson, R.W., Shirey, S.B., 1988. Lower crustal evolution under central Arizona: Sr, Nd and Pb isotopic and geochemical evidence from the mafic xenoliths of Camp Creek. Earth and Planetary Science Letters 90, 26-40.
Farner, M.J., Lee, C.-T.A., Mikus, M.L., submitted. Examining the field and geochemcial characteristics of incipient mafic-felsic magma mixing and implications for making intermediate magmas: a case study of the Bernasconi Hills pluton, California.
Farner, M.J., Lee, C.-T.A., Putirka, K.D., 2014. Mafic-felsic magma mixing limited by reactive processes: a case study of biotite-rich rinds on mafic enclaves. Earth and Planetary Science Letters 393, 49-59.
Frost, T.P., Mahood, G.A., 1987. Field, chemical, and physical constraints on mafic-felsic magma interaction in the Lamarck Granodiorite, Sierra Nevada, California. Geological Society of America Bulletin 99, 272-291.
Fujimaki, H., Tatsumoto, M., Aoki, K.-I., 1984. Partition coefficients of Hf, Zr, and REE between phenocrysts and groundmasses. Journal of Geophysical Research 89, B662-B672.
Furman, T., Spera, F.J., 1985. Co-mingling of acid and basic magma with implications for the origin of mafic I-type xenoliths: field and petrochemical relations of an unusual dike complex at Eagle Lake, Sequoia National Park, California, USA. Journal of Volcanology and Geothermal Research 24, 151-178.
Gaetani, G.A., 2016. The behavior of $Fe^{3+}/\sum Fe$ during partial melting of spinel lherzolite. Geochimica et Cosmochimica Acta 185, 64-77.
Gastil, R.G., 1975. Plutonic zones in the Peninsular Ranges of southern California and northern Baja California. Geology 3, 361-363.

Gastil, R.G., Morgan, G., Krummenacher, D., 1988. The tectonic development of Peninsular California and adjacent Mexico, in: Ernst, W.G. (Ed.), The geotectonic development of California. Prentice Hall, Englewood Cliffs, NJ, pp. 285-306.
Ghiorso, M.S., Gualda, G.A.R., 2015. An H2O-CO2 mixing fluid saturation model compatible with rhyolite-MELTS. Contributions to Mineralogy and Petrology 169, 1-30.
Ghiorso, M.S., Sack, R.O., 1995. Chemical mass transfer in magmatic processes IV: A revised and internally consistent thermodynamic model for the interpolation or extrapolation of liquid-solid equilibria in magmatic systems at elevated temperatures and pressures. Contributions to Mineralogy and Petrology 119, 197-212.
Glazner, A.F., Johnson, B.R., 2013. Late crystallization of K-feldspar and the paradox of megacrystic granites. Contributions to Mineralogy and Petrology 166, 777-799.
Green, T.H., Blundy, J.D., Adam, J., Yaxley, G.M., 2000. SIMS determination of trace element partition coefficients between garnet, clinopyroxene and hydrous basaltic melts at 2-7.5 GPa and 1080-1200°C. Lithos 53, 165-187.
Greene, A.R., DeBari, S.M., Kelemen, P.B., Blusztajn, J., Clift, P.D., 2006. A detailed geochemical study of island arc crust: the Talkeetna arc section, south-central Alaska. Journal of Petrology 47, 1051-1093.
Gromet, P., Silver, L.T., 1987. REE variations across the Peninsular Ranges Batholith: implications for batholithic petrogenesis and crustal growth in magmatic arcs. Journal of Petrology 28, 75-125.
Grove, T.L., Till, C.B., Krawczynski, M.J., 2012. The role of H2O in subduction zone magmatism. Annual Reviews in Earth and Planetary Sciences 40, 413-439.
Gualda, G.A.R., Ghiorso, M.S., Lemons, R.V., Carley, T.L., 2012. Rhyolite-MELTS: a modified calibration of MELTS optimized for silica-rich, fluid-bearing magmatic systems. Journal of Petrology 53, 875-890.
Harrison, T.M., Watson, E.B., 1984. The behavior of apatite during crustal anatexis: equilibrium and kinetic considerations. Geochimica et Cosmochimica Acta 48, 1467-1477.
Hauri, E.H., Wagner, T.P., Grove, T.L., 1994. Experimental and natural partitioning of Th, U, Pb and other trace elements between garnet, clinopyroxene and basaltic melts. Chemical Geology 117, 149-166.
Herzberg, C., Rudnick, R.L., 2012. Formation of cratonic lithosphere: an integrated thermal and petrological model. Lithos 149, 4-15.
Hildreth, W., Moorbath, S., 1988. Crustal contributions to arc magmatism in the Andes of central Chile. Contributions to Mineralogy and Petrology 98, 455-489.
Hirt, W.H., 1989. The petrological and mineralogical zonation of the Mount Whitney intrusive suite, eastern Sierra Nevada, California. University of California, Santa Barbara, p. 470.
Hodge, K.F., Jellinek, A.M., 2012. Linking enclave formation to magma rheology. Journal of Geophysical Research 117, B10208.
Holtz, F., Pichavant, M., Barbey, P., Johannes, W., 1992. Effects of H2O on liquidus phase relations in the haplogranite system at 2 and 5 kbar. American Mineralogist 77, 1223-1241.
Huang, W.-L., Wyllie, P.J., 1975. Melting relations in the system $NaAlSi_3O_8$-$KAlSi_3O_8$-SiO_2 to 35 kilobars, dry and with excess water. Journal of Geology 83, 737-748.
Huber, C., Bachmann, O., Dufek, J., 2010. The limitations of melting on the reactivation of silicic mushes. Journal of Volcanology and Geothermal Research 195, 97-105.

Huber, C., Bachmann, O., Manga, M., 2009. Homogenization processes in silicic magma chambers by stirring and mushification (latent heat buffering). Earth and Planetary Science Letters 283, 38-47.
Jagoutz, O.E., 2010. Construction of the granitoid crust of an island arc part II: a quantitative petrogenetic model. Contributions to Mineralogy and Petrology 160, 359-381.
Jagoutz, O.E., 2014. Arc crustal differentiation mechanisms. Earth and Planetary Science Letters 396, 267-277.
Jagoutz, O.E., Burg, J.-P., Hussain, S., Dawood, H., Pettke, T., Iizuka, T., Maruyama, S., 2009. Construction of the granitoid crust of an island arc part I: geochronological and geochemical constraints from the plutonic Kohistan (NW Pakistan). Contributions to Mineralogy and Petrology 158, 739-755.
Jagoutz, O.E., Schmidt, M.W., 2012. The formation and bulk composition of modern juvenile continental crust: the Kohistan arc. Chemical Geology 298-299, 79-96.
Jiang, H., Lee, C.-T.A., Morgan, J.K., Ross, C.H., 2015. Geochemistry and thermodynamics of an earthquake: a case study of pseudotachylites within mylonitic granitoid. Earth and Planetary Science Letters 430, 235-248.
Johannes, W., Holtz, F., 1996. Petrogenesis and experimental petrology of granitic rocks. Springer-Verlag.
Johnson, B.R., Glazner, A.F., 2010. Formation of K-feldspar megacrysts in granodioritic plutons by thermal cycling and late-stage textural coursening. Contributions to Mineralogy and Petrology 159, 599-619.
Johnson, D.M., Hooper, P.R., Conrey, R.M., 1999. XRF analysis of rocks and minerals for major and trace elements on a single low dilution Li-tetroborate fused bead. Advances in X-ray Analysis 41, 843-867.
Johnson, M., Rutherford, M.J., 1986. Experimentally determined conditions in the Fish Canyon Tuff, Colorado, magma chamber. Journal of Petrology 30, 711-737.
Karlstrom, L., Lee, C.-T.A., Manga, M., 2014. The role of magmatically driven lithospheric thickening on arc front migration. Geochemistry, Geophysics, Geosystems 15, 2655-2675.
Kelemen, P.B., 1995. Genesis of high Mg # andesites and the continental crust. Contributions to Mineralogy and Petrology 120, 1-19.
Keller, C.B., Schoene, B., Barboni, M., Samperton, K.M., Husson, J.M., 2015. Volcanic-plutonic parity and the differentiation of the continental crust. Nature 523.
Kelley, K.A., Cottrell, E., 2009. Water and the oxidation state of subduction zone magmas. Science 325, 605-607.
Kent, A.J.R., Darr, C., Koleszar, A.M., Salisbury, M.J., Cooper, K.M., 2010. Preferential eruption of andesitic magmas through recharge filtering. Nature Geoscience 3, 631-636.
Kerrick, D.M., 1969. K-feldspar megacrysts from a porphyritic quartz monzonite central Sierra Nevada, California. American Mineralogist 54, 839-848.
Kistler, R.W., Wooden, J.L., Morton, D.M., 2003. Isotopes and ages in the northern Peninsular Ranges Batholith, southern California. USGS Open-file report 03-489, 1-45.
Kistler, R.W., Wooden, J.L., Premo, W.R., Morton, D.M., 2014. Pb-Sr-Nd-O isotopic characterization of Mesozoic rocks throughout the northern end of the Peninsular Ranges Batholith: isotopic evidence for the magmatic evolution of oceanic arc-continental margin accretion during the Late Cretaceous of southern California, in: Morton, D.M., Miller, F.K. (Ed.), Peninsular Ranges Batholith, Baja California and southern California. Geological Society of America.

Laske, G., Masters, G., Ma, Z., Pasyanos, M., 2013. Update on CRUST1.0 - a 1-degree global model of Earth's crust. Geophysical Research Abstracts EGU2013-2658.
Lee, C.-T.A., 2014. Physics and chemistry of deep continental crust recycling, in: Holland, H., Turekian, K. (Eds.), Treatise of Geochemistry, 2 ed. Elsevier, pp. 423-456.
Lee, C.-T.A., Bachmann, O., 2014. How important is the role of crystal fractionation in making intermediate magmas? Insights from Zr and P systematics. Earth and Planetary Science Letters 393, 266-274.
Lee, C.-T.A., Cheng, X., Horodyskyj, U., 2006. The development and refinement of continental arcs by primary basaltic magmatism, garnet pyroxenite accumulation, basaltic recharge and delamination: insights from the Sierra Nevada, California. Contributions to Mineralogy and Petrology 151, 222-242.
Lee, C.-T.A., Lee, T.C., Wu, C.-T., 2014. Modeling the compositional evolution of recharging, evacuating, and fractionating (REFC) magma chamber: implications for differentiation of arc magmas. Geochimica et Cosmochimica Acta 143, 8-22.
Lee, C.-T.A., Leeman, W.P., Canil, D., Li, Z.-X.A., 2005. Similar V/Sc systematics in MORB and arc basalts: implications for the oxygen fugacities of their mantle source regions. Journal of Petrology 46, 2313-2336.
Lee, C.-T.A., Luffi, P., Chin, E.J., Bouchet, R., Dasgupta, R., Morton, D.M., Le Roux, V., Yin, Q.-z., Jin, D., 2012. Copper systematics in arc magmas and implications for crust-mantle differentiation. Science 336, 64-68.
Lee, C.-T.A., Luffi, P., V., L.R., Dasgupta, R., Albarède, F., Leeman, W.P., 2010. The redox state of arc mantle using Zn/Fe systematics. Nature 468, 681-685.
Lee, C.-T.A., Morton, D.M., 2015. High silica granites: terminal porosity and crystal settling in shallow magma chambers. Earth and Planetary Science Letters 409, 23-31.
Lee, C.-T.A., Morton, D.M., Farner, M.J., Moitra, P., 2015a. Field and model constraints on silicic melt segregation by compaction/hindered settling: the role of water and its effect on latent heat release. American Mineralogist 100, 1762-1777.
Lee, C.-T.A., Morton, D.M., Kistler, R.W., Baird, A.K., 2007. Petrology and tectonics of Phanerozoic continent formation: from island arcs to accretion and continental arc magmatism. Earth and Planetary Science Letters 263, 370-387.
Lee, C.-T.A., Thurner, S., Paterson, S., Cao, W., 2015b. The rise and fall of contienntal arcs: interplays between magmatism, uplift, weathering, and climate. Earth and Planetary Science Letters 425, 105-119.
Liao, K.Z., Morton, D.M., Lee, C.-T.A., 2013. Geochemical diagnostics of metasedimentary dark enclaves: a case study from the Peninsular Ranges Batholith, southern California. International Geology Review 55, 1049-1072.
Luth, W.C., 1969. The systems $NaAlSi_3O_8$-SiO_2 and $KAlSi_3O_8$-SiO_2 to 20 kb and the relationship between H_2O-content, P_{H2O}, and P_{total} in granitic magmas. American Journal of Science 267, 325-341.
Mallmann, G., O'Neill, H.S.C., 2009. The crystal/melt partitioning of V during mantle melting as a function of oxygen fugacity compared with some other elements (Al, P, Ca, Sc, Ti, Cr, Fe, Ga, Y, Zr and Nb). Journal of Petrology 50, 1765-1794.
Mantle, G.W., Collins, W.J., 2008. Quantifying crystal thickness variations in evolving orogens: correlation between arc basalt compositions and Moho depth. Geology 36, 87-90.
Marsh, B.D., 1981. On the crystallinity, probability of occurance, and rheology of lava and magma. Contributions to Mineralogy and Petrology 78, 85-98.

Mason, D.R., Cohen, L.H., 1990. Field, mineralogical and microtextural relationships between mafic enclaves, and host granitoids in the Bernasconi Pluton, Peninsular Ranges batholith, southern California, USA, in: Parker, A.J., Rickwood, P.C., Tucker, D.H. (Eds.), Mafic Dykes and Emplacement Mechanisms. Balkema, Rotterdam.
Matzel, J.E.P., Bowring, S.A., Miller, R.B., 2006. Timescales of pluton construction at differeing crustal levels: examples from the Mount Stuart and Tenpeak intrusions, North Cascades, Washington. Geological Society of America Bulletin 118, 1412-1430.
Miller, C.F., McDowell, S.M., Mapes, R.W., 2003. Hot and cold granites? Implications of zircon saturation temperatures and preservation of inheritance. Geology 31, 529-532.
Moore, J.G., Sisson, T.W., 2008. Igneous phenocrystic origin of K-feldspar megacrysts in granitic rocks from the Sierra Nevada batholith. Geosphere 4, 387-400.
Morton, D.M., 1969. The Lakeview Mountains pluton, southern California batholith. Part I: Petrology and structure. Geological Society of America Bulletin 80, 1539-1552.
Morton, D.M., 2003. Preliminary geologic map of the Perris quadrangle, Riverside County, California. United States Geological Survey.
Morton, D.M., Miller, F.K., Kistler, R.W., Premo, W.R., Lee, C.-T.A., Langenheim, V.E., Wooden, J.L., Snee, L.W., Clausen, B.L., Cossette, P., 2014. Framework and petrogenesis of the northern Peninsular Ranges Batholith, southern California, in: Morton, D.M., Miller, F.K. (Ed.), Peninsular Ranges Batholith, Baja California and southern California. Geological Society of America, Boulder, pp. 61-143.
Nash, W.P., Crecraft, H.R., 1985. Partition coefficients for trace elements in silicic magmas. Geochimica et Cosmochimica Acta 49, 2309-2322.
O'Neill, H.S.C., Jenner, F.E., 2012. The global pattern of trace element distributions in ocean floor basalts. Nature 491, 698-705.
Pabst, A., 1928. Observations on inclusions in the granitic rocks of the Sierra Nevada. University of California Publications Geological Sciences 17, 325-386.
Paterson, S.R., Pignotta, G.S., Vernon, R.H., 2004. THe significance of microgranitoid enclave shapes and orientations. Journal of Structural Geology 26, 1465-1481.
Patino Douce, A.E., Harris, N., 1998. Experimental constraints on Himalayan anatexis. Journal of Petrology 39, 689-710.
Patiño Douce, A.E., Johnston, A.D., 1991. Phase equilibria and melt productivity in the pelitic system: implications for the origin of peraluminous granitoids and aluminous granulites. Contributions to Mineralogy and Petrology 107, 202-218.
Plank, T., 2005. Constraints from Thorium/Lanthanum on sediment recycling at subduction zones and the evolution of the continents. Journal of Petrology 46, 921-944.
Plank, T., Kelley, K.A., Zimmer, M.M., Hauri, E.H., Wallace, P.J., 2013. Why do mafic arc magmas contain ~4 wt% water on average? Earth and Planetary Science Letters 364, 168-179.
Plank, T., Langmuir, C.H., 1988. An evaluation of the global variations in the major elements chemistry of arc basalts. Earth and Planetary Science Letters 90, 349-370.
Premo, W.R., Morton, D.M., Wooden, J.L., Fanning, C.M., 2014. U-Pb zircon geochronology of plutonism in the northern Peninsular Ranges Batholith, southern California: implications for the Late Cretaceous tectonic evolution of southern California, in: Morton, D.M., Miller, F.K. (Ed.), Peninsular Ranges Batholith, Baja California and southern California, pp. 145-180.

Ratajeski, K., Glazner, A.F., Miller, B.V., 2001. Geology and geochemistry of mafic to felsic plutonic rocks in the Cretaceous intrusive suite of Yosemite Valley, California. Geological Society of America Bulletin 113, 1486-1502.
Reid, J.B., Evans, O.C., Fates, D.G., 1983. Magma mixing in granitic rocks of the central Sierra Nevada, California. Earth and Planetary Science Letters 66, 243-261.
Reubi, O., Blundy, J.D., 2009. A dearth of intermediate melts at subduction zone volcanoes and the petrogenesis of arc andesites. Nature 461, 1269-1274.
Rudnick, R.L., 1995. Making continental crust. Nature 378, 571-578.
Rudnick, R.L., Fountain, D.M., 1995. Nature and composition of the continental crust: a lower crustal perspective. Reviews of Geophysics 33, 267-309.
Rudnick, R.L., Gao, S., 2003. Composition of the continental crust. Elsevier-Pergamon, Oxford.
Ruprecht, P., Wörner, G., 2007. Variable regimes in magma systems documented in plagioclase zoning patterns: El Misti stratovolcano and Andahua monogenetic cones. Journal of Volcanology and Geothermal Research 165, 142-162.
Sisson, T.W., 1994. Hornblende-melts trace element partitioning measured by ion microprobe. Chemical Geology 117, 331-344.
Sisson, T.W., Bacon, C.R., 1999. Gas-driven filter pressing in magmas. Geology 27, 613-616.
Sisson, T.W., Grove, T.L., 1993. Experimental investigations of the role of H2O in calc-alkaline differentiation and subduction zone magmatism. Contributions to Mineralogy and Petrology 113, 143-166.
Sisson, T.W., Grove, T.L., Coleman, D.S., 1996. Hornblende gabbro sill complex at Onion Valley, California and a mixing origin for the Sierra Nevada batholith. Contributions to Mineralogy and Petrology 126, 81-108.
Snyder, D., Tait, S., 1995. Replenishment of magma chambers: comparison of fluid-mechanic experiments with field relations. Contributions to Mineralogy and Petrology 122, 230-240.
Sparks, R.S.J., Marshall, L.A., 1986. Thermal and mechanical constraints on mixing between mafic and silicic magmas. Journal of Volcanology and Geothermal Research 29, 99-124.
Spear, F.S., 1995. Metamorphic phase equilibria and pressure-temperature-time paths. Mineralogical Society of America, Washington, D.C.
Steven, T.A., Ratte, J.C., 1960. Geology and ore deposits of the Summitville district, San Juan Mountains, Colorado. Geological Survey Professional Paper 343.
Stimac, J.A., Clark, A.H., Chen, Y., Garcia, S., 1995. Enclaves and their bearing on the origin of the Cornubian batholith, southwest England. Mineralogical Magazine 59, 273-296.
Swanson, S.E., 1977. Relation of nucleation and crystal-growth rate to the development of granitic textures. American Mineralogist 62, 966-978.
Tepley, F.J., Davidson, J.P., Clynne, M.A., 1999. Magmatic interactions as recorded in plagioclase phenocrysts of Chaos Crags, Lassen Volcanic Center, California. Journal of Petrology 40, 787-806.
Todd, V.R., Erskine, B.G., Morton, D.M., 1988. Metamorphic and tectonic evolution of the Peninsular Ranges batholith, in: Ernst, W.G. (Ed.), Metamorphism and crustal evolution of the western United States. Prentice Hall, Englewood Cliffs, NJ, pp. 894-937.
Todd, V.R., Shaw, S.E., 1985. S-type granitoids and an I-S line in the Peninsular Ranges Batholith, southern California. Geology 13, 231-233.

Turner, S.J., Langmuir, C.H., 2015a. The global chemical systematics of arc front stratovolcanoes: evaluating the role of crustal processes. Earth and Planetary Science Letters 422, 182-193.
Turner, S.J., Langmuir, C.H., 2015b. What processes control the chemical composition of arc front stratovolcanoes? Geochemistry, Geophysics, Geosystems 16, 1865-1893.
Tuttle, O.F., Bowen, N.L., 1958. Origin of granite in light of experimental studies in the system $NaAlSi_3O_8$-$KAlSi_3O_8$-SiO_2-H_2O. Geological Society of America, Baltimore.
Vernon, R.H., 1984. Microgranitoid enclaves in granites-globules of hybrid magmaquenched in a plutonic environment. Nature 309, 438-439.
Vernon, R.H., 1986. K-feldspar megacrysts in granites - phenocrysts, not porphyroblasts. Earth Science Reviews 23, 1-63.
Vernon, R.H., 1990. Crystallization and hybridism in microgranitoid enclave magmas: microstructural evidence. Journal of Geophysical Research 95, 17849-17859.
Vernon, R.H., Paterson, S.R., 2008. How late are K-feldspar megacrysts in granites? Lithos 104, 327-336.
Vielzeuf, D., Holloway, J.R., 1988. Experimental determination of the fluid-absent melting relations in the pelitic system: consequences for crustal differentiation. Contributions to Mineralogy and Petrology 98, 257-276.
Wager, L.R., Bailey, E.B., 1953. Basic magma chilled against acid magma. Nature 172, 68-69.
Walker, G.P.L., Skelhorn, R.R., 1966. Some associations of acid and basic igneous rocks. Earth Science Reviews 2, 93-109.
Watson, E.B., Harrison, T.M., 1983. Zircon saturation revisited: temperature and composition effects in a variety of crustal magma types. Earth and Planetary Science Letters 64, 295-304.
Wetmore, P.H., Herzig, C., Alsleben, H., Sutherland, M., Schmidt, K.L., Schultz, P.W., Paterson, S.R., Martin-Barajas, A., 2003. Mesozoic tectonic evolution of the Peninsular Ranges of southern and Baja California, in: Johnson, S.E., Paterson, S.R., Fletcher, J.M., Girty, G.H., Kimbrough, D.L. (Eds.), Teconic evolution of northwestern Mexico and the southwestern USA. Geological Society of America, pp. 93-116.
Whitney, J.A., 1988. The origin of granite: the role and source of water in the evolution of granitic magmas. Geological Society of America Bulletin 100, 1886-1897.
Wiebe, R.A., 1994. Magma chambers as traps for basaltic magmas: the Cadillac Mountain Intrusive Complex, Mount Desert Island, Maine. Journal of Geology 102, 423-437.
Wiebe, R.A., Smith, D., Sturm, M., King, E.M., Seckler, M.S., 1997. Enclaves in the Cadillac Mountain Granite (coastal Maine): samples of hybrid magma from the base of the chamber. Journal of Petrology 38, 393-423.
Zhang, Y., Ni, H., Chen, Y., 2010. Diffusion data in silicate melts, in: Zhang, Y., Cherniak, D.J. (Eds.), Diffusion in minerals and melts, pp. 311-408.
Zimmer, M.M., Plank, T., Hauri, E.H., Yogodzinski, G.M., Stelling, P., Larsen, J., Singer, B., Jicha, B., Mandeville, C., Nye, C.J., 2010. The role of water in generating the calc-alkaline trend: new volatile data for Aleutian magmas and new tholeiitic index. Journal of Petrology 51, 2411-2444.
Zorpi, M.J., Coulon, C., Orsini, J.B., Cocirta, C., 1989. Magma mingling, zoning and emplacement in calc-alkaline granitoid plutons. Tectonophysics 157, 315-329.

Appendix A: Whole-rock compositions of mafic enclaves, granitoids and enclave rinds

Table 1. Whole Rock Major Oxide and Trace Element Compositions

Sample Name	BH01T1FH		BH01T2FH		BH01T1R1		BH01T1R2		BH01T2R1		BH01T2R2		BH01T1EI		BH01T2EI	
Lithology	Granitic Host		Granitic Host		Enclave Rind		Enclave Rind		Enclave Rind		Enclave Rind		Enclave Interior		Enclave Interior	
SiO_2 (wt%)	72.4		72.6		54.8		52.0		57.6		53.9		56.2		59.1	
TiO_2	0.38		0.4		1.11		1.33		0.94		1.06		0.98		0.85	
Al_2O_3	13.1		13.5		16.6		17.4		16.0		16.2		16.0		15.7	
Fe_2O_3	3.21		3.09		11.8		12.8		10.0		12.0		9.75		8.46	
MnO	0.07		0.07		0.24		0.25		0.22		0.27		0.22		0.2	
MgO	0.80		0.76		3.4		3.4		2.99		3.42		3.17		2.95	
CaO	3.29		3.16		5.44		5.6		5.39		6.67		5.62		5.5	
Na_2O	4.15		4.28		4.18		4.34		4.27		4.25		4.41		4.39	
K_2O	0.86		0.98		2.31		2.6		1.85		1.64		1.75		1.47	
P_2O_5	0.067		0.068		0.129		0.173		0.111		0.117		0.105		0.098	
Total	98.34		98.87		99.99		99.86		99.41		99.50		98.24		98.71	
		1 SD		1 SD		1 SD		1 SD		1 SD		1 SD		1 SD		1 SD
Cs (ppm)	1.65	0.11	2.20	0.11	6.61	0.57	7.46	0.38	4.12	0.53	3.62	0.30	4.65	0.14	2.94	0.31
Pb	7.01	0.61	7.01	0.45	6.09	0.67	7.32	0.04	5.65	1.00	8.04	1.06	7.16	11.11	5.71	3.06
Th	2.5	0.3	2.5	0.2	3.2	0.2	1.2	0.1	1.7	0.5	2.0	0.2	7.3	1.6	8.3	0.7
U	1.29	0.15	1.29	0.23	1.41	0.12	1.37	0.04	0.76	0.22	1.27	0.04	1.95	5.17	1.53	9.20
Ba	589	15	699	1	1074	47	1236	3	712	76	756	55	874	46	639	82.70
Rb	67	4	83	5	240	16	243	5	146	7	125	6	161	6	123	9
Nb	12	1	12	1	19	1	37	2	14	2	33	4	12	0	7	1.10
La	23.1	0.5	18.5	1.1	35.1	2.1	37.0	0.9	21.8	5.0	50.1	3.0	40.7	3.0	24.1	7.4
Ce	53.4	1.5	40.9	3.8	111	14	122	4	66.3	16.3	167	8	117	5	62.6	20.5
Pr	7.8	0.1	6.0	0.5	18.1	1.9	21.9	0.3	11.6	2.2	29.1	1.1	17.2	0.6	9.4	2.6
Sr	393	20	399	24	377	26	372	1	321	16	372	13	410	4	375	30
Nd	36.9	1.8	28.0	2.3	84.7	7.9	114.2	0.9	56.8	7.2	150.9	8.7	70.8	4.3	40.3	7.9
Zr	379	20	305	14	135	8	141	3	136	1	214	18	178	8	163	7
Sm	9.9	0.4	7.9	0.6	20.9	2.3	35.4	1.3	14.8	1.4	39.6	2.0	15.3	1.3	8.7	0.6
Eu	2.25	0.43	1.88	0.15	2.88	0.34	3.14	0.47	2.12	0.17	4.36	0.45	3.21	0.43	2.67	0.88
Tb	1.74	0.09	1.33	0.12	3.44	0.35	6.63	0.51	2.50	0.18	7.22	0.83	2.49	0.36	1.46	0.03
Dy	10.4	0.3	7.8	0.5	21.9	1.0	41.1	1.0	15.6	2.5	45.5	3.2	15.9	0.9	8.4	1.2
Y	33.3	2.6	41.6	2.1	95.0	11.7	146.9	7.8	75.4	2.1	185.2	10.1	67.6	0.9	45.6	3.2
Ho	2.15	0.15	1.56	0.16	4.18	0.08	7.86	0.14	3.15	0.46	8.76	1.03	3.44	0.07	1.76	0.35
Er	6.18	0.12	4.64	0.59	12.5	0.82	22.6	0.58	9.36	0.93	25.0	2.25	9.69	0.51	5.26	0.72
Yb	5.4	0.8	4.6	0.7	11.1	0.6	18.2	0.2	8.9	1.2	22.0	2.1	9.7	0.6	5.0	0.5
Lu	0.97	0.22	0.76	0.13	1.85	0.21	2.86	0.22	1.14	0.12	3.43	0.34	1.56	0.10	0.90	0.25

Appendix B: Whole rock major element and Zr contents Bernasconi Hills Transect Samples

Table 2. Bernasconi Hills transect whole rock major oxide and Zr compositions

Sample	11H1	12H1	13H1	14H1	15H1	16H1	17H1
Lithology	Granitoid	Granitoid	Granitoid	Granitoid	Granitoid	Granitoid	Granitoid
SiO2 (wt %)	71.75	70.76	72.42	71.25	74.52	73.56	69.24
TiO2	0.413	0.444	0.312	0.382	0.336	0.216	0.272
Al2O3	14.93	14.86	13.91	13.79	12.93	13.48	14.23
FeO*	2.34	3.18	2.31	3.02	2.73	1.97	3.24
MnO	0.026	0.045	0.028	0.034	0.032	0.033	0.063
MgO	0.72	0.78	0.47	0.63	0.57	0.49	0.82
CaO	3.40	3.79	2.75	2.84	2.49	2.55	3.35
Na2O	4.11	4.30	3.82	3.71	3.19	3.25	3.39
K2O	1.54	1.22	2.50	2.53	3.04	3.34	3.68
P2O5	0.082	0.107	0.061	0.083	0.080	0.069	0.100
Total	99.31	99.49	98.58	98.26	99.92	98.95	98.38
Zr (ppm)	181	263	207	289	316	196	235

Sample	18H1	19H1	110H1	111H1	11E1	12E1	13E1
Lithology	Granitoid	Granitoid	Granitoid	Granitoid	Mafic Enclave	Mafic Enclave	Mafic Enclave
SiO2 (wt %)	71.37	69.29	70.78	67.09	61.98	59.56	63.78
TiO2	0.369	0.333	0.425	0.463	0.727	1.027	0.546
Al2O3	14.17	14.68	14.25	15.70	15.82	17.69	15.14
FeO*	2.90	3.09	3.66	4.01	6.97	7.29	6.18
MnO	0.046	0.053	0.054	0.071	0.130	0.113	0.136
MgO	0.75	0.67	0.75	0.99	2.14	1.83	1.93
CaO	2.88	2.97	2.98	4.09	5.69	5.14	5.01
Na2O	3.73	3.85	3.88	4.63	4.15	4.65	4.17
K2O	2.83	3.21	2.47	1.25	1.37	2.11	1.55
P2O5	0.104	0.085	0.101	0.119	0.141	0.334	0.091
Total	99.14	98.22	99.35	98.41	99.11	99.75	98.53
Zr (ppm)	253	373	251	420	249	462	214

Sample	14E1	15E1	16E1	17E1	18E2	19E1	112E1
Lithology	Mafic Enclave	Mafic Enclave	Mafic Enclave	Mafic Enclave	Mafic Enclave	Mafic Enclave	Mafic Enclave
SiO2 (wt %)	63.95	60.93	54.45	52.97	62.44	63.40	59.58
TiO2	0.522	0.879	1.119	1.262	0.872	0.617	0.819
Al2O3	15.17	16.39	16.27	19.24	16.54	15.76	16.49
FeO*	5.69	7.55	11.31	9.61	6.29	6.33	7.51
MnO	0.130	0.126	0.207	0.168	0.089	0.123	0.149
MgO	2.11	2.10	3.18	2.47	1.75	1.80	2.78
CaO	4.73	5.36	6.47	5.04	4.68	5.05	6.04
Na2O	4.21	4.29	4.00	5.12	4.51	4.45	4.33
K2O	1.76	1.75	1.93	2.81	1.86	1.37	1.47
P2O5	0.084	0.171	0.112	0.365	0.204	0.106	0.102
Total	98.35	99.54	99.04	99.06	99.23	99.00	99.27
Zr (ppm)	238	223	130	577	252	219	166

Sample	18S1	21H1	22H1	22FMB1	23H1	24H1	25H1
Lithology	Schlieren	Granitoid	Granitoid	Granitoid	Granitoid	Granitoid	Granitoid
SiO2 (wt %)	56.39	74.62	67.24	72.02	68.54	69.58	71.17
TiO2	0.929	0.365	0.601	0.303	0.538	0.430	0.366
Al2O3	18.29	13.10	14.64	14.08	15.32	14.92	14.99
FeO*	8.55	2.70	4.86	2.34	3.35	3.65	2.83
MnO	0.143	0.038	0.077	0.038	0.041	0.062	0.045
MgO	2.20	0.60	1.12	0.62	0.79	0.87	0.73
CaO	5.63	2.79	3.48	2.82	2.90	3.35	3.36
Na2O	4.99	3.56	3.86	3.71	4.08	4.27	4.33
K2O	2.08	2.23	2.64	2.82	2.81	2.27	2.01
P2O5	0.267	0.089	0.139	0.077	0.109	0.102	0.088
Total	99.46	100.08	98.65	98.80	98.48	99.51	99.92
Zr (ppm)	304	264	409	293	273	209	239

Sample	26H1	27H1	28H1	29H1	210H1	211H1	212H1
Lithology	Granitoid	Granitoid	Granitoid	Granitoid	Granitoid	Granitoid	Granitoid
SiO2 (wt %)	68.30	69.39	71.00	73.08	71.53	73.69	73.95
TiO2	0.478	0.424	0.413	0.244	0.319	0.294	0.171
Al2O3	14.72	14.52	13.99	13.92	14.13	13.75	13.57
FeO*	3.96	3.49	3.58	1.79	2.62	2.37	1.58
MnO	0.068	0.058	0.062	0.027	0.041	0.035	0.025
MgO	0.99	0.87	0.77	0.42	0.58	0.50	0.27
CaO	3.57	3.37	3.39	2.28	2.70	2.45	1.95
Na2O	4.06	4.05	4.03	3.56	3.84	3.67	3.37
K2O	2.24	2.16	1.78	3.51	2.93	3.13	4.11
P2O5	0.124	0.105	0.104	0.052	0.072	0.065	0.037
Total	98.51	98.43	99.12	98.88	98.75	99.96	99.04
Zr (ppm)	266	405	240	199	218	263	142

Sample	213H1	214H1	215H1	216H1	217H1	218H1	219H1
Lithology	Granitoid	Granitoid	Granitoid	Granitoid	Granitoid	Granitoid	Granitoid
SiO2 (wt %)	73.13	72.95	75.94	70.96	73.18	71.82	74.02
TiO2	0.293	0.255	0.203	0.474	0.393	0.420	0.315
Al2O3	13.89	13.49	12.90	14.38	12.16	14.43	13.12
FeO*	2.35	2.29	1.35	3.22	3.84	2.86	2.46
MnO	0.035	0.020	0.014	0.033	0.063	0.028	0.037
MgO	0.57	0.17	0.32	0.79	0.82	0.62	0.54
CaO	2.57	1.78	2.03	3.17	3.12	3.15	2.62
Na2O	3.65	3.36	3.15	4.35	3.69	4.44	3.71
K2O	3.13	4.00	3.44	1.42	1.10	1.22	2.25
P2O5	0.069	0.030	0.041	0.148	0.060	0.079	0.073
Total	99.68	98.36	99.39	98.95	98.44	99.07	99.14
Zr (ppm)	275	170	171	188	359	170	240

Sample	220H1	221H1	222H1	223H1	224H1	225H1	226H1
Lithology	Granitoid	Granitoid	Granitoid	Granitoid	Granitoid	Granitoid	Granitoid
SiO2 (wt %)	71.54	63.38	56.84	54.41	62.95	73.15	69.73
TiO2	0.291	0.828	1.403	1.005	0.835	0.403	0.534
Al2O3	14.44	15.49	17.02	21.17	16.46	14.02	14.55
FeO*	2.52	6.34	8.46	6.39	6.20	2.34	3.71
MnO	0.035	0.081	0.181	0.104	0.094	0.024	0.053
MgO	0.57	1.52	3.32	2.17	2.17	0.70	1.31
CaO	2.63	3.70	6.84	7.16	5.02	3.58	4.10
Na2O	4.00	4.33	4.07	5.35	4.07	3.66	3.75
K2O	3.10	2.11	1.63	1.64	1.85	1.19	1.36
P2O5	0.073	0.164	0.189	0.194	0.117	0.078	0.082
Total	99.19	97.93	99.95	99.58	99.77	99.14	99.19
Zr (ppm)	236	446	134	885	194	179	220

Sample	227H1	228H1	21E1	24E1	25E1	27E1	29E1
Lithology	Granitoid	Granitoid	Mafic Enclave	Mafic Enclave	Mafic Enclave	Mafic Enclave	Mafic Enclave
SiO2 (wt %)	71.37	74.06	62.68	56.93	57.84	57.76	60.87
TiO2	0.250	0.276	0.807	1.147	0.944	0.954	0.956
Al2O3	14.96	13.79	15.90	17.50	17.12	16.92	16.61
FeO*	2.08	1.93	6.63	7.67	7.85	8.96	6.87
MnO	0.040	0.031	0.116	0.152	0.155	0.167	0.131
MgO	0.66	0.56	1.77	3.12	2.53	2.45	2.69
CaO	4.31	3.46	4.86	7.31	5.46	5.84	6.43
Na2O	4.28	3.84	4.33	4.38	4.61	4.49	4.02
K2O	0.68	0.88	1.62	1.29	1.84	1.77	1.41
P2O5	0.133	0.054	0.122	0.177	0.107	0.195	0.136
Total	98.75	98.88	98.84	99.68	98.45	99.51	100.10
Zr (ppm)	75	131	182	233	173	192	139

Sample	210E1	211E1	212E1	213E1	213MB1	214E1	217E1
Lithology	Mafic Enclave	Mafic Enclave	Mafic Enclave	Mafic Enclave	Mafic Enclave	Mafic Enclave	Mafic Enclave
SiO2 (wt %)	63.21	60.54	55.97	60.91	58.26	57.38	61.02
TiO2	0.927	0.810	0.745	0.763	0.877	0.948	0.861
Al2O3	15.20	16.37	17.14	16.68	16.66	17.07	16.54
FeO*	6.98	8.03	7.28	6.71	7.13	7.33	6.93
MnO	0.114	0.162	0.180	0.132	0.163	0.136	0.142
MgO	1.86	2.71	4.15	2.31	3.43	3.40	2.95
CaO	4.22	5.48	7.45	5.21	6.37	7.27	6.33
Na2O	4.22	4.72	4.82	4.75	4.74	5.11	4.04
K2O	1.83	1.57	1.09	1.59	1.62	1.02	1.50
P2O5	0.079	0.087	0.077	0.098	0.102	0.114	0.118
Total	98.65	100.47	98.91	99.16	99.35	99.77	100.44
Zr (ppm)	165	120	103	96	100	129	125

Sample	218E1	219E1	221E1	222MB2	222FMB2	223E1	224E1
Lithology	Mafic Enclave	Mafic Enclave	Mafic Enclave	Mafic Enclave	Mafic Enclave	Mafic Enclave	Mafic Enclave
SiO2 (wt %)	59.57	55.04	65.72	49.24	57.50	52.20	62.85
TiO2	0.868	1.160	0.643	1.575	1.267	1.416	0.906
Al2O3	16.50	17.14	15.38	18.44	16.35	17.69	16.28
FeO*	7.57	8.67	5.83	10.10	7.99	9.75	6.46
MnO	0.152	0.180	0.116	0.207	0.160	0.176	0.103
MgO	2.72	3.74	2.09	3.90	3.11	4.27	2.17
CaO	5.15	7.93	4.52	8.57	6.50	8.15	5.31
Na2O	4.46	4.66	4.20	3.81	3.83	3.73	3.91
K2O	1.95	1.04	1.58	1.76	1.63	1.66	1.69
P2O5	0.112	0.135	0.080	0.253	0.166	0.213	0.151
Total	99.05	99.71	100.15	97.85	98.50	99.25	99.83
Zr (ppm)	133	88	133	199	134	104	200

Sample	225E1	226E1	227E1	229E1	2POST29 LgEn	2POST29FMB3	ENC "B"
Lithology	Mafic Enclave	Mafic Enclave	Mafic Enclave	Mafic Enclave	Mafic Enclave	Granitoid	Mafic Enclave
SiO2 (wt %)	57.70	54.59	60.03	63.42	58.28	55.98	65.85
TiO2	0.874	1.317	0.913	0.877	0.841	1.138	0.541
Al2O3	17.42	17.52	16.07	16.06	16.48	16.44	14.63
FeO*	6.89	9.11	7.45	6.29	6.70	8.58	5.70
MnO	0.145	0.141	0.136	0.095	0.137	0.171	0.164
MgO	3.13	3.21	2.63	1.91	3.00	3.99	1.93
CaO	7.23	6.29	5.69	4.03	6.70	6.74	4.28
Na2O	4.07	3.70	3.93	4.15	4.93	3.71	4.17
K2O	1.23	2.30	1.63	2.07	0.92	1.76	2.42
P2O5	0.105	0.233	0.101	0.131	0.097	0.130	0.081
Total	98.78	98.40	98.59	99.02	98.09	98.63	99.77
Zr (ppm)	72	294	123	164	100	212	174

Sample	ENC MB3	E2	E3	S5	S6	S8	E9
Lithology	Mafic Enclave	Mafic Enclave	Mafic Enclave	Schlieren	Schlieren	Schlieren	Mafic Enclave
SiO2 (wt %)	60.22	57.37	67.26	63.34	67.54	52.87	54.05
TiO2	0.763	1.120	0.561	0.816	0.663	1.175	0.796
Al2O3	15.22	17.53	14.85	16.30	14.38	18.70	16.87
FeO*	7.60	8.30	4.72	6.16	5.27	10.40	7.38
MnO	0.210	0.162	0.088	0.108	0.097	0.192	0.203
MgO	2.49	2.90	1.51	1.52	1.29	2.49	4.12
CaO	5.14	6.47	4.17	4.19	2.99	5.89	8.12
Na2O	4.51	4.64	4.28	5.12	4.16	5.45	4.66
K2O	1.59	1.64	1.36	1.57	2.69	2.15	1.67
P2O5	0.107	0.148	0.088	0.208	0.103	0.297	0.083
Total	97.85	100.28	98.89	99.34	99.19	99.62	97.94
Zr (ppm)	198	120	188	239	218	216	119

Sample	ERS7A1E	ERS7A1H	ERS7A1R	ERS7A2E	ERS7A2H	ERS7A2R	ERS7B3E
Lithology	Mafic Enclave	Granitoid	Enclave Rind	Mafic Enclave	Granitoid	Enclave Rind	Mafic Enclave
SiO2 (wt %)	61.69	64.20	55.64	63.04	67.56	56.61	60.94
TiO2	0.810	0.651	0.983	0.754	0.528	0.925	0.821
Al2O3	16.10	15.49	16.99	15.75	15.03	17.18	16.09
FeO*	7.39	6.39	10.13	6.53	4.73	9.19	7.43
MnO	0.145	0.126	0.207	0.125	0.089	0.183	0.143
MgO	2.00	1.64	2.64	1.91	1.22	2.38	2.08
CaO	5.05	4.78	6.14	4.64	4.03	5.78	4.97
Na2O	4.53	4.40	4.54	4.49	4.36	4.66	4.47
K2O	1.56	1.68	1.87	1.54	1.73	1.95	1.66
P2O5	0.084	0.256	0.122	0.079	0.154	0.123	0.086
Total	99.34	99.62	99.26	98.88	99.43	98.99	98.68
Zr (ppm)	97	360	71	113	656	110	98

Sample	ERS7B3H	ERS7B3R
Lithology	Granitoid	Enclave Rind
SiO2 (wt %)	70.32	55.39
TiO2	0.524	1.041
Al2O3	14.88	17.62
FeO*	3.77	9.46
MnO	0.059	0.189
MgO	0.96	2.62
CaO	3.44	5.87
Na2O	4.45	4.61
K2O	1.39	2.04
P2O5	0.112	0.138
Total	99.93	98.98
Zr (ppm)	373	82

Appendix C: Plagioclase Compositional Transect Compositions

Table 3. Plagioclase compositional transect data

Point	214H1-plag1a	214H1-plag1b	214H1-plag1c	214H1-plag1d	214H1-plag1e
Distance (mm)	0.00	0.05	0.10	0.14	0.19
An (mole %)	43	44	44	45	38
Ab (mole %)	56	55	55	54	61
Or (mole %)	1	1	1	1	1
Mg (ppm)	9	6	11	4	10
Fe (ppm)	401	691	751	869	899
Sr (ppm)	425	391	350	307	381

Point	214H1-plag1f	214H1-plag1g	214H1-plag1h	214H1-plag1i	214H1-plag1j
Distance (mm)	0.24	0.29	0.34	0.39	0.45
An (mole %)	41	43	39	41	41
Ab (mole %)	58	55	59	58	57
Or (mole %)	1	1	1	1	1
Mg (ppm)	5	5	11	3	5
Fe (ppm)	930	968	1051	873	832
Sr (ppm)	348	322	356	339	341

Point	214H1-plag1k	214H1-plag1l	214H1-plag1m	214H1-plag1n	214H1-plag1o
Distance (mm)	0.50	0.56	0.61	0.66	0.71
An (mole %)	45	41	40	42	40
Ab (mole %)	54	58	59	56	59
Or (mole %)	1	1	1	2	1
Mg (ppm)	6	8	7	3	6
Fe (ppm)	705	681	723	745	834
Sr (ppm)	360	362	331	323	353

Point	214H1-plag1p	214H1-plag1q	214H1-plag1r	214H1-plag1s	214H1-plag1t
Distance (mm)	0.76	0.82	0.87	0.99	1.05
An (mole %)	40	39	38	41	40
Ab (mole %)	58	59	61	58	59
Or (mole %)	1	1	1	1	1
Mg (ppm)	7	3	3	3	7
Fe (ppm)	800	858	714	497	636
Sr (ppm)	338	364	317	322	333

Point	214H1-plag1u	214H1-plag1v	214H1-plag1w	214H1-plag1x	214H1-plag1y
Distance (mm)	1.10	1.15	1.23	1.29	1.34
An (mole %)	40	40	42	42	40
Ab (mole %)	59	59	56	57	59
Or (mole %)	1	1	1	1	1
Mg (ppm)	2	4	6	3	4
Fe (ppm)	684	902	977	829	604
Sr (ppm)	360	320	366	349	397

Point	214H1-plag1z	214H1-plag1aa	214H1-plag1ab	214H1-plag1ac	214H1-plag1ad
Distance (mm)	1.39	1.43	1.48	1.53	1.59
An (mole %)	45	43	43	37	38
Ab (mole %)	54	55	56	62	61
Or (mole %)	1	1	1	1	1
Mg (ppm)	5	3	5	4	20
Fe (ppm)	689	825	755	843	1147
Sr (ppm)	372	313	366	322	346

Point	214H1-plag1ae	214H1-plag1af	214H1-plag1ag	214H1-plag1ah	214H1-plag1ai
Distance (mm)	1.64	1.72	1.78	1.86	1.90
An (mole %)	37	37	41	38	34
Ab (mole %)	62	61	58	60	64
Or (mole %)	1	1	1	1	1
Mg (ppm)	11	5	4	7	7
Fe (ppm)	991	918	821	963	1148
Sr (ppm)	335	317	293	340	341

Point	214H1-plag1aj	214H1-plag1ak	214H1-plag1al	214H1-plag1am	214H1-plag1an
Distance (mm)	1.98	2.05	2.10	2.16	2.22
An (mole %)	42	41	39	35	40
Ab (mole %)	56	58	59	63	59
Or (mole %)	2	1	1	1	1
Mg (ppm)	6	8	4	4	7
Fe (ppm)	1136	1209	996	910	987
Sr (ppm)	341	310	314	337	335

Point	214H1-plag1ao	214H1-plag1ap	214H1-plag1aq	214H1-plag1ar	214H1-plag1at
Distance (mm)	2.27	2.33	2.38	2.44	2.56
An (mole %)	39	40	36	39	37
Ab (mole %)	60	59	63	60	62
Or (mole %)	1	1	1	1	1
Mg (ppm)	6	4	2	1	3
Fe (ppm)	880	713	727	687	889
Sr (ppm)	352	350	291	349	326

Point	214H1-plag1au	214H1-plag1av	214H1-plag1aw	214H1-plag1ax
Distance (mm)	2.62	2.68	2.72	2.78
An (mole %)	42	36	42	38
Ab (mole %)	57	63	58	61
Or (mole %)	1	1	1	1
Mg (ppm)	4	4	4	5
Fe (ppm)	667	708	596	421
Sr (ppm)	353	336	356	360

Point	214H1-plag2a	214H1-plag2b	214H1-plag2c	214H1-plag2d	214H1-plag2e
Distance (mm)	0.00	0.06	0.11	0.17	0.23
An (mole %)	40	40	41	39	39
Ab (mole %)	59	59	58	60	60
Or (mole %)	1	1	1	1	1
Mg (ppm)	2	5	8	7	4
Fe (ppm)	652	637	692	761	849
Sr (ppm)	334	336	354	319	334

Point	214H1-plag2f	214H1-plag2g	214H1-plag2h	214H1-plag2i	214H1-plag2j
Distance (mm)	0.29	0.34	0.38	0.43	0.48
An (mole %)	38	40	40	41	40
Ab (mole %)	60	59	58	58	59
Or (mole %)	1	1	1	1	1
Mg (ppm)	10	8	8	4	4
Fe (ppm)	886	872	892	694	711
Sr (ppm)	336	372	353	326	341

Point	214H1-plag2k	214H1-plag2l	214H1-plag2m	214H1-plag2n	214H1-plag2o
Distance (mm)	0.54	0.60	0.66	0.72	0.79
An (mole %)	40	40	43	41	42
Ab (mole %)	59	58	56	58	57
Or (mole %)	1	1	1	1	1
Mg (ppm)	6	5	11	10	5
Fe (ppm)	839	710	620	520	658
Sr (ppm)	353	318	357	334	337

Point	214H1-plag2p	214H1-plag2q	214H1-plag2r	214H1-plag2s	214H1-plag2t
Distance (mm)	0.85	0.90	0.97	1.02	1.09
An (mole %)	40	41	41	38	36
Ab (mole %)	59	58	58	61	62
Or (mole %)	1	1	1	1	1
Mg (ppm)	8	8	8	6	19
Fe (ppm)	671	735	809	770	777
Sr (ppm)	347	349	333	350	306

Point	214H1-plag2u	214H1-plag2v	214H1-plag2w	214H1-plag2x	214H1-plag2y
Distance (mm)	1.16	1.27	1.32	1.38	1.43
An (mole %)	39	39	44	42	41
Ab (mole %)	59	60	55	56	58
Or (mole %)	1	1	1	1	1
Mg (ppm)	13	21	6	21	4
Fe (ppm)	866	890	765	651	567
Sr (ppm)	324	339	326	322	336

Point	214H1-plag4a	214H1-plag4b	214H1-plag4c	214H1-plag4d	214H1-plag4e
Distance (mm)	0.00	0.05	0.10	0.15	0.21
An (mole %)	41	38	41	37	41
Ab (mole %)	58	61	58	62	58
Or (mole %)	1	1	1	1	1
Mg (ppm)	2	3	3	4	5
Fe (ppm)	495	649	711	749	745
Sr (ppm)	328	343	337	341	366

Point	214H1-plag4f	214H1-plag4g	214H1-plag4h	214H1-plag4i	214H1-plag4j
Distance (mm)	0.25	0.29	0.35	0.40	0.45
An (mole %)	39	36	39	39	40
Ab (mole %)	60	62	60	60	59
Or (mole %)	1	1	1	1	1
Mg (ppm)	4	4	3	5	4
Fe (ppm)	789	916	835	895	925
Sr (ppm)	368	339	335	368	341

Point	214H1-plag4k	214H1-plag4l	214H1-plag4m	214H1-plag4n	214H1-plag4o
Distance (mm)	0.50	0.56	0.62	0.68	0.73
An (mole %)	41	40	43	41	42
Ab (mole %)	57	59	56	57	57
Or (mole %)	1	1	1	1	1
Mg (ppm)	6	5	6	5	4
Fe (ppm)	935	927	875	962	781
Sr (ppm)	339	395	337	378	327

Point	214H1-plag4p	214H1-plag4q	214H1-plag4r	214H1-plag4s	214H1-plag4t
Distance (mm)	0.78	0.84	0.89	0.94	0.99
An (mole %)	37	40	39	40	39
Ab (mole %)	62	59	60	59	61
Or (mole %)	1	1	1	1	1
Mg (ppm)	5	3	2	5	3
Fe (ppm)	691	552	443	418	373
Sr (ppm)	329	349	371	341	380

Point	214H1-plag4u
Distance (mm)	1.05
An (mole %)	42
Ab (mole %)	57
Or (mole %)	1
Mg (ppm)	2
Fe (ppm)	383
Sr (ppm)	350

Point	ERS7B3B-plag1a	ERS7B3B-plag1b	ERS7B3B-plag1c	ERS7B3B-plag1d	ERS7B3B-plag1e
Distance (mm)	0.00	0.06	0.11	0.15	0.20
An (mole %)	38	37	38	40	41
Ab (mole %)	61	62	62	59	58
Or (mole %)	1	1	1	1	1
Mg (ppm)	13	18	14	8	6
Fe (ppm)	543	404	658	822	790
Sr (ppm)	459	408	429	409	397

Point	ERS7B3B-plag1f	ERS7B3B-plag1g	ERS7B3B-plag1h	ERS7B3B-plag1i	ERS7B3B-plag1j
Distance (mm)	0.25	0.29	0.34	0.39	0.43
An (mole %)	39	36	36	33	38
Ab (mole %)	60	62	63	67	61
Or (mole %)	1	2	1	1	1
Mg (ppm)	11	6	6	12	13
Fe (ppm)	789	628	629	561	638
Sr (ppm)	364	366	370	381	362

Point	ERS7B3B-plag1k	ERS7B3B-plag1l	ERS7B3B-plag1m	ERS7B3B-plag1n	ERS7B3B-plag1o
Distance (mm)	0.47	0.51	0.55	0.60	0.64
An (mole %)	36	35	36	38	36
Ab (mole %)	62	64	63	59	63
Or (mole %)	2	1	1	3	1
Mg (ppm)	9	9	4	22	17
Fe (ppm)	600	651	839	510	438
Sr (ppm)	364	375	400	378	435

Point	ERS7B3B-plag1p	ERS7B3B-plag1q	ERS7B3B-plag1r	ERS7B3B-plag1s	ERS7B3B-plag1t
Distance (mm)	0.68	0.73	0.77	0.81	0.85
An (mole %)	35	34	32	35	33
Ab (mole %)	64	65	65	64	66
Or (mole %)	2	1	3	1	1
Mg (ppm)	7	9	10	8	15
Fe (ppm)	673	759	735	783	680
Sr (ppm)	345	448	365	378	448

Point	ERS7B3B-plag1u	ERS7B3B-plag1v	ERS7B3B-plag1w	ERS7B3B-plag1x	ERS7B3B-plag1y
Distance (mm)	0.89	0.94	0.98	1.03	1.08
An (mole %)	38	38	41	35	35
Ab (mole %)	61	61	58	64	64
Or (mole %)	1	1	1	1	1
Mg (ppm)	10	13	9	8	12
Fe (ppm)	623	542	609	537	606
Sr (ppm)	415	394	385	345	434

Point	ERS7B3B-plag1z	ERS7B3B-plag1aa	ERS7B3B-plag1ab
Distance (mm)	1.12	1.16	1.21
An (mole %)	39	37	37
Ab (mole %)	60	63	62
Or (mole %)	1	1	1
Mg (ppm)	19	11	6
Fe (ppm)	566	525	471
Sr (ppm)	357	437	379

Point	ERS7B3B-plag3a	ERS7B3B-plag3b	ERS7B3B-plag3c	ERS7B3B-plag3d	ERS7B3B-plag3e
Distance (mm)	0.00	0.05	0.11	0.17	0.23
An (mole %)	40	39	38	37	39
Ab (mole %)	59	60	61	62	60
Or (mole %)	1	1	1	1	1
Mg (ppm)	10	9	8	6	9
Fe (ppm)	548	655	358	351	328
Sr (ppm)	364	391	360	355	399

Point	ERS7B3B-plag3f	ERS7B3B-plag3g	ERS7B3B-plag3h	ERS7B3B-plag3i	ERS7B3B-plag3j
Distance (mm)	0.29	0.35	0.40	0.45	0.50
An (mole %)	39	39	40	38	42
Ab (mole %)	61	60	59	61	57
Or (mole %)	1	1	1	1	1
Mg (ppm)	7	7	10	11	9
Fe (ppm)	335	361	270	330	318
Sr (ppm)	379	382	342	357	368

Point	ERS7B3B-plag3k	ERS7B3B-plag3l	ERS7B3B-plag3m	ERS7B3B-plag3n	ERS7B3B-plag3o
Distance (mm)	0.55	0.60	0.66	0.72	0.78
An (mole %)	39	39	39	37	38
Ab (mole %)	61	61	60	63	60
Or (mole %)	1	1	1	1	1
Mg (ppm)	6	6	16	7	9
Fe (ppm)	406	241	271	293	313
Sr (ppm)	391	369	390	383	354

Point	ERS7B3B-plag3p	ERS7B3B-plag3q	ERS7B3B-plag3r	ERS7B3B-plag3s	ERS7B3B-plag3t
Distance (mm)	0.83	0.89	0.95	1.01	1.06
An (mole %)	38	39	35	39	38
Ab (mole %)	61	60	64	61	61
Or (mole %)	1	1	1	1	1
Mg (ppm)	4	10	18	8	18
Fe (ppm)	295	302	291	312	348
Sr (ppm)	413	381	346	388	417

Point	ERS7B3B-plag3u	ERS7B3B-plag3v	ERS7B3B-plag3w	ERS7B3B-plag3x
Distance (mm)	1.12	1.18	1.24	1.33
An (mole %)	38	39	37	40
Ab (mole %)	62	61	62	59
Or (mole %)	1	1	1	1
Mg (ppm)	13	12	10	9
Fe (ppm)	386	461	441	401
Sr (ppm)	363	436	433	393

Point	215H1-plag3a	215H1-plag3b	215H1-plag3c	215H1-plag3d	215H1-plag3e
Distance (mm)	0.00	0.04	0.08	0.11	0.15
An (mole %)	43	43	43	43	46
Ab (mole %)	56	56	56	56	53
Or (mole %)	1	1	1	1	1
Mg (ppm)	8	6	8	6	11
Fe (ppm)	714	657	524	556	570
Sr (ppm)	407	397	365	357	437

Point	215H1-plag3f	215H1-plag3g	215H1-plag3h	215H1-plag3i	215H1-plag3j
Distance (mm)	0.18	0.23	0.28	0.33	0.39
An (mole %)	44	40	42	45	43
Ab (mole %)	55	59	56	54	55
Or (mole %)	1	1	1	1	1
Mg (ppm)	6	3	6	6	4
Fe (ppm)	545	537	725	783	618
Sr (ppm)	389	355	450	441	366

Point	215H1-plag3k	215H1-plag3l	215H1-plag3m	215H1-plag3n	215H1-plag3o
Distance (mm)	0.44	0.49	0.54	0.60	0.65
An (mole %)	41	40	46	39	42
Ab (mole %)	58	59	53	60	57
Or (mole %)	1	1	1	1	2
Mg (ppm)	3	8	6	6	11
Fe (ppm)	567	729	908	874	754
Sr (ppm)	378	346	399	407	329

Point	215H1-plag3p	215H1-plag3q	215H1-plag3r	215H1-plag3s	215H1-plag3t
Distance (mm)	0.71	0.77	0.82	0.88	0.95
An (mole %)	42	40	40	40	41
Ab (mole %)	57	59	59	59	58
Or (mole %)	1	1	2	1	1
Mg (ppm)	4	5	13	4	13
Fe (ppm)	838	803	834	916	834
Sr (ppm)	375	378	373	369	336

Point	215H1-plag3u	215H1-plag3v	215H1-plag3w	215H1-plag3x	215H1-plag3y
Distance (mm)	1.01	1.07	1.13	1.19	1.24
An (mole %)	42	37	41	42	39
Ab (mole %)	57	62	58	57	60
Or (mole %)	1	1	1	1	1
Mg (ppm)	6	6	7	13	4
Fe (ppm)	750	628	813	751	670
Sr (ppm)	377	372	376	355	377

Point	215H1-plag3z	215H1-plag3ab	215H1-plag3ac	215H1-plag3ae	215H1-plag3ag
Distance (mm)	1.29	1.41	1.46	1.57	1.70
An (mole %)	39	37	40	41	38
Ab (mole %)	60	62	60	58	61
Or (mole %)	1	1	1	1	1
Mg (ppm)	2	3	7	7	13
Fe (ppm)	867	551	479	434	693
Sr (ppm)	402	357	397	405	342

Point	215H1-plag3ah	215H1-plag3ai	215H1-plag3aj
Distance (mm)	1.76	1.82	1.88
An (mole %)	45	40	46
Ab (mole %)	54	59	53
Or (mole %)	1	1	1
Mg (ppm)	6	4	6
Fe (ppm)	830	525	641
Sr (ppm)	378	406	383

Point					
Distance (mm)	215H1-plag2a	215H1-plag2b	215H1-plag2c	215H1-plag2d	215H1-plag2e
	0.00	0.06	0.11	0.16	0.21
An (mole %)					
Ab (mole %)	46	43	40	44	44
Or (mole %)	53	55	58	54	54
Mg (ppm)	1	1	1	1	1
Fe (ppm)	13	9	8	8	13
Sr (ppm)	688	693	755	891	1133
	409	400	413	390	405

Point	215H1-plag2f	215H1-plag2g	215H1-plag2h	215H1-plag2i	215H1-plag2j
Distance (mm)	0.26	0.32	0.37	0.41	0.45
An (mole %)	43	43	43	44	48
Ab (mole %)	56	56	55	54	50
Or (mole %)	1	1	2	2	1
Mg (ppm)	8	11	11	21	18
Fe (ppm)	950	1044	1182	1145	946
Sr (ppm)	413	376	376	402	380

Point	215H1-plag2k	215H1-plag2l	215H1-plag2m	215H1-plag2n	215H1-plag2o
Distance (mm)	0.49	0.53	0.57	0.62	0.66
An (mole %)	44	41	47	44	44
Ab (mole %)	54	57	51	54	55
Or (mole %)	1	2	1	1	1
Mg (ppm)	19	18	20	9	10
Fe (ppm)	1143	1030	1381	847	1064
Sr (ppm)	343	417	403	370	423

Point	215H1-plag2p	215H1-plag2q	215H1-plag2r	215H1-plag2s	215H1-plag2t
Distance (mm)	0.71	0.76	0.81	0.86	0.91
An (mole %)	46	47	43	46	44
Ab (mole %)	53	52	56	53	55
Or (mole %)	1	1	1	1	1
Mg (ppm)	13	16	17	28	14
Fe (ppm)	1091	1150	1020	1120	1052
Sr (ppm)	407	392	403	390	411

Point	215H1-plag2u	215H1-plag2v	215H1-plag2w
Distance (mm)	0.96	1.01	1.05
An (mole %)	41	43	42
Ab (mole %)	58	56	57
Or (mole %)	1	1	1
Mg (ppm)	13	22	6
Fe (ppm)	1011	868	746
Sr (ppm)	372	349	442

Appendix D: Linear Regression Values for Global Composition-Elevation Trends

Table 4. Linear regression values for mean major oxide contents in arc lavas as functions of elevation

Regressions for major element composition (wt %) as a function of elevation (m) in the form X(h) = Ah+B

10 km^2 elevation model

	A	B	r^2	p-value
SiO2	0.00124	56.81	0.62	0.05
MgO	-0.000335	4.381	0.46	0.05
TiO2	-1.51E-05	0.8873	0.08	0.05
FeO*	-0.00059	7.539	0.79	0.05
CaO	-0.000638	7.77	0.7	0.05
K2O	0.0003063	1.388	0.68	0.05

FeO* = total Fe cast as FeO

Appendix E: Fitted Parameters for melt % (F) and SiO_2 (wt %) as functions of temperature

Table 5. Parameters for *F* and SiO_2 as functions of temperature from Rhyolite-MELTS output

Parameters for F(T)	
a7	575.9
a6	-321.6
a5	-2962
a4	5707
a3	-4156
a2	1295
a1	-38.30
a0	0
Parameters for SiO2(T)	
b6	-1561
b5	5762
b4	-8353
b3	5999
b2	-2190
b1	342.7
b0	51.92

Appendix F: Global volcanic arc mean and median compositions with standard deviation

Table 6. Mean arc lava compositions grouped by elevation

Elevation Bin	SiO2 (wt%)	TiO2 (wt%)	Al2O3 (wt%)	FeO* (wt%)	MnO (wt%)	MgO (wt%)	CaO (wt%)
-1000	47.83	0.77	16.86	8.84	0.16	8.34	11.96
-900	56.51	0.76	16.73	8.22	0.17	4.26	8.76
-800	56.24	0.65	16.10	8.62	0.16	4.60	9.06
-700	57.00	0.78	17.11	7.55	0.17	3.88	8.17
-600	58.53	0.75	16.65	7.25	0.18	3.69	7.72
-500	54.33	0.90	17.30	7.50	0.16	4.62	8.72
-400	54.54	0.80	16.81	9.01	0.18	4.71	9.61
-300	56.42	0.80	16.61	7.68	0.15	4.65	8.33
-200	57.43	0.76	16.55	7.70	0.15	4.09	7.33
-100	59.05	0.77	16.37	6.62	0.14	3.53	6.77
0	57.73	0.92	16.45	7.48	0.15	4.14	7.27
100	58.75	0.95	16.28	6.90	0.14	4.00	6.59
200	59.00	0.83	16.61	6.93	0.14	3.69	6.99
300	57.55	0.96	16.72	7.61	0.18	4.01	7.35
400	57.97	0.94	16.59	7.60	0.14	3.80	7.16
500	60.17	0.89	16.42	6.65	0.12	3.26	6.33
600	59.01	1.01	16.63	6.89	0.13	3.46	6.22
700	59.30	0.92	16.41	7.06	0.14	3.59	6.73
800	58.92	0.92	16.63	6.87	0.18	3.66	6.72
900	57.34	1.02	16.21	7.40	0.14	4.69	7.05
1000	59.19	0.90	16.50	6.99	0.14	3.88	6.48
1100	57.49	0.99	17.14	7.15	0.13	3.90	6.99
1200	56.96	1.04	16.94	7.44	0.23	4.20	7.08
1300	57.98	0.94	16.82	6.92	0.15	4.10	6.90
1400	57.30	0.86	16.86	7.09	0.17	4.45	7.29
1500	56.33	0.93	17.29	7.39	0.15	3.86	7.69
1600	59.31	0.96	16.72	6.38	0.11	3.54	6.29
1700	55.65	1.16	16.62	7.74	0.17	4.93	7.60
1800	58.40	0.85	16.88	6.21	0.12	4.43	6.82
1900	59.73	0.99	16.72	6.39	0.11	3.38	6.00
2000	58.46	0.94	17.11	6.29	0.12	3.68	6.54
2100	58.59	0.91	16.75	6.46	0.12	3.94	6.76
2200	58.31	1.00	16.96	6.42	0.12	4.16	6.57
2300	60.52	0.97	16.55	5.80	0.11	3.43	5.72
2400	60.39	0.90	16.64	5.72	0.11	3.29	5.52
2500	61.13	0.76	16.83	5.31	0.10	3.44	5.66
2600	56.49	0.95	17.20	6.73	0.13	4.65	7.15
2700	60.58	0.82	16.76	5.46	0.11	3.32	5.58
2800	62.79	0.77	16.34	4.70	0.09	3.29	4.75
2900	59.77	0.78	16.69	5.76	0.11	3.96	6.42
3000	59.91	1.07	16.29	5.75	0.11	4.20	5.51
3100	61.56	0.83	16.21	5.04	0.09	3.62	5.46
3200	59.91	0.78	17.00	5.62	0.11	3.37	5.79
3300	61.22	0.75	16.89	5.47	0.10	2.98	5.66
3400	61.74	0.73	16.36	5.50	0.10	3.07	5.46
3500	60.96	0.88	16.68	5.02	0.08	2.93	5.45
3600	62.17	0.77	16.00	5.08	0.09	3.11	5.15
3700	56.84	0.91	16.43	6.98	0.13	5.10	7.39
3800	60.36	0.86	16.25	5.54	0.10	3.70	5.71
3900	61.56	0.68	16.25	5.39	0.10	3.29	5.42
4000	61.40	0.91	16.32	5.49	0.10	2.74	5.35

Elevation Bin	SiO2 (wt%)	TiO2 (wt%)	Al2O3 (wt%)	FeO* (wt%)	MnO (wt%)	MgO (wt%)	CaO (wt%)
4100	62.81	0.80	16.23	4.74	0.08	2.84	4.80
4200	62.96	0.76	16.24	4.68	0.08	2.89	4.86
4300	62.55	0.80	16.46	4.96	0.09	2.42	4.95
4400	63.25	0.78	16.16	4.56	0.07	2.96	4.58
4500	63.08	0.81	16.01	4.83	0.09	2.57	4.82
4600	63.25	0.91	15.96	4.73	0.08	2.33	4.50
4700	62.82	0.75	16.24	4.87	0.09	2.77	4.95
4800	64.64	0.76	15.90	4.26	0.08	2.12	4.25
4900	60.03	0.88	16.45	5.79	0.10	3.49	5.80
5000	63.01	0.76	16.27	4.65	0.08	2.45	4.72
5100	64.18	0.71	16.15	4.38	0.08	2.35	4.35
5200	66.66	0.67	15.32	3.55	0.06	1.91	3.49
5300	63.59	0.83	15.79	4.49	0.08	2.25	4.55
5400	59.28	0.95	16.26	5.95	0.10	3.79	6.01
5500	62.89	0.67	16.42	4.99	0.08	2.52	4.92
5600	66.93	0.74	15.58	2.95	0.04	1.28	2.84
5700	66.97	0.60	15.32	3.20	0.05	1.57	3.16
5900	59.69	0.87	16.40	5.19	0.09	3.74	5.85

Elevation Bin	Na2O (wt%)	K2O (wt%)	P2O5 (wt%)	Rb (ppm)	Sr (ppm)	Y (ppm)	Zr (ppm)
-1000	2.14	1.37	0.492	22	816	28	76
-900	2.88	0.87	0.138	15	299	27	78
-800	2.45	0.91	0.126	23	305	17	63
-700	3.31	1.08	0.167	22	397	25	88
-600	3.44	0.87	0.158	19	273	27	84
-500	2.91	2.32	0.352	73	599	26	163
-400	2.48	0.68	0.122	15	241	25	69
-300	2.88	1.44	0.168	32	390	24	105
-200	3.33	1.70	0.174	38	360	23	128
-100	3.48	2.23	0.217	80	491	27	146
0	3.30	1.56	0.204	44	371	26	130
100	3.55	1.81	0.222	52	431	26	160
200	3.17	1.60	0.175	38	371	23	117
300	3.36	1.39	0.237	32	436	25	118
400	3.18	1.59	0.195	45	421	24	127
500	3.52	1.60	0.161	28	515	22	107
600	3.65	2.02	0.242	60	453	31	174
700	3.32	1.69	0.189	53	416	25	133
800	3.51	1.62	0.245	34	463	23	125
900	3.47	1.62	0.272	34	467	26	144
1000	3.36	1.74	0.216	39	435	29	162
1100	3.66	1.49	0.223	35	467	24	152
1200	3.49	1.71	0.270	31	525	27	148
1300	3.54	1.71	0.224	43	436	25	148
1400	3.49	1.53	0.226	44	544	23	151
1500	3.50	1.82	0.249	44	544	24	131
1600	3.90	1.95	0.245	61	511	24	179
1700	3.50	1.63	0.310	38	579	24	157
1800	3.77	1.73	0.210	38	603	20	143
1900	4.16	1.69	0.260	35	478	24	180
2000	4.11	1.79	0.246	42	621	24	181
2100	3.70	1.92	0.203	57	519	23	156
2200	3.84	1.86	0.262	51	580	21	179
2300	4.00	2.05	0.258	48	533	22	182
2400	4.12	2.25	0.244	53	537	22	202
2500	3.90	1.95	0.192	56	505	22	155
2600	3.87	1.67	0.271	38	573	19	143
2700	4.04	2.10	0.214	59	547	19	164
2800	4.14	2.31	0.195	58	474	21	163
2900	3.86	1.74	0.214	39	705	19	151
3000	4.16	2.03	0.360	52	507	26	245
3100	3.96	2.12	0.277	52	649	18	164
3200	4.14	2.26	0.270	66	764	16	134
3300	4.03	1.97	0.204	50	540	16	130
3400	3.78	2.18	0.183	70	451	17	140
3500	4.30	2.37	0.335	76	815	15	185
3600	3.85	2.37	0.234	62	541	15	129
3700	3.41	1.71	0.211	52	548	19	138
3800	3.67	2.57	0.274	83	683	15	145
3900	3.76	2.20	0.212	56	538	14	115
4000	3.44	2.96	0.271	95	572	18	182

Elevation Bin	Na2O (wt%)	K2O (wt%)	P2O5 (wt%)	Rb (ppm)	Sr (ppm)	Y (ppm)	Zr (ppm)
4100	3.85	2.78	0.211	102	569	18	168
4200	3.95	2.66	0.208	107	513	17	169
4300	3.76	2.95	0.256	117	531	18	166
4400	3.69	3.07	0.230	153	522	14	161
4500	3.50	3.10	0.255	132	498	22	193
4600	3.93	3.31	0.309	143	489	15	159
4700	3.69	2.74	0.219	123	493	18	165
4800	3.77	3.22	0.220	138	515	17	168
4900	3.91	2.32	0.274	69	640	17	172
5000	4.02	2.71	0.237	97	570	16	160
5100	3.58	3.31	0.192	141	448	18	159
5200	3.48	3.99	0.220	198	427	18	191
5300	4.32	3.14	0.154	91	680	13	190
5400	3.37	2.71	0.263	103	562	21	211
5500	4.15	2.16	0.194	64	549	11	108
5600	2.69	4.74	0.380	216	612	18	250
5700	4.94	3.73	0.155	109	612	11	172
5900	3.85	2.55	0.277	84	765	22	217

Elevation Bin	La (ppm)	Yb (ppm)	Gd (ppm)	La/Yb	Gd/Yb	Rb/Sr
-1000	37	2.2	6.4	17	3	0.026
-900	9	2.5	3.5	3	1	0.050
-800	5	1.9	2.3	3	1	0.074
-700	12	2.5	3.8	5	2	0.055
-600	12	2.3	3.6	5	2	0.070
-500	43	2.4	5.8	18	2	0.123
-400	6	2.4	3.3	2	1	0.061
-300	13	2.5	3.8	5	2	0.083
-200	15	2.6	3.5	6	1	0.105
-100	33	2.9	4.6	11	2	0.162
0	19	2.6	4.3	7	2	0.119
100	25	2.3	4.9	11	2	0.120
200	19	2.2	3.9	9	2	0.103
300	16	2.3	4.5	7	2	0.073
400	22	2.3	4.3	9	2	0.107
500	20	2.0	3.6	10	2	0.054
600	29	2.5	5.3	12	2	0.133
700	17	2.3	4.1	7	2	0.128
800	19	2.3	4.3	8	2	0.074
900	19	2.4	4.7	8	2	0.073
1000	23	2.8	4.7	8	2	0.091
1100	20	2.2	4.5	9	2	0.076
1200	24	2.3	4.7	10	2	0.059
1300	24	2.3	4.4	10	2	0.099
1400	20	2.3	4.0	9	2	0.082
1500	21	2.4	4.5	9	2	0.081
1600	22	2.5	5.3	9	2	0.119
1700	23	2.1	4.6	11	2	0.065
1800	18	2.0	3.7	9	2	0.064
1900	18	2.2	4.9	8	2	0.074
2000	23	2.3	4.5	10	2	0.067
2100	20	2.3	4.7	9	2	0.110
2200	22	2.1	4.6	10	2	0.089
2300	23	2.0	4.5	12	2	0.089
2400	24	2.5	4.8	10	2	0.099
2500	22	1.9	4.0	12	2	0.111
2600	23	2.1	4.2	11	2	0.067
2700	24	1.8	4.0	13	2	0.108
2800	24	1.8	4.2	14	2	0.123
2900	23	1.9	4.2	12	2	0.055
3000	27	2.7	5.9	10	2	0.102
3100	30	1.7	5.1	17	3	0.080
3200	23	1.5	3.8	15	2	0.086
3300	20	1.4	3.4	14	2	0.093
3400	21	1.8	3.4	12	2	0.156
3500	34	1.8	4.4	19	2	0.094
3600	23	1.6	3.4	14	2	0.114
3700	23	2.0	4.6	12	2	0.094
3800	30	1.7	3.6	18	2	0.121
3900	21	1.5	2.9	14	2	0.105
4000	35	1.7	4.5	21	3	0.165

Elevation Bin	La (ppm)	Yb (ppm)	Gd (ppm)	La/Yb	Gd/Yb	Rb/Sr
4100	33	1.7	4.3	20	3	0.178
4200	34	1.6	4.2	21	3	0.209
4300	34	1.7	4.6	20	3	0.221
4400	28	1.6	3.5	18	2	0.294
4500	37	1.7	4.9	21	3	0.266
4600	35	1.5	4.4	23	3	0.293
4700	32	1.6	4.8	19	3	0.249
4800	39	1.7	4.1	23	2	0.267
4900	27	1.5	4.4	18	3	0.107
5000	31	1.5	4.1	20	3	0.170
5100	35	1.8	4.5	20	3	0.314
5200	42	1.6	5.8	27	4	0.464
5300	37	1.4	4.1	27	3	0.134
5400	42	1.9	5.2	22	3	0.184
5500	22	1.4	2.9	16	2	0.116
5600	79	1.5	6.9	54	5	0.353
5700	42	1.2		34		0.178
5900	44	1.7	6.4	26	4	0.109

Elevation Bin	Crustal Thickness (km)	Melt Fraction	Lithostatic Pressure (GPa)
-1000	20.8	0.31	0.6
-900	21.5	0.49	0.6
-800	22.2	0.47	0.6
-700	22.9	0.40	0.6
-600	23.7	0.49	0.7
-500	24.4	0.19	0.7
-400	25.1	0.63	0.7
-300	25.8	0.30	0.7
-200	26.6	0.25	0.7
-100	27.3	0.19	0.8
0	28.0	0.28	0.8
100	28.7	0.24	0.8
200	29.4	0.27	0.8
300	30.2	0.31	0.8
400	30.9	0.27	0.9
500	31.6	0.27	0.9
600	32.3	0.21	0.9
700	33.1	0.25	0.9
800	33.8	0.27	1.0
900	34.5	0.27	1.0
1000	35.2	0.25	1.0
1100	36.0	0.29	1.0
1200	36.7	0.25	1.0
1300	37.4	0.25	1.1
1400	38.1	0.28	1.1
1500	38.9	0.24	1.1
1600	39.6	0.22	1.1
1700	40.3	0.26	1.1
1800	41.0	0.25	1.2
1900	41.8	0.25	1.2
2000	42.5	0.24	1.2
2100	43.2	0.22	1.2
2200	43.9	0.23	1.2
2300	44.7	0.21	1.3
2400	45.4	0.19	1.3
2500	46.1	0.22	1.3
2600	46.8	0.26	1.3
2700	47.5	0.20	1.3
2800	48.3	0.19	1.4
2900	49.0	0.25	1.4
3000	49.7	0.21	1.4
3100	50.4	0.20	1.4
3200	51.2	0.19	1.4
3300	51.9	0.22	1.5
3400	52.6	0.20	1.5
3500	53.3	0.18	1.5
3600	54.1	0.18	1.5
3700	54.8	0.25	1.5
3800	55.5	0.17	1.6
3900	56.2	0.20	1.6
4000	57.0	0.15	1.6

Elevation Bin	Crustal Thickness (km)	Melt Fraction	Lithostatic Pressure (GPa)
4100	57.7	0.15	1.6
4200	58.4	0.16	1.6
4300	59.1	0.15	1.7
4400	59.9	0.14	1.7
4500	60.6	0.14	1.7
4600	61.3	0.13	1.7
4700	62.0	0.16	1.7
4800	62.7	0.13	1.8
4900	63.5	0.19	1.8
5000	64.2	0.16	1.8
5100	64.9	0.13	1.8
5200	65.6	0.11	1.8
5300	66.4	0.14	1.9
5400	67.1	0.16	1.9
5500	67.8	0.20	1.9
5600	68.5	0.09	1.9
5700	69.3	0.12	2.0
5900	70.7	0.17	2.0

Table 7. Median arc lava compositions grouped by elevation

Elevation Bin	SiO2 (wt%)	TiO2 (wt%)	Al2O3 (wt%)	FeO* (wt%)	MnO (wt%)	MgO (wt%)	CaO (wt%)
-1000	48.00	0.78	17.59	8.78	0.16	7.79	12.02
-900	53.19	0.76	17.11	8.85	0.17	4.09	9.69
-800	54.59	0.65	15.75	9.57	0.17	4.48	9.56
-700	55.31	0.79	17.42	7.43	0.17	3.70	8.23
-600	57.57	0.69	17.00	7.08	0.18	3.64	7.80
-500	53.02	0.89	17.43	7.53	0.15	4.64	8.90
-400	52.36	0.73	17.21	9.38	0.18	4.32	10.24
-300	53.39	0.74	16.67	8.23	0.15	4.60	8.93
-200	56.07	0.73	16.99	8.02	0.16	3.82	7.78
-100	57.73	0.69	16.53	7.18	0.15	3.30	7.11
0	56.19	0.82	16.54	7.62	0.15	3.84	7.71
100	57.64	0.80	16.42	7.25	0.15	3.52	6.85
200	57.20	0.75	16.62	7.42	0.15	3.32	7.42
300	58.03	0.78	17.01	7.63	0.16	3.39	7.33
400	55.50	0.84	16.54	7.83	0.15	3.87	7.80
500	58.18	0.80	16.60	6.92	0.14	3.13	7.02
600	58.61	0.87	16.52	7.17	0.14	3.03	6.53
700	55.93	0.84	16.54	7.99	0.15	3.65	7.77
800	59.17	0.81	16.76	7.42	0.14	3.10	6.74
900	55.20	0.87	16.37	7.77	0.15	4.10	7.58
1000	59.09	0.81	16.41	7.27	0.14	3.37	6.72
1100	56.54	0.85	17.29	7.45	0.15	3.65	7.23
1200	54.52	0.91	17.24	8.10	0.15	3.94	7.82
1300	56.63	0.89	17.16	7.32	0.14	3.81	7.38
1400	55.75	0.80	17.09	7.45	0.14	4.26	7.49
1500	54.53	0.86	17.43	7.68	0.16	3.33	8.34
1600	57.50	0.94	16.90	6.71	0.11	3.35	6.90
1700	53.40	1.08	16.95	8.10	0.14	4.72	8.26
1800	56.69	0.84	17.23	6.48	0.12	3.95	7.03
1900	59.40	1.01	16.72	6.58	0.12	3.06	6.25
2000	58.70	0.82	17.36	6.11	0.11	3.58	6.44
2100	56.20	0.93	16.80	7.02	0.12	4.06	7.55
2200	56.77	0.92	17.02	6.74	0.12	4.00	6.96
2300	59.82	0.90	16.70	5.67	0.10	3.51	5.92
2400	60.13	0.86	16.90	5.59	0.11	2.80	5.78
2500	60.10	0.77	17.14	5.61	0.10	3.47	6.06
2600	54.50	0.98	17.34	7.35	0.14	4.77	7.64
2700	60.50	0.79	16.80	5.44	0.09	3.14	5.60
2800	63.25	0.74	16.15	4.61	0.09	3.29	4.87
2900	59.76	0.76	16.81	5.91	0.11	3.81	6.71
3000	58.65	0.99	16.20	6.17	0.12	3.99	6.20
3100	61.92	0.79	16.22	4.94	0.09	2.94	5.34
3200	58.89	0.81	17.13	6.01	0.11	3.16	6.00
3300	59.80	0.73	17.38	5.92	0.10	3.03	6.46
3400	61.70	0.70	16.21	5.97	0.10	3.21	5.77
3500	60.50	0.85	16.86	5.22	0.08	2.95	5.77
3600	62.70	0.70	16.01	5.03	0.08	2.53	5.16
3700	53.91	0.91	16.65	8.05	0.15	5.03	8.09
3800	59.94	0.80	16.20	5.48	0.10	2.76	6.03
3900	61.69	0.58	16.38	5.44	0.09	2.98	5.52
4000	60.50	0.89	16.50	5.52	0.10	2.50	5.80

Elevation Bin	SiO2 (wt%)	TiO2 (wt%)	Al2O3 (wt%)	FeO* (wt%)	MnO (wt%)	MgO (wt%)	CaO (wt%)
4100	63.24	0.74	16.21	4.56	0.07	2.40	4.50
4200	62.38	0.75	16.28	4.83	0.09	2.62	5.10
4300	61.36	0.82	16.53	5.25	0.09	2.37	5.19
4400	62.07	0.75	16.01	4.95	0.08	2.62	4.96
4500	62.16	0.87	16.05	5.20	0.09	2.56	5.30
4600	62.38	0.85	16.07	4.89	0.08	2.35	4.94
4700	62.36	0.72	16.24	4.96	0.09	2.55	4.96
4800	64.84	0.73	16.10	4.14	0.08	1.90	4.22
4900	58.50	0.87	16.55	6.39	0.11	3.58	6.29
5000	63.06	0.72	16.20	4.58	0.08	2.33	4.67
5100	63.26	0.72	16.03	4.65	0.08	1.97	4.70
5200	68.02	0.60	15.29	3.06	0.05	1.18	2.99
5300	62.29	0.97	15.75	5.12	0.07	2.51	4.97
5400	57.09	1.07	16.09	6.35	0.10	3.23	6.46
5500	63.15	0.65	16.40	4.96	0.08	2.40	4.91
5600	66.93	0.74	15.58	2.95	0.04	1.28	2.84
5700	67.39	0.58	15.37	3.11	0.05	1.44	2.85
5900	60.15	0.82	16.45	5.05	0.08	3.77	5.66

Elevation Bin	Na2O (wt%)	K2O (wt%)	P2O5 (wt%)	Rb (ppm)	Sr (ppm)	Y (ppm)	Zr (ppm)
-1000	2.20	1.29	0.524	18	846	26	74
-900	2.74	0.64	0.130	11	259	21	62
-800	2.14	0.52	0.110	8	234	15	30
-700	3.28	0.79	0.140	13	258	23	77
-600	3.44	0.63	0.145	13	253	25	76
-500	2.82	2.16	0.360	68	633	26	161
-400	2.22	0.37	0.100	5	185	23	43
-300	2.77	0.92	0.140	15	357	21	75
-200	2.99	1.16	0.160	20	278	22	80
-100	3.46	1.69	0.150	46	347	24	118
0	3.27	1.18	0.160	27	316	24	111
100	3.52	1.30	0.180	27	355	24	135
200	3.14	1.14	0.140	28	320	21	105
300	3.20	1.03	0.180	23	400	25	89
400	3.28	1.33	0.170	32	366	23	121
500	3.44	1.35	0.140	18	444	20	90
600	3.60	1.61	0.180	37	409	28	142
700	3.34	1.35	0.160	31	362	24	130
800	3.51	1.31	0.175	29	378	22	115
900	3.47	1.36	0.230	26	417	24	130
1000	3.20	1.56	0.170	34	423	25	142
1100	3.63	1.34	0.180	29	446	22	137
1200	3.54	1.39	0.200	23	468	22	138
1300	3.55	1.33	0.220	27	398	23	142
1400	3.60	1.28	0.190	26	513	20	119
1500	3.53	1.73	0.250	38	544	23	107
1600	3.90	1.54	0.210	45	448	22	157
1700	3.46	1.30	0.270	27	553	23	145
1800	3.83	1.34	0.180	24	584	19	124
1900	4.16	1.60	0.270	31	444	23	173
2000	4.05	1.37	0.200	23	552	21	141
2100	3.69	1.57	0.200	36	521	22	139
2200	3.84	1.50	0.230	31	527	19	155
2300	4.00	1.67	0.214	35	522	20	163
2400	3.98	1.97	0.210	38	502	20	151
2500	4.00	1.67	0.190	35	548	20	152
2600	3.80	1.40	0.240	30	561	19	137
2700	4.06	1.95	0.210	48	568	18	151
2800	4.22	2.02	0.186	56	434	21	155
2900	3.79	1.70	0.180	28	669	17	138
3000	4.18	1.59	0.285	33	517	25	205
3100	4.02	1.91	0.220	43	588	18	162
3200	4.18	2.15	0.260	53	760	15	123
3300	4.03	1.59	0.206	36	567	15	121
3400	3.76	1.77	0.170	40	418	17	145
3500	4.33	2.48	0.270	45	864	13	177
3600	3.94	2.14	0.192	33	462	13	104
3700	3.43	1.20	0.193	23	403	20	109
3800	3.76	2.39	0.230	68	636	14	125
3900	3.88	1.76	0.150	42	500	12	87
4000	3.44	2.48	0.290	66	575	19	172

Elevation Bin	Na2O (wt%)	K2O (wt%)	P2O5 (wt%)	Rb (ppm)	Sr (ppm)	Y (ppm)	Zr (ppm)
4100	3.90	2.70	0.190	64	540	17	163
4200	4.01	2.30	0.194	74	474	17	171
4300	3.75	2.76	0.260	84	524	17	161
4400	3.75	2.89	0.220	89	552	14	160
4500	3.42	2.93	0.255	119	512	22	197
4600	4.14	3.14	0.280	125	421	16	166
4700	3.64	2.52	0.210	87	462	18	164
4800	3.90	3.22	0.200	122	514	14	166
4900	3.98	2.21	0.240	51	607	16	155
5000	4.28	3.00	0.222	70	580	15	165
5100	3.57	3.34	0.200	121	464	18	152
5200	3.42	4.13	0.190	232	325	18	174
5300	4.30	2.91	0.160	78	718	14	187
5400	3.46	2.76	0.200	81	536	20	240
5500	4.16	2.14	0.185	59	560	10	101
5600	2.69	4.74	0.380	216	612	18	250
5700	5.07	3.68	0.175	109	611	11	172
5900	3.80	2.76	0.260	92	810	22	223

Elevation Bin	La (ppm)	Yb (ppm)	Gd (ppm)	La/Yb	Gd/Yb	Rb/Sr
-1000	38	2.1	6.1	18	3	0.021
-900	7	1.8	3.0	4	2	0.042
-800	2	1.9	2.1	1	1	0.034
-700	8	2.1	3.4	4	2	0.050
-600	9	1.9	3.0	5	2	0.051
-500	45	2.3	5.9	20	3	0.107
-400	3	2.1	3.0	1	1	0.028
-300	7	2.1	3.2	3	2	0.042
-200	12	2.4	3.3	5	1	0.072
-100	27	2.5	4.0	10	2	0.133
0	15	2.3	3.9	7	2	0.085
100	16	2.1	4.4	7	2	0.076
200	19	2.0	3.6	9	2	0.088
300	12	2.1	4.1	5	2	0.056
400	17	2.2	4.0	8	2	0.087
500	12	1.8	3.2	7	2	0.041
600	16	2.2	5.3	7	2	0.090
700	13	2.0	3.9	7	2	0.084
800	16	2.0	4.2	8	2	0.077
900	16	2.1	4.5	7	2	0.061
1000	18	2.2	4.3	8	2	0.080
1100	15	2.1	4.1	7	2	0.065
1200	19	2.1	4.1	9	2	0.050
1300	20	2.1	4.1	10	2	0.068
1400	15	1.8	3.6	8	2	0.050
1500	16	2.2	4.0	7	2	0.070
1600	19	2.3	5.3	8	2	0.100
1700	18	2.0	4.4	9	2	0.048
1800	15	2.0	3.5	8	2	0.041
1900	17	2.0	4.3	9	2	0.070
2000	13	2.0	3.6	6	2	0.041
2100	19	2.0	4.6	10	2	0.069
2200	20	1.8	4.3	11	2	0.059
2300	21	1.7	4.2	12	2	0.067
2400	19	1.9	4.8	10	2	0.076
2500	18	1.8	4.1	10	2	0.063
2600	20	2.0	4.3	10	2	0.053
2700	22	1.6	3.8	14	2	0.085
2800	23	1.7	3.6	14	2	0.129
2900	17	1.5	3.3	11	2	0.042
3000	25	2.4	6.2	10	3	0.064
3100	24	1.6	4.6	15	3	0.073
3200	23	1.4	3.7	16	3	0.069
3300	16	1.3	3.3	13	3	0.063
3400	19	1.8	3.4	11	2	0.096
3500	37	1.8	4.8	21	3	0.052
3600	17	1.6	2.8	10	2	0.071
3700	16	2.0	4.5	8	2	0.057
3800	25	1.5	3.2	16	2	0.107
3900	13	1.5	2.5	9	2	0.083
4000	32	1.6	4.5	20	3	0.114

Elevation Bin	La (ppm)	Yb (ppm)	Gd (ppm)	La/Yb	Gd/Yb	Rb/Sr
4100	35	1.5	3.9	23	3	0.119
4200	34	1.5	4.2	22	3	0.156
4300	34	1.6	4.8	22	3	0.160
4400	20	1.5	3.4	14	2	0.161
4500	38	1.7	5.0	22	3	0.232
4600	38	1.5	4.7	25	3	0.297
4700	28	1.5	5.1	18	3	0.188
4800	42	1.6	4.0	25	2	0.237
4900	21	1.4	4.0	15	3	0.083
5000	30	1.6	3.6	19	2	0.120
5100	35	1.9	4.1	19	2	0.260
5200	40	1.3	5.3	31	4	0.714
5300	37	1.2	4.0	29	3	0.109
5400	50	1.8	4.5	27	3	0.151
5500	21	1.2	2.8	18	2	0.104
5600	79	1.5	6.9	54	5	0.353
5700	42	1.2		34	0	0.178
5900	43	1.7	6.4	26	4	0.114

Table 8. Standard deviation of arc compositions grouped by elevation

Elevation Bin	SiO2 (wt%)	TiO2 (wt%)	Al2O3 (wt%)	FeO* (wt%)	MnO (wt%)	MgO (wt%)	CaO (wt%)
-1000	0.25	0.02	1.82	0.15	0.03	1.94	0.48
-900	9.31	0.32	2.58	3.08	0.05	2.99	3.73
-800	5.56	0.29	1.33	2.30	0.05	2.09	2.56
-700	7.59	0.22	2.28	2.41	0.05	2.16	3.02
-600	7.35	0.30	2.12	2.20	0.06	2.27	3.13
-500	4.32	0.25	1.25	1.39	0.06	1.62	2.03
-400	6.25	0.27	2.06	2.36	0.05	2.56	2.83
-300	8.43	0.46	2.07	2.98	0.12	2.94	3.67
-200	6.84	0.38	2.60	2.90	0.05	3.20	3.35
-100	7.73	0.63	2.16	2.51	0.12	2.55	3.25
0	7.35	0.52	1.86	2.98	0.12	2.72	2.96
100	8.09	0.61	1.99	2.83	0.07	2.95	3.14
200	8.01	0.53	1.78	2.83	0.06	2.62	2.93
300	6.65	0.51	1.71	2.39	0.40	2.37	2.54
400	7.51	0.49	1.73	3.25	0.06	2.21	2.86
500	8.15	0.46	2.62	2.49	0.10	2.43	3.10
600	7.01	0.52	1.62	2.49	0.06	2.39	2.71
700	9.20	0.56	2.01	3.27	0.06	2.59	3.22
800	6.58	0.45	1.62	2.33	0.43	2.40	2.45
900	7.75	0.51	1.64	2.59	0.05	3.05	2.74
1000	7.07	0.43	1.73	2.31	0.06	2.70	2.55
1100	6.63	0.50	1.65	2.41	0.05	2.30	2.57
1200	7.95	0.54	2.16	2.56	0.93	2.61	3.01
1300	7.84	0.51	1.64	2.83	0.46	2.61	2.82
1400	7.66	0.47	2.03	2.71	0.52	2.82	2.85
1500	6.90	0.40	2.02	2.54	0.11	2.23	3.08
1600	7.95	0.50	1.69	2.76	0.05	2.34	2.92
1700	7.40	0.59	1.93	2.73	0.50	2.78	2.77
1800	7.49	0.35	1.44	2.41	0.05	2.93	2.97
1900	6.66	0.40	1.27	2.19	0.04	2.22	2.38
2000	6.80	0.45	1.60	2.34	0.04	2.10	2.55
2100	7.98	0.45	2.05	2.72	0.05	2.40	3.08
2200	6.54	0.47	1.48	2.28	0.04	2.28	2.30
2300	6.71	0.61	1.45	2.34	0.04	2.03	2.31
2400	7.06	0.45	1.49	2.40	0.04	2.38	2.64
2500	5.54	0.26	1.43	1.71	0.04	1.86	1.90
2600	5.95	0.30	1.34	1.93	0.03	2.36	2.23
2700	4.97	0.32	1.12	1.74	0.04	1.81	1.82
2800	4.11	0.24	1.15	1.53	0.04	1.74	1.56
2900	5.39	0.31	1.17	1.83	0.04	1.80	2.06
3000	7.28	0.57	1.26	2.41	0.04	2.72	2.29
3100	5.92	0.31	0.90	1.77	0.03	2.30	1.74
3200	5.00	0.22	1.22	1.72	0.06	1.71	1.80
3300	6.10	0.37	1.60	2.01	0.03	1.65	2.08
3400	6.50	0.29	1.72	2.33	0.04	1.88	2.24
3500	4.46	0.33	0.98	1.44	0.03	1.15	1.56
3600	6.18	0.34	1.15	1.89	0.03	2.13	1.82
3700	6.04	0.28	1.50	2.20	0.05	2.85	2.39
3800	5.46	0.34	1.36	1.81	0.04	2.49	1.82
3900	4.53	0.31	1.06	1.45	0.08	1.69	1.50
4000	6.69	0.51	1.41	2.42	0.04	1.86	2.51

Elevation Bin	SiO2 (wt%)	TiO2 (wt%)	Al2O3 (wt%)	FeO* (wt%)	MnO (wt%)	MgO (wt%)	CaO (wt%)
4100	5.61	0.34	1.07	1.84	0.04	1.91	1.85
4200	4.77	0.27	0.98	1.56	0.03	1.70	1.59
4300	6.10	0.32	1.55	2.08	0.04	1.28	2.00
4400	5.34	0.31	1.92	1.68	0.04	1.96	1.84
4500	4.67	0.29	0.86	1.64	0.03	1.33	1.67
4600	5.47	0.39	1.05	1.77	0.03	1.21	1.70
4700	5.24	0.22	1.15	1.55	0.03	1.49	1.74
4800	5.13	0.31	1.17	1.66	0.03	1.41	1.61
4900	4.24	0.24	0.97	1.35	0.03	1.31	1.42
5000	3.86	0.18	0.90	1.22	0.02	1.01	1.32
5100	5.59	0.31	1.20	1.78	0.04	1.75	1.80
5200	5.02	0.31	0.86	1.50	0.03	1.96	1.43
5300	4.40	0.31	0.89	1.59	0.06	0.99	1.35
5400	6.95	0.30	0.72	2.38	0.04	2.80	2.50
5500	2.46	0.18	0.50	0.87	0.01	0.74	0.84
5600	0.00	0.00	0.00	0.00	0.00	0.00	0.00
5700	3.72	0.17	0.32	0.98	0.02	0.63	1.45
5900	3.27	0.09	0.61	0.77	0.02	1.63	1.37

Elevation Bin	Na2O (wt%)	K2O (wt%)	P2O5 (wt%)	Rb (ppm)	Sr (ppm)	Y (ppm)	Zr (ppm)
-1000	0.25	0.30	0.085	12	82	4	14
-900	1.15	0.82	0.103	16	199	33	63
-800	0.74	0.89	0.050	33	160	8	59
-700	0.91	1.01	0.124	33	387	10	66
-600	1.06	0.70	0.094	36	156	11	46
-500	0.61	1.15	0.188	38	198	6	58
-400	0.95	0.86	0.094	40	142	10	96
-300	0.97	1.45	0.163	58	201	12	100
-200	1.39	1.69	0.150	43	261	13	154
-100	0.97	1.71	0.209	92	384	12	113
0	0.88	1.26	0.185	53	239	15	92
100	1.03	1.49	0.198	87	299	12	151
200	0.77	1.21	0.150	31	186	9	57
300	0.84	1.03	0.193	33	190	8	102
400	0.83	1.22	0.153	46	244	9	65
500	0.82	1.03	0.174	46	297	19	139
600	0.78	1.31	0.216	57	242	37	130
700	0.75	1.31	0.170	57	241	10	64
800	0.75	1.11	0.219	28	260	11	67
900	0.77	0.98	0.193	40	281	10	119
1000	0.92	0.95	0.172	43	238	36	101
1100	0.91	0.89	0.182	29	232	10	82
1200	0.87	1.27	0.501	29	319	43	82
1300	0.70	1.15	0.153	46	248	12	68
1400	0.88	1.18	0.196	48	345	14	115
1500	0.76	1.25	0.151	45	297	12	68
1600	0.66	1.22	0.171	53	371	9	93
1700	0.83	1.09	0.372	35	255	7	83
1800	0.77	1.24	0.137	43	402	7	71
1900	0.68	0.83	0.125	25	235	8	66
2000	0.83	1.17	0.164	41	489	14	98
2100	0.67	1.31	0.157	53	208	10	77
2200	0.64	1.09	0.138	54	261	10	128
2300	0.63	1.07	0.235	41	231	9	109
2400	0.79	1.26	0.153	46	278	8	145
2500	0.60	0.92	0.132	53	202	9	43
2600	0.55	0.91	0.196	31	192	5	54
2700	0.49	0.84	0.122	38	183	7	63
2800	0.55	1.02	0.097	21	154	4	37
2900	0.63	0.75	0.132	38	314	13	112
3000	0.50	1.14	0.280	68	152	11	136
3100	0.58	0.89	0.162	39	270	7	37
3200	0.51	0.85	0.292	50	281	4	36
3300	0.46	0.91	0.096	36	147	5	38
3400	0.48	1.32	0.094	70	241	5	49
3500	0.57	1.06	0.237	101	324	6	83
3600	0.51	1.07	0.148	55	200	6	55
3700	0.69	1.08	0.130	51	346	6	65
3800	0.67	1.05	0.168	63	320	7	54
3900	0.58	1.18	0.162	42	225	6	60
4000	0.64	1.41	0.175	80	237	4	115

Elevation Bin	Na2O (wt%)	K2O (wt%)	P2O5 (wt%)	Rb (ppm)	Sr (ppm)	Y (ppm)	Zr (ppm)
4100	0.55	1.05	0.159	90	259	8	64
4200	0.62	1.08	0.130	84	272	4	40
4300	0.54	1.11	0.120	84	270	6	49
4400	0.56	1.06	0.167	185	252	5	62
4500	0.64	0.82	0.138	71	241	6	48
4600	0.65	0.90	0.169	85	333	6	64
4700	0.42	1.05	0.074	87	257	5	53
4800	0.67	0.80	0.121	73	245	7	49
4900	0.56	0.76	0.134	44	230	3	49
5000	0.54	0.95	0.083	69	230	5	46
5100	0.58	0.86	0.109	163	188	6	58
5200	0.73	0.74	0.124	74	195	5	57
5300	0.37	0.66	0.132	40	145	2	32
5400	0.45	1.04	0.119	70	161	5	57
5500	0.20	0.49	0.071	31	88	3	41
5600	0.00	0.00	0.000	0	0	0	0
5700	0.70	0.23	0.116	3	171	1	11
5900	0.10	0.48	0.057	32	122	4	15

Elevation Bin	La (ppm)	Yb (ppm)	Gd (ppm)
-1000	1	0.3	1.1
-900	9	1.8	2.5
-800	10	0.5	0.8
-700	14	1.2	1.6
-600	15	1.2	1.8
-500	19	0.7	2.0
-400	12	1.1	1.5
-300	18	1.5	2.3
-200	15	1.1	1.5
-100	28	1.3	2.2
0	16	1.2	2.5
100	29	0.9	2.4
200	11	0.7	1.4
300	15	0.9	2.4
400	35	0.8	1.8
500	83	0.7	1.3
600	96	1.0	2.0
700	16	1.1	1.8
800	13	0.9	1.9
900	14	0.9	1.6
1000	47	1.5	1.8
1100	15	0.9	1.9
1200	45	1.0	2.0
1300	15	0.9	1.4
1400	16	1.3	1.8
1500	29	0.9	1.8
1600	13	1.1	1.8
1700	42	0.8	1.2
1800	11	0.6	1.3
1900	9	0.8	2.2
2000	26	1.4	2.0
2100	11	2.3	1.6
2200	10	1.5	1.5
2300	13	0.9	1.7
2400	14	1.8	1.8
2500	27	0.4	0.9
2600	15	0.5	1.1
2700	13	0.7	1.1
2800	14	0.4	1.3
2900	15	1.7	1.9
3000	14	1.0	2.6
3100	14	0.8	2.1
3200	9	0.4	0.7
3300	9	0.4	1.0
3400	12	0.5	0.8
3500	16	0.4	1.1
3600	14	0.5	1.3
3700	21	0.5	1.8
3800	15	0.6	1.3
3900	17	0.6	1.2
4000	21	0.5	1.3

Elevation Bin	La (ppm)	Yb (ppm)	Gd (ppm)
4100	14	0.6	1.6
4200	15	0.4	1.0
4300	11	0.6	1.2
4400	18	0.5	1.8
4500	12	0.5	1.1
4600	15	0.4	1.7
4700	13	0.4	1.3
4800	13	0.5	1.2
4900	12	0.2	1.2
5000	12	0.4	1.5
5100	13	0.5	1.2
5200	9	0.6	1.7
5300	9	0.3	0.4
5400	16	0.2	1.2
5500	7	0.6	0.6
5600	0	0.0	0.0
5700	7	0.2	
5900	4	0.5	1.5

Appendix G: Bernasconi Hills whole rock trace element compositions

Table 9. Trace element contents of Bernasconi Hills samples

Sample	11H1	12H1	13H1	14H1	15H1	16H1
Position (m)	0.00	5.00	10.00	15.00	20.00	25.00
Sc	1.9	9.9	6.3	13.7	16.0	12.0
V	30	33	23	34	50	20
Cr	4	3	2	4	3	2
Cs	1	1	1	1	1	2
Pb	4	4	4	5	4	5
Th	2.8	0.8	2.2	2.7	1.4	0.9
U	0.5	0.7	0.5	0.7	0.7	0.8
Ba	668	446	1083	1110	1588	2006
Rb	44	38	44	49	54	51
Nb	3	4	3	4	4	3
La	10	8	13	15	8	6
Ce	14	15	21	24	16	11
Pr	1.5	2.2	2.3	2.9	2.1	1.7
Sr	257	244	192	278	299	216
Nd	5	10	8	12	10	9
Zr	181	263	207	289	316	196
Sm	0.9	2.4	1.5	2.7	2.4	2.3
Eu	0.7	0.9	0.7	0.9	0.8	0.8
Gd	0.7	2.6	1.6	2.7	2.8	2.9
Tb	0.1	0.4	0.2	0.4	0.4	0.5
Dy	0.6	2.7	1.3	2.6	2.6	3.1
Y	5	17	10	21	22	21
Ho	0.13	0.54	0.29	0.52	0.54	0.62
Er	0.4	1.6	0.8	1.4	1.5	1.7
Tm	0.06	0.22	0.12	0.19	0.21	0.23
Yb	0.4	1.4	0.8	1.2	1.3	1.6
Lu	0.07	0.23	0.15	0.19	0.20	0.25

Sample	17H1	18H1	19H1	110H1	111H1	11E1
Position (m)	30.00	35.00	40.00	45.00	50.00	0.00
Sc (ppm)	23.8	8.9	19.4	10.0	17.4	30.6
V	40	36	36	42	43	107
Cr	3	3	3	3	4	16
Cs	1	1	1	1	1	1
Pb	5	5	6	5	4	4
Th	1.7	2.6	1.4	2.1	1.0	0.8
U	1.0	0.8	0.6	0.7	0.7	0.3
Ba	1724	1600	1619	1184	504	496
Rb	47	52	41	49	31	36
Nb	5	5	4	5	5	8
La	13	12	10	11	12	20
Ce	31	21	23	19	26	47
Pr	4.7	3.0	3.0	2.5	3.3	7.2
Sr	219	187	325	210	337	299
Nd	19	13	14	11	14	34
Zr	235	253	373	251	420	249
Sm	5.2	3.1	4.0	2.4	3.5	8.6
Eu	0.9	0.9	1.1	0.8	1.1	1.3
Gd	5.9	3.4	4.6	2.7	3.4	9.0
Tb	1.0	0.5	0.7	0.4	0.5	1.5
Dy	6.4	3.2	4.7	2.6	3.4	9.5
Y	51	19	38	16	24	68
Ho	1.24	0.67	0.90	0.51	0.71	1.91
Er	3.7	1.9	2.5	1.6	2.1	5.6
Tm	0.53	0.25	0.35	0.22	0.27	0.79
Yb	3.2	1.7	2.2	1.4	1.7	4.9
Lu	0.49	0.28	0.31	0.22	0.29	0.75

Sample	12E1	13E1	14E1	15E1	16E1	17E1
Position (m)	5.00	10.00	15.00	20.00	25.00	30.00
Sc (ppm)	41.5	17.9	15.5	34.4	58.4	42.0
V	80	97	116	117	155	112
Cr	1	4	4	6	3	3
Cs	4	1	1	1	2	15
Pb	4	5	4	4	4	6
Th	0.6	0.7	0.8	0.7	0.6	1.4
U	0.6	0.5	0.4	0.6	0.8	1.1
Ba	789	570	662	690	712	962
Rb	76	39	45	49	63	126
Nb	9	7	5	10	17	18
La	19	16	16	18	29	16
Ce	44	45	35	46	88	43
Pr	6.4	7.1	5.2	7.3	14.3	7.1
Sr	391	251	244	247	216	308
Nd	28	35	22	35	69	35
Zr	462	214	238	223	130	577
Sm	6.7	8.6	5.2	9.5	18.5	9.4
Eu	1.1	1.3	1.2	1.4	2.0	1.3
Gd	6.6	8.2	4.9	9.7	19.0	9.8
Tb	1.0	1.3	0.8	1.6	3.1	1.6
Dy	6.7	8.4	5.3	10.5	19.7	10.1
Y	65	58	42	56	117	86
Ho	1.38	1.72	1.08	2.04	3.87	1.99
Er	4.1	4.8	3.4	5.9	11.3	5.5
Tm	0.57	0.65	0.47	0.77	1.63	0.82
Yb	3.6	3.8	3.0	4.7	10.3	5.5
Lu	0.54	0.60	0.45	0.70	1.49	0.82

Sample	18E2	19E1	112E1	21H1	22H1	22FMB1
Position (m)	35.00	40.00	55.00	0.00	5.00	5.00
Sc (ppm)	29.0	18.7	32.1	7.2	22.2	9.1
V	79	103	197	26	70	33
Cr	3	3	7	2	4	3
Cs	1	1	1	1	1	1
Pb	4	4	4	4	4	6
Th	0.7	0.6	1.1	1.7	2.5	2.4
U	0.4	0.4	0.5	0.8	0.7	0.8
Ba	621	504	599	1063	1047	1396
Rb	53	31	35	43	48	41
Nb	10	8	4	3	6	4
La	16	16	16	11	20	14
Ce	38	43	37	18	38	24
Pr	5.8	7.0	4.9	2.2	4.8	3.1
Sr	271	307	268	183	228	267
Nd	26	32	21	9	21	11
Zr	252	219	166	264	409	293
Sm	6.3	7.9	4.7	2.0	5.0	2.7
Eu	1.0	1.3	1.3	0.7	0.9	0.9
Gd	6.1	7.8	4.8	2.2	4.9	2.9
Tb	1.0	1.3	0.8	0.3	0.8	0.4
Dy	6.7	8.7	5.1	2.1	4.9	3.0
Y	62	57	41	14	43	21
Ho	1.32	1.68	1.04	0.41	0.89	0.57
Er	3.9	5.1	3.1	1.2	2.6	1.6
Tm	0.54	0.73	0.45	0.16	0.36	0.22
Yb	2.9	4.4	2.9	0.9	2.1	1.3
Lu	0.47	0.66	0.46	0.15	0.29	0.19

Sample	23H1	24H1	25H1	26H1	27H1	28H1
Position (m)	10.00	15.00	20.00	25.00	30.00	35.00
Sc (ppm)	3.0	14.3	10.0	14.2	25.5	12.4
V	29	41	36	46	62	33
Cr	3	5	3	4	7	3
Cs	1	1	1	1	1	1
Pb	5	5	4	4	5	5
Th	3.5	1.2	1.6	0.8	1.0	2.9
U	0.7	0.8	0.7	0.5	0.7	1.1
Ba	1353	886	940	730	874	768
Rb	54	45	35	34	36	32
Nb	4	6	5	6	5	4
La	22	10	12	8	10	17
Ce	31	20	22	20	20	34
Pr	3.1	3.2	2.9	3.6	3.2	4.5
Sr	214	173	230	204	387	186
Nd	11	17	13	19	15	19
Zr	273	209	239	266	405	240
Sm	1.6	4.7	3.3	4.8	4.2	4.3
Eu	0.9	1.0	0.9	0.9	0.9	0.9
Gd	1.7	5.3	3.3	4.8	4.8	4.5
Tb	0.2	0.8	0.5	0.8	0.7	0.7
Dy	1.2	4.9	3.1	5.1	4.7	4.1
Y	8	28	22	30	48	24
Ho	0.24	0.96	0.66	0.89	0.91	0.80
Er	0.8	3.1	2.0	2.4	2.5	2.4
Tm	0.10	0.38	0.24	0.30	0.34	0.33
Yb	0.8	2.5	1.5	2.1	2.0	1.8
Lu	0.14	0.39	0.23	0.27	0.31	0.30

Sample	29H1	210H1	211H1	212H1	213H1	214H1
Position (m)	40.00	45.00	50.00	55.00	60.00	65.00
Sc (ppm)	5.2	10.1	10.4	6.6	13.3	1.1
V	19	32	25	16	25	19
Cr	2	3	2	2	3	1
Cs	1	1	1	1	1	0
Pb	6	5	5	6	5	6
Th	2.2	2.2	2.5	3.0	2.0	1.1
U	0.7	0.6	0.6	0.5	0.4	0.4
Ba	1474	1002	1019	1706	1217	1249
Rb	46	45	39	48	46	43
Nb	3	4	3	2	4	1
La	12	13	16	18	18	7
Ce	20	27	26	28	30	10
Pr	2.4	3.1	3.1	3.3	3.5	1.1
Sr	189	209	199	187	236	185
Nd	10	13	12	13	15	4
Zr	199	218	263	142	275	170
Sm	1.9	2.8	2.6	2.6	3.3	0.6
Eu	0.8	0.8	0.7	0.9	0.8	0.7
Gd	2.2	2.9	2.7	2.8	3.4	0.6
Tb	0.3	0.4	0.4	0.4	0.5	0.1
Dy	1.8	2.7	2.7	2.5	3.1	0.4
Y	14	21	20	15	27	3
Ho	0.37	0.54	0.50	0.48	0.59	0.08
Er	1.1	1.6	1.5	1.4	1.7	0.3
Tm	0.14	0.19	0.21	0.20	0.21	0.04
Yb	0.9	1.3	1.2	1.2	1.2	0.3
Lu	0.14	0.21	0.19	0.18	0.18	0.05

Sample	215H1	216H1	217H1	218H1	219H1	220H1
Position (m)	70.00	75.00	80.00	85.00	90.00	95.00
Sc (ppm)	1.0	4.8	27.7	2.8	7.9	14.5
V	13	16	22	21	25	24
Cr	2	5	3	3	2	3
Cs	1	1	1	1	1	1
Pb	4	4	5	4	4	6
Th	1.7	7.6	3.4	2.1	1.8	3.4
U	0.2	0.4	0.8	0.4	0.6	0.6
Ba	948	375	176	294	948	1029
Rb	35	39	27	32	39	52
Nb	1	6	5	5	4	4
La	11	50	19	17	13	22
Ce	15	76	37	25	22	41
Pr	1.5	7.5	5.2	2.7	2.8	4.4
Sr	228	188	155	170	194	187
Nd	5	24	22	10	12	18
Zr	171	188	359	170	240	236
Sm	0.7	3.3	5.2	1.4	2.5	3.4
Eu	0.5	0.8	0.8	0.7	0.7	0.7
Gd	0.7	3.0	5.6	1.3	2.6	3.5
Tb	0.1	0.3	0.9	0.2	0.4	0.5
Dy	0.3	1.5	5.9	0.8	2.5	3.2
Y	3	12	35	5	18	20
Ho	0.08	0.31	1.10	0.16	0.50	0.63
Er	0.2	0.8	3.1	0.5	1.5	1.6
Tm	0.06	0.09	0.43	0.06	0.21	0.20
Yb	0.3	0.7	2.6	0.4	1.3	1.2
Lu	0.08	0.13	0.37	0.07	0.23	0.18

Sample	221H1	222H1	223H1	224H1	225H1	226H1
Position (m)	100.00	105.00	110.00	115.00	120.00	125.00
Sc (ppm)	19.2	30.4	19.8	35.9	1.7	13.4
V	73	211	153	110	27	60
Cr	8	2	10	3	3	25
Cs	1	1	1	1	1	1
Pb	4	4	5	4	4	4
Th	7.0	0.6	2.4	0.5	0.6	0.8
U	0.7	0.2	1.8	0.3	0.4	0.3
Ba	684	511	557	609	387	535
Rb	56	35	42	53	33	41
Nb	9	11	7	8	3	5
La	60	22	19	12	6	8
Ce	100	51	44	28	9	16
Pr	10.5	8.5	5.6	4.2	0.9	2.2
Sr	174	249	475	253	213	265
Nd	36	39	25	20	4	10
Zr	446	134	885	194	179	220
Sm	6.8	9.7	5.7	5.9	0.7	2.4
Eu	0.9	1.3	1.3	1.0	0.6	0.7
Gd	5.6	9.9	5.4	6.1	0.7	2.4
Tb	0.8	1.6	1.0	1.0	0.1	0.4
Dy	4.5	10.7	6.1	6.5	0.5	2.5
Y	29	71	45	42	4	18
Ho	0.89	2.28	1.23	1.26	0.11	0.49
Er	2.4	6.7	4.1	3.5	0.4	1.4
Tm	0.32	0.99	0.58	0.47	0.06	0.20
Yb	1.9	6.4	3.8	3.0	0.4	1.2
Lu	0.30	0.98	0.62	0.42	0.09	0.18

Sample	227H1	228H1	21E1	24E1	25E1	27E1
Position (m)	130.00	135.00	0.00	15.00	20.00	30.00
Sc (ppm)	9.5	2.2	29.4	39.5	37.3	39.9
V	31	27	175	219	251	159
Cr	2	2	4	20	7	10
Cs	1	3	1	0	1	1
Pb	5	5	5	4	4	4
Th	0.9	2.9	0.3	1.2	0.3	0.3
U	0.5	0.6	0.3	0.4	0.2	0.3
Ba	176	185	584	381	534	508
Rb	22	35	38	22	47	43
Nb	3	4	9	5	10	13
La	9	8	19	17	17	18
Ce	16	13	41	28	47	51
Pr	2.4	1.3	6.4	3.9	7.5	9.4
Sr	235	193	260	397	346	231
Nd	11	5	31	17	34	48
Zr	75	131	182	233	173	192
Sm	3.0	0.9	8.5	4.0	8.1	13.6
Eu	0.8	0.5	1.2	1.2	1.3	1.6
Gd	3.6	0.9	8.5	4.4	8.0	14.2
Tb	0.6	0.1	1.4	0.7	1.3	2.4
Dy	3.6	0.7	8.8	4.7	8.9	15.6
Y	22	5	61	36	94	119
Ho	0.77	0.14	1.70	0.99	1.81	3.12
Er	2.1	0.5	4.9	2.9	5.6	9.1
Tm	0.30	0.08	0.67	0.41	0.84	1.25
Yb	1.9	0.6	4.1	2.6	5.3	7.7
Lu	0.31	0.12	0.58	0.40	0.80	1.08

Sample	29E1	210E1	211E1	212E1	213E1	213MB1
Position (m)	40.00	45.00	50.00	55.00	60.00	60.00
Sc (ppm)	25.4	34.9	35.6	34.4	19.2	26.4
V	169	95	198	198	147	191
Cr	12	3	17	59	10	47
Cs	1	1	1	1	1	1
Pb	4	4	4	5	4	5
Th	1.3	0.3	5.3	4.4	0.8	6.9
U	0.4	0.3	0.8	1.3	0.4	0.8
Ba	420	617	357	229	386	319
Rb	35	55	40	22	43	47
Nb	5	11	4	2	7	3
La	15	15	16	11	13	12
Ce	29	36	39	23	36	27
Pr	3.9	5.6	5.6	2.9	5.5	3.7
Sr	283	217	206	219	163	162
Nd	16	26	23	10	23	15
Zr	139	165	120	103	96	100
Sm	3.8	7.3	5.2	2.1	5.3	3.3
Eu	1.0	1.2	1.3	1.0	1.1	1.0
Gd	4.1	8.0	5.0	2.3	5.1	3.4
Tb	0.7	1.3	0.8	0.4	0.9	0.5
Dy	4.4	8.3	5.5	2.6	5.9	3.5
Y	27	68	45	20	35	19
Ho	0.95	1.67	1.13	0.52	1.26	0.71
Er	3.0	4.6	3.4	1.7	4.0	2.2
Tm	0.46	0.62	0.51	0.25	0.62	0.33
Yb	3.1	3.6	3.4	1.7	4.1	2.2
Lu	0.49	0.52	0.54	0.27	0.64	0.34

Sample	214E1	217E1	218E1	219E1	221E1	222MB2
Position (m)	65.00	80.00	85.00	90.00	100.00	105.00
Sc (ppm)	38.9	26.8	32.0	50.1	21.7	41.4
V	215	166	180	305	145	219
Cr	27	18	14	18	12	3
Cs		1	1		1	3
Pb	6	4	5	4	3	6
Th	1.0	0.5	0.8	1.8	0.9	2.0
U	0.5	0.3	0.4	0.6	0.3	1.2
Ba	164	398	423	205	440	375
Rb	7	42	53	8	37	46
Nb	3	5	7	6	5	7
La	8	13	15	21	13	18
Ce	13	28	35	40	31	41
Pr	1.9	3.6	5.6	5.6	4.5	6.3
Sr	296	273	241	312	179	357
Nd	9	15	27	23	18	28
Zr	129	125	133	88	133	199
Sm	2.6	3.4	6.9	5.7	3.8	6.8
Eu	0.8	1.0	1.1	1.1	0.9	1.6
Gd	2.8	3.8	7.3	5.8	3.7	7.6
Tb	0.5	0.6	1.2	1.0	0.6	1.2
Dy	3.0	4.5	8.0	6.5	3.9	7.9
Y	25	32	60	55	35	51
Ho	0.59	0.91	1.62	1.35	0.88	1.65
Er	1.8	2.7	4.7	4.1	2.8	4.7
Tm	0.26	0.39	0.66	0.61	0.41	0.67
Yb	1.7	2.6	4.0	3.9	3.0	4.6
Lu	0.27	0.44	0.63	0.62	0.47	0.70

Sample	222FMB2	223E1	224E1	225E1	226E1	227E1
Position (m)	105.00	110.00	115.00	120.00	125.00	130.00
Sc (ppm)	27.5	32.1	22.1	31.1	29.4	32.0
V	213	236	147	203	150	172
Cr	3	5	7	41	3	5
Cs	1	1	1	1	1	2
Pb	5	3	3	4	4	4
Th	0.5	1.4	0.5	1.9	0.6	0.6
U	0.2	0.5	0.3	0.5	0.3	0.4
Ba	485	363	650	419	826	426
Rb	40	40	49	26	72	48
Nb	10	5	6	7	9	7
La	18	16	12	16	19	19
Ce	44	39	27	37	45	47
Pr	7.3	5.2	3.9	5.2	6.9	7.0
Sr	260	355	318	252	292	253
Nd	35	22	18	22	32	33
Zr	134	104	200	72	294	123
Sm	8.9	5.1	4.7	5.0	8.0	8.2
Eu	1.2	1.3	1.0	1.1	1.2	1.0
Gd	9.9	5.1	4.8	4.9	8.2	8.3
Tb	1.5	0.8	0.8	0.8	1.3	1.3
Dy	10.0	5.4	5.2	5.3	8.5	8.7
Y	65	42	35	33	63	70
Ho	2.06	1.14	1.04	1.12	1.73	1.71
Er	6.3	3.3	3.1	3.6	5.2	4.9
Tm	0.90	0.46	0.41	0.56	0.72	0.68
Yb	5.8	3.1	2.5	3.8	4.5	4.0
Lu	0.87	0.47	0.36	0.61	0.66	0.59

Sample	229E1
Position (m)	140.00
Sc (ppm)	18.5
V	129
Cr	1
Cs	4
Pb	4
Th	1.7
U	0.5
Ba	461
Rb	86
Nb	8
La	8
Ce	21
Pr	3.2
Sr	211
Nd	14
Zr	164
Sm	3.2
Eu	0.7
Gd	3.6
Tb	0.7
Dy	3.9
Y	35
Ho	0.82
Er	2.4
Tm	0.33
Yb	2.2
Lu	0.36